DISPERSION AND PROCESSING OF GRAPHENE AND MXENE NANOSHEETS

WITH APPLICATIONS IN STRUCTURAL ENERGY STORAGE

A Dissertation

by

SMIT ALKESH SHAH

Submitted to the Office of Graduate and Professional Studies of
Texas A&M University
in partial fulfillment of the requirements for the degree of

DOCTOR OF PHILOSOPHY

Chair of Committee,	Micah J. Green
Committee Members,	Jodie L. Lutkenhaus
	Miladin Radovic
	Zhengdong Cheng
Head of Department,	Arul Jayaraman

December 2019

Major Subject: Chemical Engineering

ABSTRACT

Two-dimensional (2D) nanomaterials are unique for their high surface-to-volume ratio and high aspect ratio making them useful in a range of applications. Graphene and MXenes are such 2D nanosheets and have great potential in applications such as polymer composites, electrochemical energy storage electrodes in batteries and supercapacitors, and conductive inks. Improvements to existing lab-scale synthesis and processing techniques are crucial to serve the high demand of graphene and MXene nanosheets and make their applications commercially viable.

In this study, various aspects of exfoliation, dispersion and processing of pristine graphene are investigated. A facile washing process was developed to recover graphene entrapped in the sediment to improve the overall yield of liquid phase exfoliated graphene (graphene/unexfoliated parent material). The total amount of graphene obtained through this approach increases with cumulative solvent volume. Graphene quantum dots (GQD) with sulfonyl, amine, and carboxylic functional groups were employed to exfoliate and disperse pristine graphene nanosheets in water. Sulfonyl functionalized GQD are able to disperse highest concentration of graphene in water compared to other functional groups. The results are consistent with a prior finding by pyrene and indicate that π- π stacking interaction between polyaromatic hydrocarbons (PAH) and graphene nanosheets and their role in dispersing graphene nanosheets are general across a wide range of PAH sizes and species. 2D flat $Ti_3C_2T_X$ MXene nanosheets were processed for the first time in a spray dryer to scroll, bend, and fold

them in to three-dimensional (3D) crumpled structures. This was the first experimental demonstration proving computational predictions that 2D MXene nanosheets can exist in a scrolled morphology. 3D graphene oxide (rGO) hydrogels were fabricated using colloidal self-assembly for application as supercapacitor electrodes due to their excellent specific surface area, high porosity, and electrically conductive continuous network. High-strength, Kevlar-derived aramid nanofibers (ANF) were employed as a reinforcing filler to improve the shear modulus of rGO hydrogels.

This work will pave the way for further research to design and fabricate nanosheet based electrode architectures with controlled morphology and reinforcement with structural fillers to develop load-bearing multifunctional energy storage devices.

DEDICATION

This dissertation is dedicated to my parents (Alkesh Shah, Seema Shah). For their selfless, unconditional love and support.

ACKNOWLEDGEMENTS

I am eternally grateful to my advisor Dr. Micah J. Green, whose expertise was invaluable in formulating the research topics in this dissertation. Your constant guidance for developing effective research communication skills was pivotal to my growth as a researcher. I sincerely appreciate your support related to my professional growth and career development. Thank you for being patient and understanding throughout my PhD, and for emphasizing the value of work-life balance. Despite your busy schedule, you always took out time for having discussions, providing feedback and motivation, and I am very grateful for that.

I would like to thank Dr. Jodie L. Lutkenhaus, Dr. Miladin Radovic, and Dr. Zhengdong Cheng for their valuable feedback and guidance as collaborators and committee members. Dr. Lutkenhaus, thank you for your insightful comments, and suggestions on electrochemical experimental designs. Dr. Radovic, thank you for sharing your materials science expertise on MAX phase synthesis and fluoride etching. Dr. Cheng, thank you for sharing your expertise on colloids and soft matter. I want to acknowledge Huili, Peipei, Evan, Se Ra, Anish, Evi, Glenn, Abhijeet and other collaborators and members of Radovic, Lutkenhaus, and Cheng research groups. Thank you for your collaborative efforts and fruitful discussions. I would also like to acknowledge Dr. Karim, Dr. Jayaraman, and Dr. Holste for their supportive words and for sharing invaluable research and teaching skills.

I am grateful to my current and past research group colleagues for their help and support. Dr. Dorsa Parviz, Dr. Fahmida Irin, Dr. Yueyi Xu and Dr. Charles B. Sweeney, thank you for making me feel welcome when I joined the group, and getting me accustomed to the labs and research. Special thanks to Dr. Wanmei Sun, Dr. Touseef Habib, and Xiaofei Zhao for your contributions, and stimulating discussions. I am very thankful to Kyler Rountree, Devon Kulhanek, and Eliza Price for their help with experiments. I also want to acknowledge Martin Pospisil, Morgan Odom, Nutan Patil, Saerom Yu, Pritishma Lakhe, Anas Muhammad, Joshua Hope, Dr. Taruna Bansala, and rest of the Green group for all those joyful moments and the good time we had working together. Big thanks to my friends and staff at the Artie McFerrin Department of Chemical Engineering for always being so welcoming and helpful.

CONTRIBUTORS AND FUNDING SOURCES

Contributors

This work was supervised by a dissertation committee consisting of Dr. Micah J. Green (advisor), Dr. Jodie L. Lutkenhaus, Dr. Zhengdong Cheng of the Artie McFerrin Department of Chemical Engineering, and Dr. Miladin Radovic of the Department of Materials Science and Engineering.

Some data from Chapter 3 was provided by Dr. Zhengdong Cheng and Minxiang Zeng from the Artie McFerrin Department of Chemical Engineering at Texas A&M University; this data is marked appropriately. All other work conducted for the dissertation was completed by the student independently.

Funding Sources

TABLE OF CONTENTS

ix

LIST OF FIGURES

xiv

LIST OF TABLES

CHAPTER 1

INTRODUCTION

1.1 Motivation

Graphene and other 2D materials show significant potential for applications in energy storage and conversion devices, optoelectronic devices, sensors, composites, catalysis etc. Graphene nanosheets possess unique combination of excellent properties such as high electrical and thermal conductivity, high surface area, exceptional mechanical properties which makes them very valuable to researchers from all scientific disciplines. Ever since the graphene was isolated by Dr. Geim and Dr. Novoselov in 2004, intense research interest has resulted in exploration of new layered materials with set of unique properties. Some other 2D materials of interest include MXenes, hexagonal boron nitride (hBN), transition metal oxides (TMOs), transition metal dichalcogenides (TMDs), and phosphorene.

The importance of development of new energy, health and infrastructure solutions cannot be emphasized enough. With the recent global push towards green energy resources, automotive and aerospace industries are interested in developing stronger, light-weight electrochemical energy storage solutions. To meet the upcoming industry requirements, it will become crucial to develop scalable production and processing approaches for graphene and MXene nanosheets which have been shown to have potential as electrodes for batteries and supercapacitors.

Liquid phase exfoliation of graphene is one of the potential ways to scalable production of graphene. However, for aqueous dispersions, stabilizing agents such as

polymers, pyrene derivatives, surfactants are needed to colloidally stabilize the exfoliated nanosheets. Usually, due to the high concentration of these dispersants with respect to graphene, the final application is affected. Sulfonyl functionalized pyrene derivates are found to be very efficient at dispersing graphene at low dispersant/graphene ratios. There is a need to investigate if influence of functionalization in dispersing and stabilizing graphene also extends to other types of polyaromatic hydrocarbons.

For certain applications requiring assembly of nanomaterials, their morphology, assembly and chemical functionality have significant influence the properties of the final macrostructure. Nanocomposites can be made to achieve multifunctionality or synergistic improvement in properties of advanced materials. Several polymers and polymer nanofibers such as polyvinyl alcohol (PVA), cellulose nanofiber, and aramid nanofibers have been employed to obtain enhancements in mechanical properties or to achieve multifunctionality in nanomaterial composites.

This dissertation addresses the processing of graphene and MXene nanosheets, self-assembly of graphene oxide (GO) and its composites with aramid nanofibers for applications in structural energy storage. The dissertation explores the creation of aggregation resistance crumpled powder for 2D MXene nanosheets using a template-free spray drying technique. The liquid phase processing of graphene nanosheets is also studied with respect to colloidal stability and separation scalability for improvement in yield.

1.2 Goals and outline of the dissertation

This dissertation is divided in six chapters, with the first one giving an overview of the topics discussed in the proposal. The focus of chapters 2 and 3 is on scalable exfoliation of pristine graphene nanosheets in aqueous phase with emphasis on use of dispersants as graphene stabilizers.[1-3] Chapter 4 is focused on synthesis and processing of $Ti_3C_2T_X$ MXene nanosheets into 3D crumpled morphology using spray drying approach.[4] Chapter 5 discussed synthesis and characterization of porous graphene oxide hydrogels with aramid nanofiber as fillers for application as structural supercapacitor electrodes.[5] Chapter 6 concludes the dissertation with discussion on the future work on MXene-ANF high strain conductive composites.

Chapter 2

2D graphene nanosheets

Graphene is a single layer allotrope of carbon consisting of sp^2 hybridized carbon atoms arranged in a honeycomb lattice structure. Today, graphene is a part of a vast family of 2D nanomaterials and is prized for its unique combination of excellent electrical, thermal (Thermal conductivity: 3000 WmK^{-1}), optical, and mechanical properties (Young modulus: > 0.5-1 TPa) with a theoretical specific surface area of 2500 m^2g^{-1} and experimental surface area: 400-700 m^2g^{-1}. As a result, graphene has been shown to have the potential for many applications such as energy storage and conversion, catalysis, solar cells, light emitting devices, photodetectors etc.

Graphene nanosheets can be obtained by two main approaches top-down and bottom-up synthesis. Bottom-up synthesis can produce graphene nanosheets with very

high quality suited for applications such as optoelectronics. Such methods include chemical vapor growth, epitaxial growth, and annealing SiC substrates. However, these methods suffer from low production rates making them unviable for large scale industrial applications.

Scalable liquid phase exfoliation of graphene

Scalable production of graphene through liquid-phase exfoliation has been plagued by low yields. Although several recent studies have attempted to improve graphene exfoliation technology, the problem of separating colloidal nanosheets from unexfoliated parent material has received far less attention. In this chapter we demonstrate a scalable method for improving nanosheet yield through a facile washing process. By probing the sedimentation of liquid-phase exfoliated slurries of graphene nanosheets and parent material, we found that a portion of exfoliated graphene is entrapped in the sediment but can be recovered by repeatedly washing the slurry of nanosheet and parent material with additional solvent. We found this process to significantly increase the overall yield of graphene (graphene / parent material) and recover a roughly constant proportion of graphene with each wash. The cumulative amount of graphene recovered is only a function of total solvent volume. Moreover, we found this technique to be applicable to other types of nanosheets such as boron nitride nanosheets.

Chapter 3

In this chapter we investigate π–π stacking of polyaromatic hydrocarbons (PAHs) with graphene surfaces, showing that such interactions are general across a wide range of PAH sizes and species, including graphene quantum dots. We synthesized a series of graphene quantum dots with sulfonyl, amino, and carboxylic functional groups and employed them to exfoliate and disperse pristine graphene in water. We observed that sulfonyl-functionalized graphene quantum dots were able to stabilize the highest concentration of graphene in comparison to other functional groups; this is consistent with prior findings by pyrene. The graphene nanosheets prepared showed excellent colloidal stability, indicating great potential for applications in electronics, solar cells, and photonic displays.

Chapter 4

$Ti_3C_2T_X$ and other types of MXene nanosheets are an exciting new class of 2D materials. However, little has been reported on manipulating the shape of MXene nanosheets. In chapter 4, we demonstrate that flat $Ti_3C_2T_X$ nanosheets encapsulated within spray-dried droplets can be scrolled, bent, and folded into 3D crumpled structures. This morphological change was observed to be reversible upon rehydration.

Chapter 5

Three-dimensional (3D) graphene porous architectures are notable for their unique combination of excellent specific surface area, high porosity, and electrically conductive continuous network. Specifically, self-assembled graphene hydrogels have

received attention in the field of electrochemical energy storage due to the ease of tailoring their electrical, mechanical, and structural properties. However, graphene hydrogels suffer from poor mechanical integrity compared to layered architectures like graphene buckypapers, limiting their applications in practical devices. In this chapter, we employ aramid nanofibers (ANFs) as structural fillers to enhance graphene hydrogel's shear modulus in the context of multifunctional (mechanical and electrochemical) architectures. ANFs are high strength, Kevlar®-derived polymeric nanofillers and are integrated with graphene hydrogels using a sol-gel gelation approach. The addition of 2 wt.% ANFs resulted in an 80% improvement in shear modulus compared to neat graphene hydrogel. Addition of ANFs resulted in gradual reduction of specific capacitance, with the specific capacitance of 190 F/g for neat graphene hydrogel, reducing to 128 F/g for an ANF loading of 15 wt.% (dry weight basis). This work shows the broader concept that adding high-strength nanofibers to a nanomaterial gel can add reinforcement provided that the gelation process itself is not disrupted.

CHAPTER 2

COLLOIDAL PROCESSING OF PRISTINE GRAPHENE AQUEOUS

DISPERSIONS[*][†]

2.1 Introduction

Significance of pristine graphene nanosheets

The precise term "pristine" typically refers to graphene produced through mechanical exfoliation of graphite without inducing chemical functionalization. Furthermore, the term pristine graphene is used in contrast to graphene oxide (GO) nanosheets and other partially oxidized graphene-like materials. GO is commonly used in academic graphene research because of its ease of exfoliation, but the high degree of oxidation has certain drawbacks, such as poor electrical conductivity and surface defects. In this chapter, the term "pristine graphene" is used to define graphene nanosheets which are 1–10 layers thick with minimal defects and functionalization, based on the influential paper by Ferrari *et al*.[6] The term "graphene" has been very loosely used in the literature, and researchers have confused it with nanoscale platelets which are ≈100 nm thick. More detailed discussions of graphene nomenclature can be found elsewhere.[7]

Pristine graphene differs from graphene oxide both in its low oxygen content and in that it often consists of multiple layers. Graphene nanosheets may be produced with significant differences in the morphological properties such as lateral size and thickness, the surface area, the density of structural and compositional defects on the surface, the residual impurity content, surface chemistry, and chemical reactivity, depending on their preparation strategy.[8] These characteristics strongly affect the functional properties of graphene (Figure 2.1).
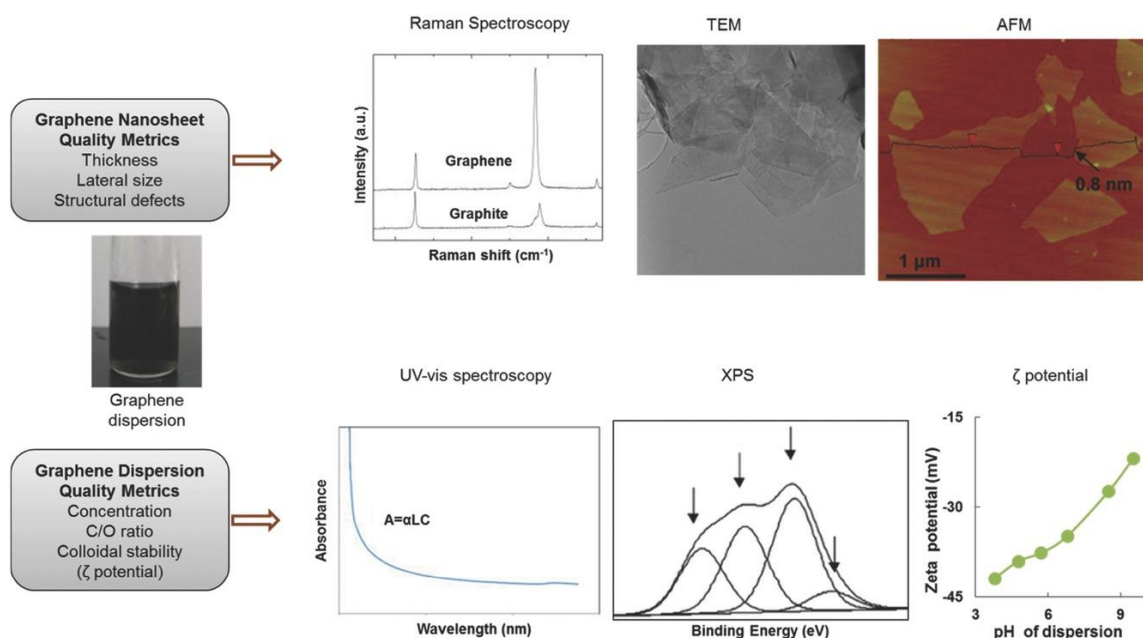
Figure 2.1 Metrics and measurement techniques used to determine the quality of graphene nanosheets and their dispersions. Reprinted with permission from Parviz *et al.*[1]

Top-down approach for direct exfoliation of graphite to graphene in liquids

Current techniques produce graphene in both "bottom-up" and "top-down" approaches: "bottom-up" methods include chemical vapor deposition[9,10] or epitaxial growth[11]on a substrate and do tend to produce high-quality graphene films. However,

these methods produce large-area (>1 cm^2), small-mass quantities of graphene and are not suitable for bulk material applications. In contrast, "top-down" approaches have been explored to exfoliate graphene nanosheets from graphitic precursors. These approaches may result in graphene dispersed in a liquid medium or isolated as a powder, typically with lateral areas on the order of square micrometers. Such nanosheets are suitable for preparation of electrodes in batteries and supercapacitors, polymer composites, and conductive inks and coatings.

Graphite or its derivatives are the main carbon source in the top-down approach that aims to "exfoliate" single- to few-layer graphene nanosheets from the parent graphitic material. Since the interlayer van der Waals (vdW) attractive forces in graphite are weak, they can be overcome by an external force, resulting in separation of adjacent layers. These external forces may have side effects on the material, such as the creation of defects in the basal plane.[12] Maintaining the exfoliated state of the separated graphene nanosheets requires an energy barrier which prevents the reaggregation of the nanosheets, especially in a liquid medium.

What is typically termed "pristine graphene" is typically colloidal pristine graphene exfoliated directly from graphite in the presence of a low-viscosity liquid medium. This approach involves the following steps: i) Pretreatment of graphite, ii) exfoliation of graphite, iii) stabilization of graphene layers, and iv) separation of graphene nanosheets from unexfoliated and nonstabilized graphitic material.[13] These steps are depicted schematically in Figure 2.2, and are discussed in detail below.
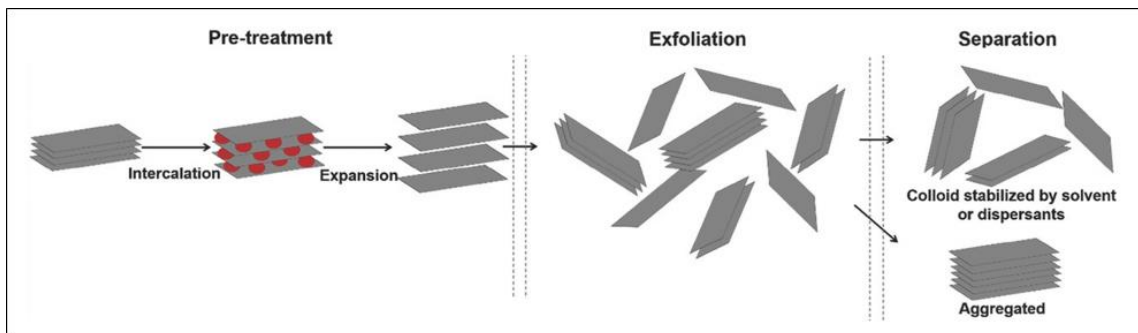
Figure 2.2 Mechanism of graphene processing through pretreatment, exfoliation, and separation or reduction units. Even after exfoliation, graphene nanosheets are prone to reaggregate unless solvent or dispersant interactions allow for inter-nanosheet repulsion and prevent aggregation. Reprinted with permission from Parviz *et al.*[1]

Pretreatment involves reducing the graphite interlayer attractive forces by intercalation of various atoms and molecules into the graphite structure and increasing the interlayer spacing to allow for easier exfoliation.[14] Intercalation involves the insertion of small molecules in between the graphite layers to produce graphite intercalation compound (GIC), followed by applying an external stimuli (often heat) to rapidly expand the intercalated molecules.[15-17] Various intercalating agents ranging from supercritical CO_2 to bisulfate salts have been reported.[18-20] The subsequent thermal shock of GICs leads to flash evaporation and release of the intercalants in the interlayer spacing of graphite and ultimate expansion of the layers. This thermal shock process has been accomplished via microwave radiation or rapid heating to high temperatures (>1000 °C).[21,22]

Mechanical exfoliation techniques

The most widely used mechanical exfoliation strategy is direct exfoliation of graphite in a solvent using ultrasonication. The ultrasonic waves produce cavitation bubbles in the solvent; it has been proposed that as these bubble collapses due to the pressure increase, they generate high energy microjets and shock waves that can exert compressive stress on the bulk graphite to induce exfoliation.[23,24] Additional mechanisms have been proposed, including: i) unbalanced compressive forces on two adjacent layers cause a shear-induced exfoliation or ii) microjets acting as wedges in the interlayer spacing of graphite and induce exfoliation.

Shear mixing may also be utilized as a means of mechanical exfoliation which relies on high shear forces that delaminate graphene nanosheets.[25] The graphene nanosheets produced by this method tend to have higher lateral size and less defects compared to sonication, but often higher number of layers. Other shear based exfoliation techniques such as high pressure homogenizers[26] and rotating blade mixers[27] have also been used to obtain graphene nanosheets.

Colloidal stability and separation of exfoliated pristine graphene

Even if exfoliation in liquid described above is successful, nanosheets are highly prone to re-agglomerate rather than remaining as a stable colloidal dispersion. It is somewhat difficult to separate the twin issues of exfoliation effectiveness and colloidal stability; shortcomings from either one will result in a low yield of stable, dispersed nanosheets. This is a critical issue because many papers in the prior literature focus on

only exfoliation effectiveness rather than both exfoliation effectiveness and colloidal stability.

The stabilization of nanosheets in solvents can be accomplished by reducing the nanosheet–liquid interfacial tension through various strategies such as usage of appropriate solvents or dispersant solutions (discussed below). After exfoliation, any nanosheets that are not colloidally stable will begin to aggregate and form heavier flakes with an increased number of layers. These reaggregated nanosheets and unexfoliated graphite flakes constitute a large fraction of the total graphitic material in the dispersion. In the dispersion, both Brownian and gravitational forces are acting on the dispersed materials. The large, unexfoliated material and aggregates will tend to form sediment over time (due to dominance of gravitational forces), while few-layer graphene nanosheets will remain suspended (due to dominance of Brownian forces). Thus, sedimentation allows for effective separation between stable colloidal graphene and other graphitic materials. The balance between these two forces determines which graphene nanosheets (in terms of layers, lateral size) may remain suspended for long times. Centrifuging a dispersion increases these settling forces, allowing for a more rapid separation process. Thus, high centrifuge speeds may result in lower equilibrium concentrations (and lower number of layers/nanosheet) in the supernatant; this is one of the prime causes of the quantity/quality tradeoff common to graphene dispersion processing.

The yield of the process can be calculated by measuring the amount of starting graphite and the concentration of graphene in the centrifuged dispersions (using UV–vis

spectroscopy). Exfoliation effectiveness may be determined by solvent type, sonication time, sonication power, while colloidal stability is determined by dispersant and/or solvent choice. Finally, separation effectiveness is determined by centrifugation speed and time. Collectively, these parameters affect both quantity (measured by the post-centrifugation concentration of nanosheets) and quality (lateral size, number of layers, defect density) of the as-produced graphene nanosheets.

Dispersant-assisted colloidal stability of graphene colloidal dispersions

Exfoliation of graphene in common, useful solvents (including water) can be facilitated by using a dispersant to prevent aggregation. Addition of surfactants, polymers and small organic molecules to such solvents can reduce the surface tension and facilitate exfoliation of graphite. Furthermore, adsorption of these dispersant molecules on the graphene surface assists the stabilization of exfoliated nanosheets and prevents reaggregation. Lotya *et al*. demonstrated that surfactant-based methods for CNTs could be extended to surfactant-stabilized graphene dispersions as well.[28] Since then, a variety of dispersants have been explored to yield high concentration graphene dispersions in water and organic solvents. Several groups have extensively studied the dispersion of graphene in water and organic solvents using various types of dispersants which include surfactants,[29-31] polymers,[32-34] and aromatic compounds.[35-39] These techniques yield highly concentrated dispersions (up to 1 mg mL^{-1}) of few-layer pristine graphene nanosheets in a range of solvents.

Various surfactants have been utilized as stabilizers for pristine graphene nanosheets, particularly for dispersion in water.[28,31,40-43] The hydrophobic tail of the

surfactant adsorbs onto the graphene surface via noncovalent interactions. The dissociation of the hydrophilic head of the adsorbed ionic surfactants creates a surface charge on the nanosheets. This surface charge (reflected in the zeta-potential value) induces an electrostatic repulsion between the graphene nanosheets covered with surfactant molecules. Both anionic surfactants and cationic surfactants have been used to disperse graphene nanosheets of 2–4 layers with ≈1 μm lateral size at a concentration of 0.1 mgmL^{-1}. Longer sonication time can improve the surfactant-stabilized graphene concentration and yield, but at the cost of decreased lateral size.

Nonionic dispersants (mainly polymers) may adsorb on graphene surfaces in order to lower interfacial energy; they stabilize graphene nanosheets through steric repulsion induced by their long hydrophilic heads spread into the water. Polystyrene (PS), poly(methyl methacrylate) (PMMA), poly(vinylpyrrolidone) (PVP), polyacrylamide (PAM), P-123, Triton X-100, and Brij-700 are a few examples of the polymers that assist exfoliation of few-layer graphene. Interestingly, these interactions are often nonspecific; for instance, molecular dynamics simulations show that PVP in water will migrate to the surface of both graphene and boron nitride nanosheets, allowing for stable dispersion in water.[44] Furthermore, the polymer-assisted graphene dispersions can be directly processed to fabricate polymer nanocomposites. Guardia *et al.*[42] and Smith *et al.*[43] reported that nonionic surfactants and polymers can produce graphene dispersions at higher concentrations than ionic surfactants.

One of the main issues associated with surfactant and polymer assisted dispersions is the excessive dispersant content in the final graphene product, chiefly

14

because the dispersant acts as unwanted or counterproductive diluent in the final graphene product.[28] Removal of excess dispersants in the liquid state is nontrivial.[45] Our group previously investigated techniques such as washing (under vacuum filtration) and dialysis, and although some excess dispersant (unattached to a graphene surface) may be removed, complete removal appears to be impractical.[46] Of course, successful attempts to remove or degrade the dispersant may also destabilize the dispersion.[47] Other studies of dispersant removal have been limited to annealing the dispersant after drying.

Polycyclic aromatic hydrocarbon (PAH) derivatives are promising alternatives to the use of high-concentration polymers and surfactants. These molecules have lower molecular weight than polymers and surfactants and are capable of stabilizing high quantities of graphene in aqueous dispersions via π–π interactions with the nanosheets. Various pyrene derivatives have been used to prepare high-concentration graphene dispersions ($\approx$1 mg mL^{-1}).[35,48-50] We studied the effectiveness of various pyrene derivatives as dispersants in detail, and the data indicate that the type, number, and the counterion of the functional groups affect the graphene yield and colloidal stability of the nanosheets in the dispersion.[35] Further, it was shown that the location of the functional groups affect the adsorption of the pyrene species on the graphene surface and the graphene concentration.[51]

Challenges in scaling-up graphene processing

Scalability may be understood by constructing a relationship for graphene production rate as a function of the exfoliation system size. One may undertake a

scalability analysis for each separate unit operation within the graphene production, with graphene synthesis (or exfoliation) distinct from graphene separation or handling units. For instance, recent reports have demonstrated that high-shear mixing can exfoliate nanosheets from the parent material with a power law relationship, described by the following equation:

$$P_R \sim V^\alpha$$

where P_R is the production rate, V is the volume of the exfoliation vessel, and α is a scalability exponent which depends on the choice of nanosheet, solvent, and dispersant.[52] The key issue is this: if α is greater than or equal to 1, then scaling up to large volumes becomes feasible from a manufacturing standpoint. If α is less than 1, then scaling up results in diminishing returns, and this approach will remain confined to small batch operations.

Paton *et al.* empirically determined values of $\alpha > 1$ for several dispersant/solvent combinations in shear-mixing exfoliation of graphene (as well as other nanosheets such as boron nitride nanosheets and transition metal dichalcogenides) by experimentally investigating exfoliation effectiveness as a function of exfoliation vessel parameters (such as initial graphite concentration, rotor speed, shear mixing time, rotor diameter).[52] This shows excellent promise for scalable exfoliation of pristine graphene from parent graphite materials in liquids. Notably, Paton *et al.* also approached the question of a recycle stream and demonstrated that the recycled graphite could be exfoliated with the same approximate yield as the "fresh" graphite. This indirectly implies that graphite is fairly homogeneous in its ability to be exfoliated.

Sonication produces high quality graphene in bulk amounts suitable for laboratory experiments. To achieve high yields long sonication times are required, however they are detrimental for the lateral area of graphene.[53] Khan *et al*. showed that the lateral size of graphene nanosheets reduce gradually with sonication time t, with a scaling law of lateral size trending with $t^{-1/2}$.[54,55] Moreover, sonication can only handle small volumes ($\approx$50–100 mL) of dispersion which limits the scalability of the method. The effectiveness of sonication diminishes with increasing dispersion volume ($\alpha < 1$); hence, alternative mechanical exfoliation schemes such as shear mixing are needed for scale-up.

One of the largest and most long-standing challenges in the area of nanomanufacturing is the need for scalable production techniques for nanosheets such as graphene, boron nitride nanosheets (BNNSs), and transition metal dichalcogenides (TMDCs).[56,57] These materials are prized for their unique properties and potential material applications in structural composites, functional papers, electronic devices, sensors, and photovoltaic films.[12,34,58-62] In the subsequent discussion, we focus on graphene as a model nanosheet, but we anticipate that our results are generalizable to the larger class of 2D materials.

In order to produce pristine nanosheets, a top-down approach is typically applied to exfoliate nanosheets from the parent material.[63-65] Liquid-phase exfoliation is a convenient top-down technique for processing nanosheets into functional films, gels, electrodes, or composites. Nanosheets tend to aggregate, so solvents and/or dispersants are chosen that may non-covalently functionalize the nanomaterial surface.[31,40,66,67] A

17

typical lab-scale exfoliation procedure is as follows: the parent material is added to a solvent (often containing a dispersant) and exfoliation is carried out by an external energy source such as sonication, shear mixing, or high pressure homogenization.[68-71]

Liquid-phase exfoliation typically produces a mixture of nanosheets with varying thickness, as well as unexfoliated parent material. The number of layers in nanosheets (directly associated with thickness) dictate the quality of the dispersion, so a secondary step is required to separate nanosheets based on their thickness. Centrifugation is a commonly used technique to separate nanosheets from unexfoliated or aggregated material; centrifugation is based on the relative magnitudes of Brownian and settling forces being exerted on the dispersed nanosheets in the dispersion. The thicker nanosheets and unexfoliated parent material are generally unstable and sediment upon centrifugation. In contrast, the thinner nanosheets remain well dispersed in the solvent and are eventually extracted with the supernatant.

Despite these advances, there are still persistent challenges to scalable, commercial production that need to be addressed. The low yield (mass of graphene product/mass of graphite feedstock) of few layered nanosheets obtained after centrifugation is particularly problematic. Typical yields reported in the literature for well dispersed pristine graphene nanosheets are < 2%.[72] Usually, low yields are attributed to difficulties in exfoliation, so numerous attempts to improve exfoliation have been reported recently; one notable study showed that despite low yields, exfoliation is scalable in industrial shear mixing.[73] However, we argue that not only difficulties in

exfoliation but also difficulties in separation are responsible for the low yield. Virtually no research has focused on improving yields through improved separation processes.

Attempts to decrease centrifugation speed or time result in higher graphene yields, but there is an associated quality tradeoff. However, prior studies have not examined whether centrifugation (or the associated sedimentation processes) can be improved by re-treating the sediment to recover additional graphene and increase yield. This is promising, given that sedimentation is widely used in industry to refine graphite ore in the pencil lead making industry. The issues of low yield and scalability of separation processes are yet to be addressed in the graphene community and are discussed in this study.

In this chapter, we have shown that the overall yield of nanosheet production processes can be improved by modifying the post-exfoliation separation process. We argue that heavier, unexfoliated parent materials are prone to trap exfoliated nanosheets during the gravity-induced sedimentation process, reducing the yield of nanosheets. We show that this trapped material can be recovered using wash cycles (mild agitation in presence of added solvent). This paper examines the mechanism of this trapping process, and also explores methods of recovering the trapped nanosheets. Using this recovery approach, we observed a drastic increase of >200% in our overall exfoliation yield.

2.2 Materials and Methods

Exfoliation

In the exfoliation step, graphite and PVP are added to water (200 mg/mL graphite, 40 mg/mL PVP, 100 mL water in a Fisher 250-mL beaker) and then shear

mixed with a Silverson L5M-A shear mixer at 8,000 rpm for 8 hours. After shear mixing, the dispersion was left to settle for 24 hours. During this settling time, the heavier unexfoliated parent material settles to the bottom of the vessel. The upper aqueous layer, containing well-dispersed graphene nanosheets, is removed and the sediment is stored for future use. During this removal process, updraft currents might pull some heavier graphitic material into the upper aqueous layer. To ensure that this unexfoliated material is removed, the extracted aqueous layer is centrifuged in a Fisher Scientific Sorvall ST-16 at 3300 rpm for 4 hours. The supernatant is then removed, the volumetric yield is measured, and the concentration of graphene is measured using a Shimadzu 2550 UV-Vis spectrophotometer as discussed in the next section (2.2).
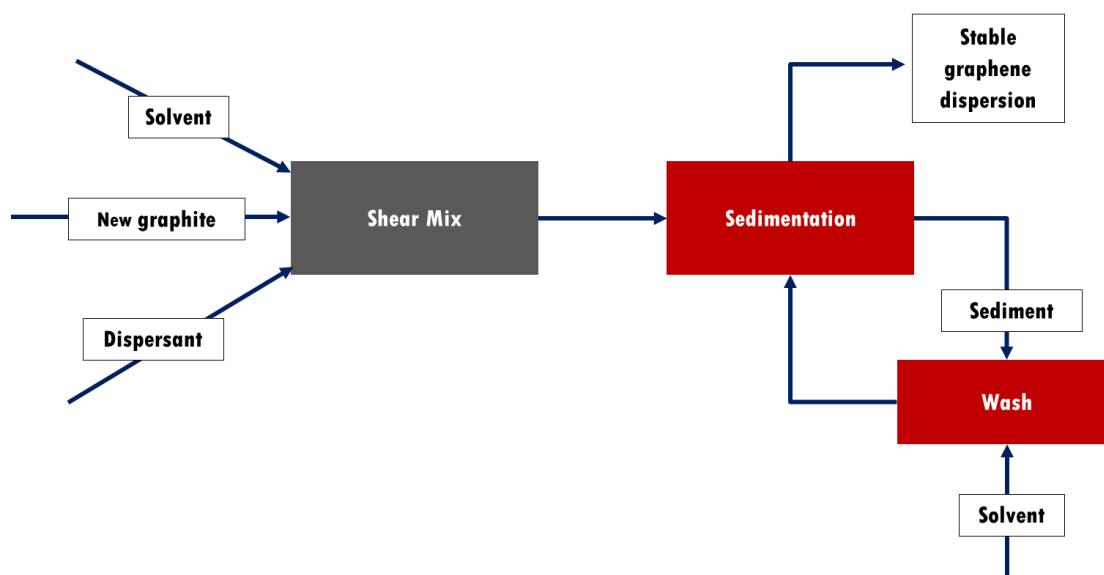
Figure 2.3 Schematic of graphene production and wash cycle. Reprinted with permission from Rountree et al.[2]

The previously mentioned settling process is repeated by adding fresh deionized (DI) water to the beaker containing sediment. To ensure consistency the volume of water

20

is chosen to be equal to the volumetric yield of the previous extraction. The sediment and fresh DI water are stirred together, allowed to settle for 24 hours, and this extraction-centrifugation process is repeated (As illustrated in **Figure 2.3**).

UV-Vis Spectroscopy

UV-vis measurements were carried out using a Shimadzu UV-vis spectrophotometer 2550, with a wavelength range of 200 nm to 800 nm. The concentration of graphene was determined by the Beer-Lambert law,

$$A = \alpha L c$$

where A is the absorbance of the solution at 660 nm[31], α is the extinction coefficient (1293 mL mg^{-1} m^{-1} for graphene-PVP dispersions[32]), L is the path distance of light through measurement cell, and c is the concentration of material in solution.

Dynamic light scattering

The particle size distribution of the nanosheets was determined at room temperature using dynamic light scattering by a ZetaSizer ZS90 from Malvern Instruments Limited. All the samples were diluted to a concentration of 0.05 mg/ml before measurements to ensure consistency.

Thermogravimetric analysis

For thermogravimetric analysis, the dispersion was dried using freeze drying (lyophilization) to form a powder. Thermogravimetric analysis was carried out using a TA Instruments Q50 to determine the PVP content of the freeze-dried powders. To remove moisture effects all samples were held at 50 °C for 30 minutes before the

analysis. The ramp rate for analysis was 5 °C/min from 50 °C up to 900 °C under an Argon atmosphere.

2.3 Results and Discussion

The purpose of this study is to examine (1) whether significant quantities of nanosheets are entrapped during sedimentation such that (2) recovery of nanomaterials from an exfoliated sample may be improved by adding solvent back to the settled sediment.

Graphene recovery and increased yield

We hypothesize that during sedimentation, unexfoliated/partially exfoliated graphite settles to the bottom of the vessel (taking some exfoliated graphene with it), while some of the stabilized graphene stays in the supernatant. To test this, a PVP-aided dispersion of graphene was made by shear mixing graphite and PVP in water for 8 hours. After shear mixing, the dispersion was left to settle for 24 hours. During this settling, a distinct supernatant was formed; this supernatant was removed and centrifuged for 4 hours to remove any sediment that may have been extracted with the supernatant. The mass of graphene recovered was measured by UV-vis spectroscopy and volumetric measurements. We attempted to recover additional graphene by adding solvent back to the graphite sediment and stirring thoroughly. The process is then repeated, as supernatant is extracted and treated as before. A single iteration of this process will be referred to as a "wash step."

The mass of graphene recovered from the wash steps are plotted as a function of total wash volume in **Figure 2.4,** with 37 mL of solvent for each wash step. The fact that

additional wash steps continue to yield additional graphene confirms the hypothesis that (1) graphene is indeed trapped by the graphite parent material during settling. This data demonstrates that (2) washing is feasible and effective in recovering significant quantities of graphene, although the amount of graphene recovered decreases with each extraction. The chemical engineering equivalent of such a recovery process in conventional distillation would be a "reboiler" to obtain a higher yield of the light product from the heavies, through multiple separation passes. In our case, the graphene dispersion is the light product obtained at the top. The unexfoliated graphitic slurry with entrapped graphene is the "bottoms" product. Each wash step is equivalent to a reboiler cycle which extracts more graphene from the bottoms at the expense of increased processing, solvent, and handling.
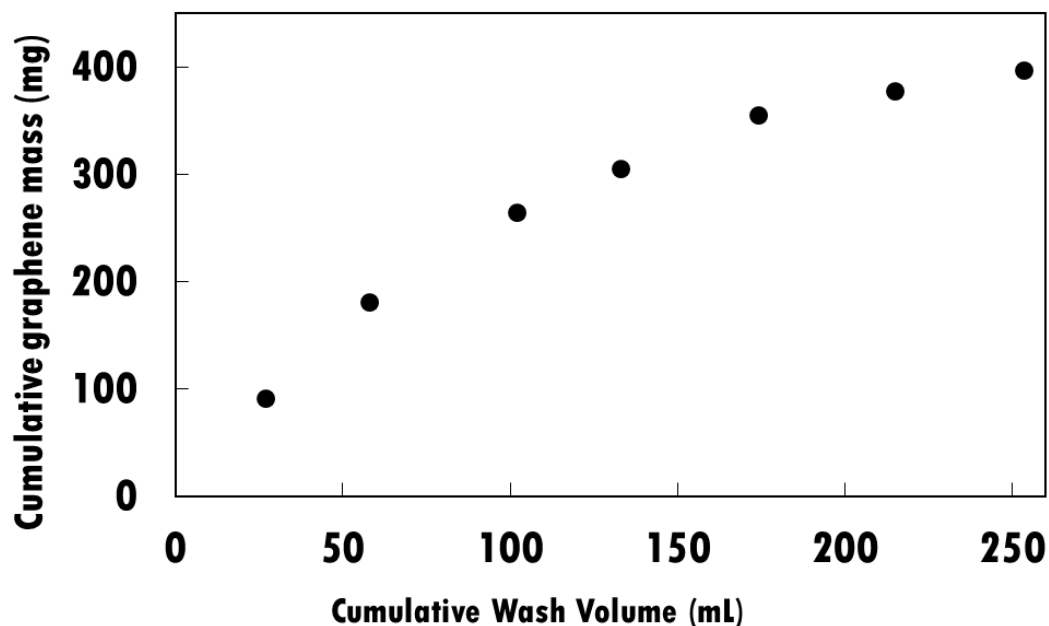
Figure 2.4 Variation of cumulative mass of graphene recovered with respect to the total wash volume. This data was obtained from an experiment with a wash volume averaging 37 mL per wash. Reprinted with permission from Rountree *et al.*[2]

This is somewhat surprising; one might assume that graphene in the sediment would be irreversibly aggregated. The data suggest that the graphene trapped by this process does not re-aggregate due to the dispersant present. (Adsorbed PVP is known to induce steric repulsion between dispersed graphene sheets.)[74] The wash process allows for the graphene trapped by graphite during the previous settling process to re-disperse.
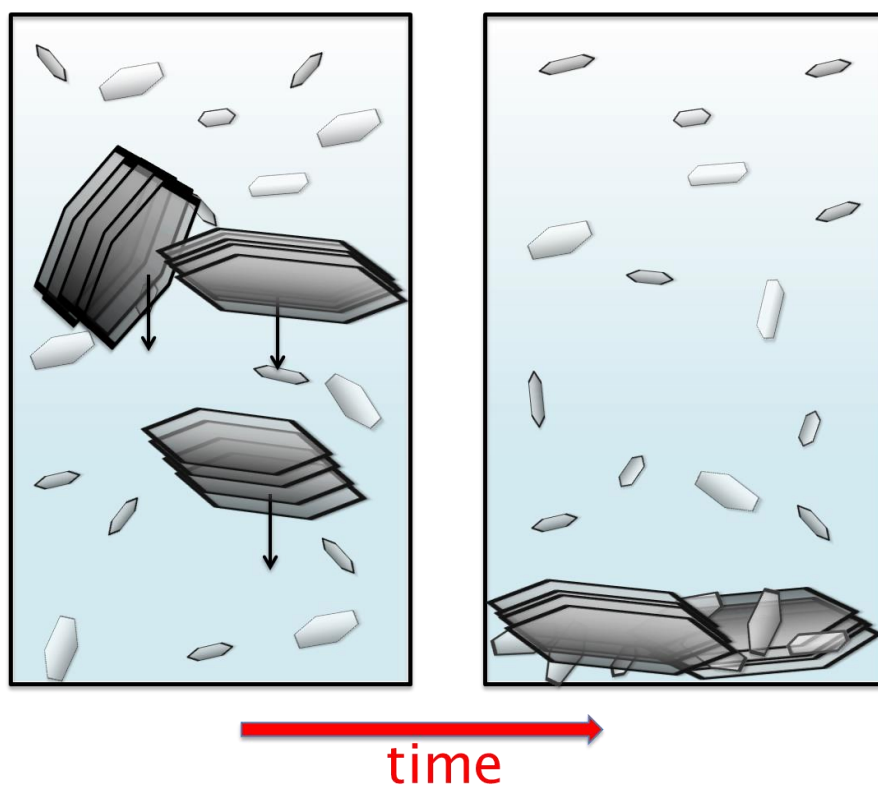
Figure 2.5 Conceptual illustration of our settling hypothesis. The large hexagons are flakes of graphite, and the smaller ones represent graphene. As time progresses, the parent material settles, and nanosheets are trapped under the parent material. Reprinted with permission from Rountree *et al.*[2]

Graphene recovery ratio

We argue that as graphite sediments, it has a probability of interacting with dispersed graphene sheets (illustrated in **Figure 2.5**). As the mass of unexfoliated

graphite in the vessel remains constant with each wash, the probability of interaction is constant. To investigate this phenomenon, we utilized the data from **Figure 2.4** to calculate the "graphene recovery ratio" (ratio of extracted graphene / available graphene) at each wash step. **Figure 2.6** shows that this fraction is approximately constant throughout the entire process. This supports the concept of the graphite-graphene interaction probability described above. From a chemical engineering point of view, this is analogous to tray efficiency, which describes the separation efficiency relative to an equilibrium (in our case, complete) separation between top and bottom products.
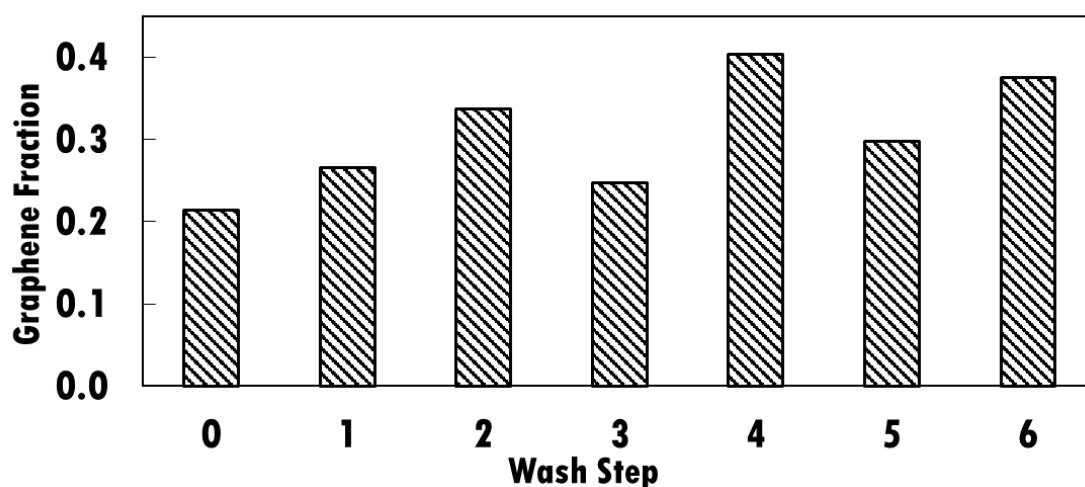
Figure 2.6 Graphene fraction (mass of graphene recovered/mass of available graphene) remains roughly constant with each wash step. The average wash volume was 37 mL per wash. Reprinted with permission from Rountree *et al.*[2]

Entrapment and graphene size

We hypothesized that if the entrapment process described above is correct, then graphene nanosheets with larger lateral size (which is correlated with hydrodynamic radius) would be more susceptible to entrapment by sedimenting graphite flakes. This

would mean that the smallest graphene sheets would be recovered in early wash steps, resulting in an increasing average lateral size over successive wash steps. To see if there was any correlation, DLS was used to measure the hydrodynamic radius distribution for each of the samples collected from the above experiments.[75] This peak hydrodynamic radius was measured for each wash and is shown in **Figure 2.7**. The data suggest that the hypothesis is correct, since peak hydrodynamic radius increases with increasing wash steps. This could potentially make size-selective extraction of nanomaterial feasible on a large scale.
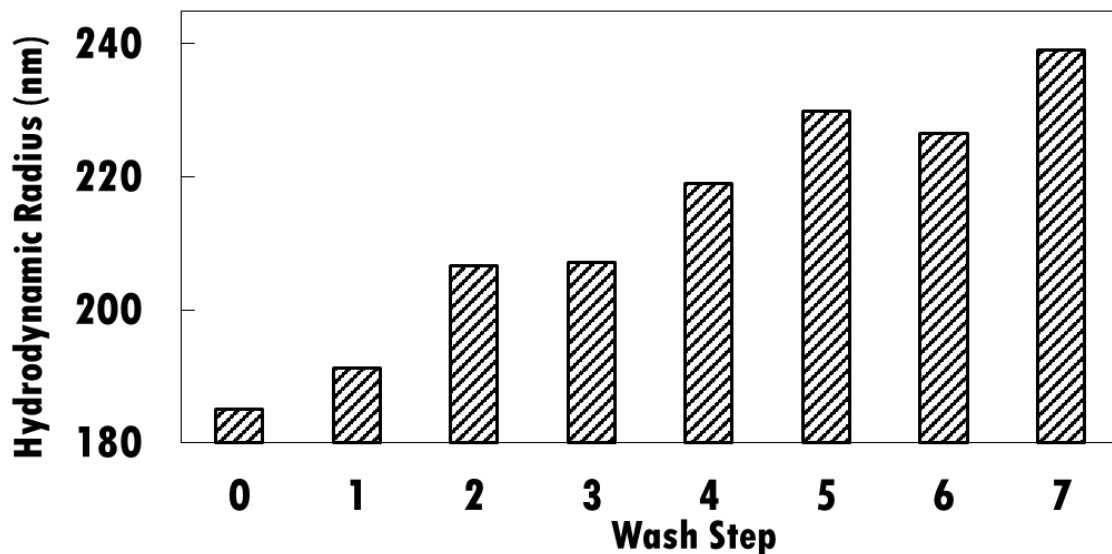
Figure 2.7 Hydrodynamic radius of graphene nanosheets for each wash step. Hydrodynamic radius increases with each subsequent wash. Reprinted with permission from Rountree *et al.*[2]

Improving graphene extraction

We then hypothesized that increasing the amount of solvent used to wash the graphite sediment should increase the quantity of graphene recovered, due to fewer graphene-graphite interactions. To test this, another shear mixed slurry was made, the

supernatant was removed, and 100 mL of water was used to wash the sediment, with similar 100 mL wash steps repeated afterwards. **Figure 2.8** shows that as solvent volume per wash increases, greater amounts of graphene are recovered per wash step. **Figure 2.8** also indicates that increasing wash volume maintains the same trend compared to the initial experiment. We concluded that the cumulative mass of graphene extracted is essentially a function of cumulative wash volume. From this, we can assume that an extremely large wash volume will recover almost all the available graphene in a single step.
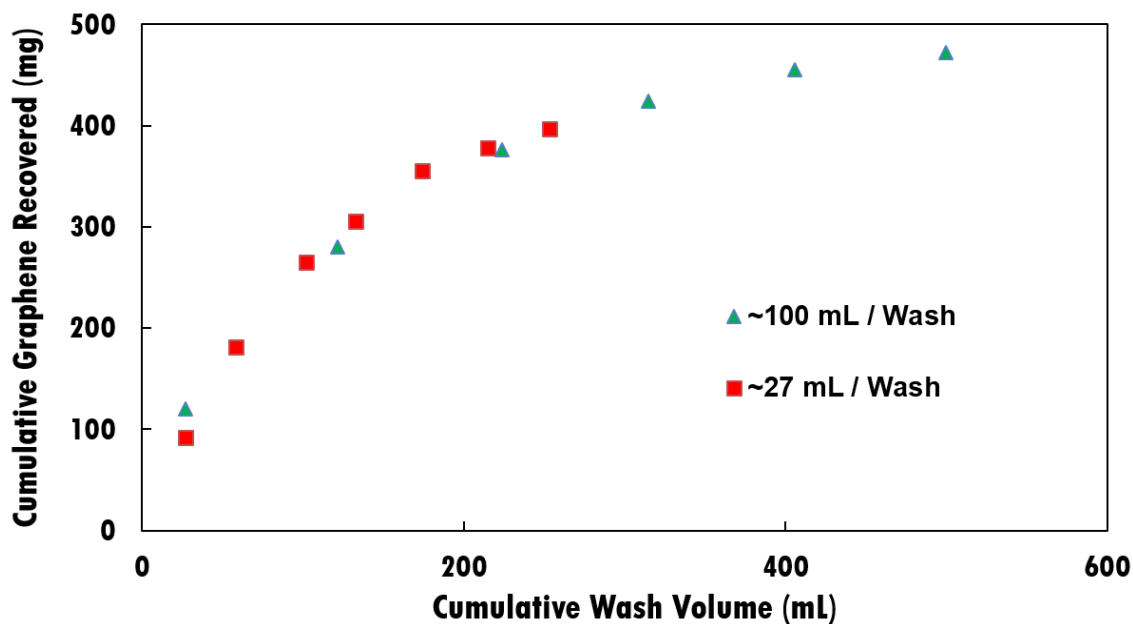
Figure 2.8 Cumulative graphene recovered vs. cumulative wash volume (comparing ~100 mL per wash with ~27 mL per wash). Fewer washes are required to recover the same quantity of graphene in the case of ~ 100 mL per wash. Both graphs seem to follow the same trend. Reprinted with permission from Rountree *et al.*[2]

Interestingly, the graphene recovery ratio does correlate with the ratio of supernatant water / total water available. This coheres nicely with the trends in **Figure**

2.4 and Figure 2.8 in showing that the dispersed graphene tracks with the solvent even when entrapped in sediment.

We also investigated the effect of graphite areal density (**Figure 2.9**); surprisingly, this parameter had little effect on graphene entrapment. If graphite areal density is dominant in determining graphene entrapment during sedimentation, this means that an increase in the cross-sectional area of the settling vessel should lead to an increase in the yield of graphene per wash, as the same amount of graphite covers a smaller portion of the settling area. To test this, the standard shear mixing process was carried out. After extracting the first supernatant, the sediment was placed into a 4 Liter beaker with a greater cross-sectional area and washed with 100 mL of water. Washes were subsequently carried out with same wash volume (~100 mL/wash). As can be seen in **Figure 2.9**, increasing cross-sectional area does not significantly increase the yield of graphene per wash. This implies that either the kinetic interaction mechanism while settling is not a dominant factor or it is not a strong function of the cross-sectional area.
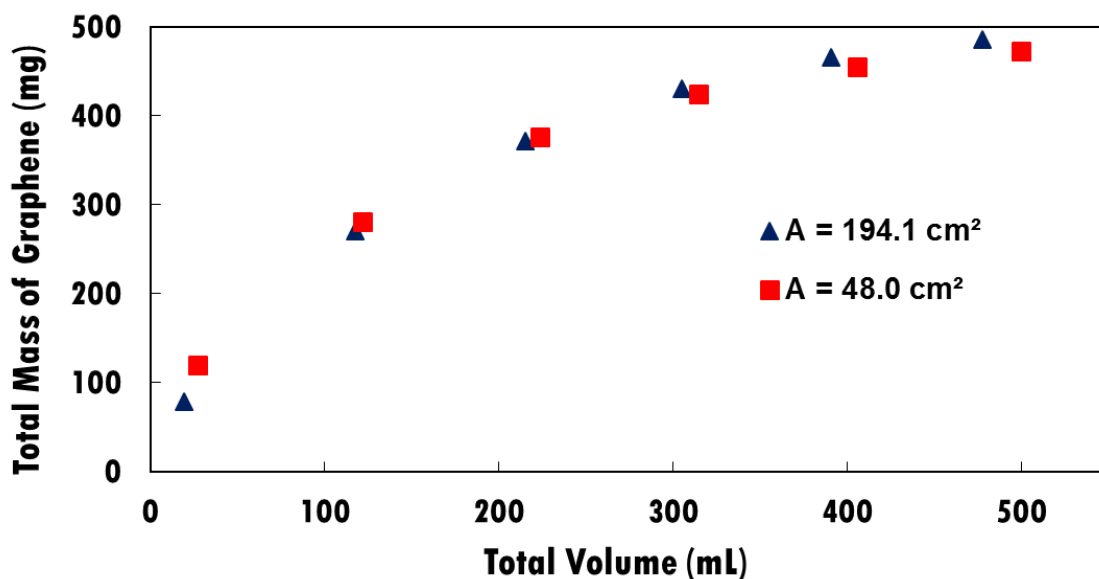
Figure 2.9 Comparison of graphene mass recovered with wash volume as a function of graphite areal density at constant volume/wash. Reprinted with permission from Rountree et al.[2]

Thermogravimetric analysis

To determine how such wash cycles decrease the total PVP content, the composition of the samples from the experiment described in section 3.4 was determined using TGA (**Figure 2.10**), with the data summarized in **Table 2.1**. This data show that the amount of free PVP in dispersion drops gradually with each separation step. The PVP content of a sample is estimated by measuring the drop in mass around 600° C, which is comfortably above the degradation temperature of PVP; the graphene is the remaining mass as temperature continues to increase. In "Wash 0", graphene constitutes only ~9.8% of the material in the sample, whereas in "Wash 4" graphene constitutes ~14.3% of the sample material. This occurs because a large majority of the free PVP is removed with the supernatant in the first separation step.
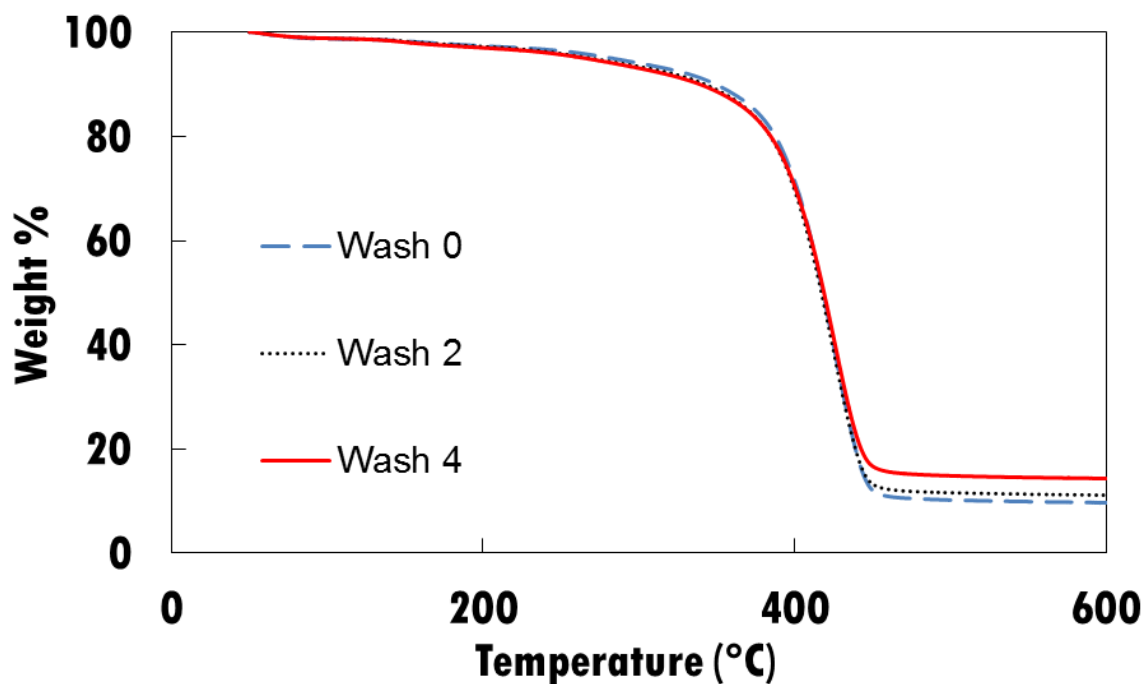
Figure 2.10 Thermogravimetric analysis of recovered graphene. "Wash 0" is sampled from the initial extracted supernatant. "Wash 2" is from supernatant extracted after 115 mL of water was added. "Wash 4" is from the supernatant after 235 mL of water was added. Reprinted with permission from Rountree et al.[2]

Table 2.1 Summary of thermogravimetric analysis, with reference temperature of 600 ºC. The ratio of PVP to graphene decreases with increasing wash steps. Reprinted with permission from Rountree et al.[2]

Wash Step	Graphene (wt.%)	PVP (wt.%)	PVP/Graphene
0	9.79	90.21	9.22
2	11.11	88.89	8.00
4	14.33	85.67	5.98

Extraction optimization

As discussed in section 3.4, we obtained higher graphene yield with larger quantities of solvent, but this higher graphene yield comes at the price of extra solvent processing and overhead costs on an industrial scale. The marginal increase in graphene yield reduces with increasing wash volume (**Figure 2.4**). One may devise an optimization algorithm to determine the optimum volume of solvent for graphene recovery, given the costs of solvent processing, precursor material, and graphene product.

Because the incremental increase in extracted graphene decreases with respect to wash volume, this suggests a "point of diminishing returns," such that there is an optimum wash volume based on processing and product costs. Our data in **Figure 2.8** suggest that the overall yield of the wash process is a direct function of cumulative solvent volume and is independent of solvent volume used in each individual wash. There is no added benefit to multiple washes, aside from time and space considerations for sedimentation.

The following assumption were made for the analysis. The settling time is not taken into consideration. We have chosen water as a solvent for this calculation. Its costs are negligible in comparison with other material and operation costs involved. For these reasons we have neglected the solvent cost in the calculation. The drier is assumed to operate with no material loss.

The optimization problem is framed as a function of solvent (wash) volume V as:

Total Profit (V) = [Graphene Mass (V) * Graphene Selling Price] –

$$[\text{Precursor Cost} * \text{Mass of Precursor}] - [\text{Drying Cost/volume} * V]$$

Graphene mass as a function of V is derived from **Figure 2.8.** We assume the following costs (as an example) for our calculation: Precursor cost = 1 ($/g), Graphene cost = 2 ($/mg), and drying cost = 450 ($/liter). The results are discussed in **Figure 2.11.**
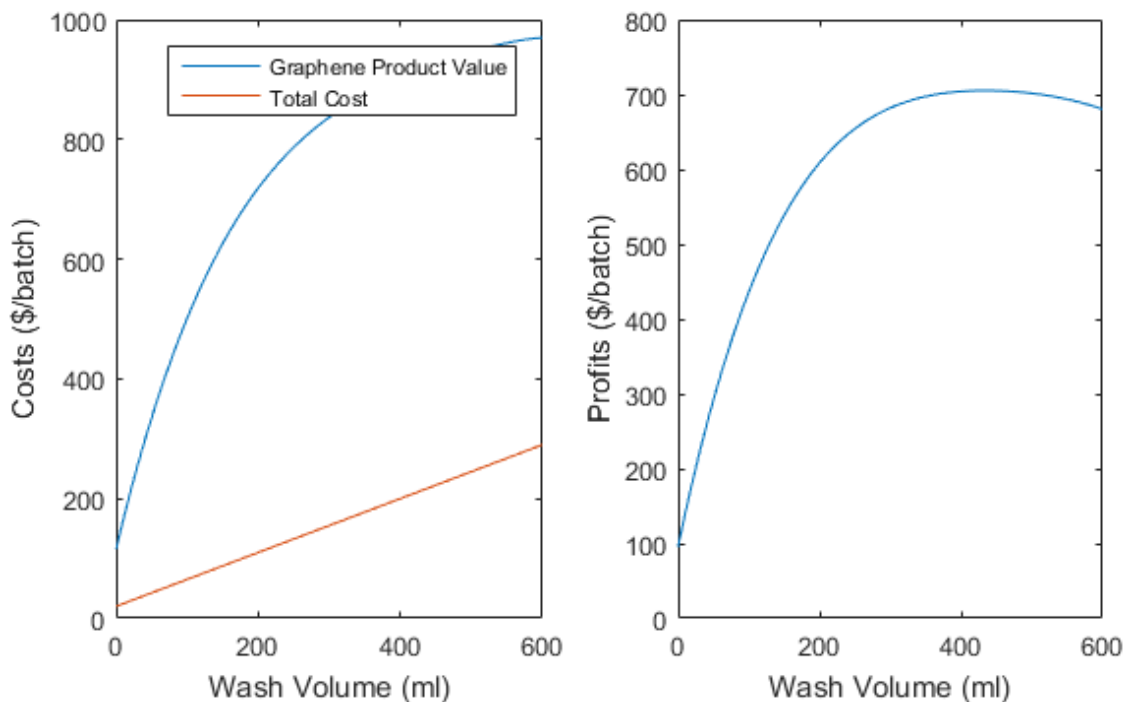
Figure 2.11 (a) Costs/batch as a function of wash volume. For a typical wash process, total costs scale linearly with wash volume as drying costs add up in proportion to the wash volume used; however, the graphene product value levels off at high was volume. (b) Profit/batch as a function of was volume. A maximum profit can be obtained by choosing an appropriate wash volume. This occurs at the point where the differential product value first goes below the slope of the total cost curve. Reprinted with permission from Rountree _et al._[2]

Applicability to other nanosheets

Additionally, we utilized the same washing process to investigate recovery of dispersed BNNSs (**Figure 2.12**). As can be seen in the figure, the experiment was successful in yielding additional BNNSs out of the sediment, suggesting that the

washing improves yield of nanosheets in general, not just graphene. Fundamentally, this indicates that this phenomenon of entrapment is universal to all nanosheets produced by liquid-phase exfoliation.
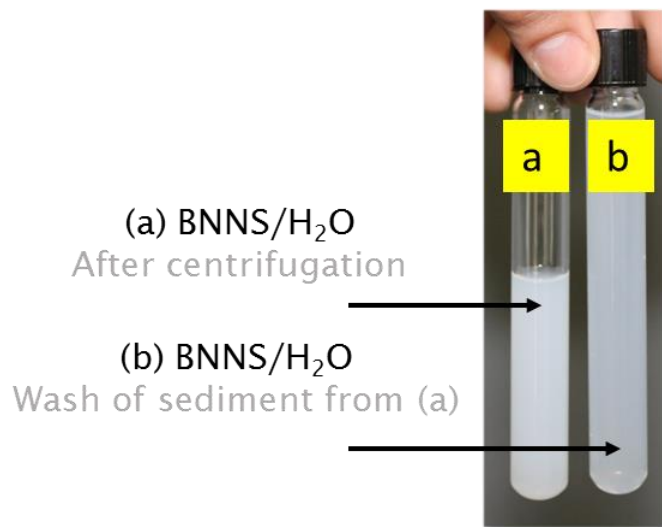
Figure 2.12 Photograph of a boron nitride nanosheet dispersion after centrifugation. As can be seen, boron nitride nanosheets were extracted from the sediment. This implies that washes can be used on nanosheet dispersions in general. Reprinted with permission from Rountree *et al.*[2]

2.4 Conclusions

We have demonstrated a simple and effective method of improving the yield of liquid-phase exfoliation processes. This technique uses simple sedimentation and reflux of solvent through the sediment; such methods can be easily carried out in industry. Our economic analysis showed that an optimal quantity of reflux solvent can be chosen for our method to maximize profits from a commercial standpoint. The concept of washes can be applied to other nanosheets such as MXenes and BNNSs as well. A possible streamlining of this process for industrial applications would be the use of a continuous

33

centrifuge,[76] which would separate the nanomaterial from the parent material based on particle size. This improvement of yield through a simple wash cycle brings large-scale graphene production one step closer to a reality.

CHAPTER 3

GRAPHENE QUANTUM DOTS AS DISPERSANTS FOR EXFOLIATION AND

STABILIZATION OF PRISTINE GRAPHENE NANOSHEETS[‡][§]

3.1 Introduction

As discussed in chapter 2, functionalized pyrene derivatives have been reported as dispersants for producing graphene dispersions because of their ability to stabilize graphene at high concentration/dispersant ratios in comparison with traditional surfactants.[77,78] By introducing repulsive solvation and/or electrostatic forces on graphene sheets, pyrene derivatives are able to prevent nanosheet aggregation and thus stabilize graphene in aqueous dispersion.[35,79,80]

The type and number of functional groups can play an important role in determining the quantity and quality of graphene dispersions prepared using pyrene derivatives. The exfoliation efficiencies of pyrene derivatives with amino groups ($-NH_2$), carboxylic groups ($-COOH$), and sulfonic groups ($-SO_3H$) were investigated under various pH values and processing conditions.[35] It was shown that functional groups with greater electronegativity can enhance the interaction between stabilizers and graphene layers. In particular, sulfonyl functionalized pyrenes produced stable colloidal dispersions for a broad range of pH values. Herein, we aim to demonstrate that the

---

concept of functionalizing pyrene as graphene dispersants can be generalized to larger polyaromatic particles (i.e., graphene quantum dots) acting as graphene dispersants.

Graphene quantum dots (GQDs) and carbon dots (CDs) are mono- or few-layered graphene sheets with lateral dimensions no larger than 0.1 μm, though GQDs have higher crystallinity.[81] In fact, GQDs possess aromatic cores and, with proper functional groups, can be expected to prepare stable graphene dispersions. GQDs with carboxylic groups (−COOH) have been used to stabilize commercial graphene powder by He *et al*. in 2014,[82] but a direct exfoliation of graphite into graphene by GQDs has not been discussed. Recently, an attempt was made to prepare graphene from graphite by using small-sized CDs (∼1.8 nm) with amino functional groups (−NH$_2$) to produce graphene aqueous dispersion.[83]

In this study, we evaluate graphene quantum dots with sulfonyl (−SO$_3^-$) functionalization (S-GQDs) and compared them against carboxylic functionalized GQDs (C-GQDs) and amine functionalized GQDs (N-GQDs) as dispersants for preparing graphene in aqueous solution. We show that the concentration of dispersed graphene depends considerably on polar functional groups present on the polyaromatic GQDs. We demonstrated that their functionalities affect the formation and stability of π–π stacking interactions that dictate the graphene exfoliation efficiency.

3.2 Materials and Methods

Materials

Citric acid monohydrate (99.5%) and 4-styrenesulfonic acid sodium salt (97%) were purchased from Sigma-Aldrich, USA. Expanded graphite was obtained from

Asbury Carbons (CAS no. 7782-42-5, grade 3805). All chemicals and solvents were used as received without further purification unless otherwise stated.

Synthesis of S-GQDs, N-GQDs, and C-GQDs

S-GQDs were fabricated by direct condensation and pyrolysis of citric acid and 4-styrenesulfonic acid sodium salt. In a typical procedure, 1.4 g of citric acid and 0.6 g of 4-styrenesulfonic acid sodium salt were mixed by a homogenizer. The white solid mixture was then transferred into a 20 mL glass vial and calcinated in air at 200 °C for 80 min. The dark solid residue was further purified by a dialysis tube (2000 Da) to remove possible unreacted starting materials. The final product S-GQDs were further dried by a freeze-drying machine. GQDs with amine functional groups (N-GQDs) and carboxylic acid groups (C-GQDs) were prepared based on previous works.[84,85]

Preparing aqueous dispersions of graphene nanosheets

Functionalized graphene quantum dots were utilized as dispersants. Specifically, 100 mg of dispersant was stirred into 50 mL of DI water at room temperature to obtain a uniform colloidal solution. We then introduced expanded graphite into the above solution, followed by 1 h of tip sonication (output wattage ~ 45 W) using a Qsonica sonicator (Q-700). To prevent the temperature of the sonication slurry from rising during exfoliation, we employed a water bath at ambient temperature. As-prepared sonicated slurry was allowed to settle for a day, and then centrifuged (Sorvall ST-16, Fisher Scientific) at 500–3300 rpm for 30–240 min to remove larger aggregates, and the supernatant was collected. This stable dispersion was used for further characterizations.

Characterization

TEM images were taken by a high-resolution transmission electron microscopy (HR-TEM, JEM 2010, JEOL). A ZetaSizer ZS90 (Malvern Instruments Limited) was used to conduct measurements of ζ potential at room temperature.

The concentrations of dispersions were measured using the Beer–Lambert law which states that the concentration of a dispersion is proportional to its absorbance. A UV–vis spectrophotometer (Shimadzu 2550) was used to perform UV–vis spectroscopy on aqueous dispersions for measuring their absorbance. Dispersant solution was used as a reference sample while measuring the absorbance of graphene dispersions to eliminate the contribution of stabilizer solution to the absorbance. To calculate the extinction coefficient of the graphene dispersion in water, a concentration versus absorbance calibration was performed at a wavelength of 660 nm. For calibration, the unknown concentrations of graphene dispersions were measured using a vacuum filtration assembly with a hydrophilic polytetrafluoroethylene filter paper (200 nm pore size). The differences in mass of the filter papers before and after filtration were used to calculate the nanosheet concentrations.

Aqueous graphene nanosheet dispersions stabilized with S-GQDs were analyzed using AFM to determine the thickness of graphene nanosheets and verify the presence of S-GQDs on their surface. Graphene dispersions were spin coated on freshly cleaved mica surface and were analyzed using tapping mode on AFM (Dimension Icon, Bruker).

3.3 Results and discussion

Morphology of functionalized GQDs

The morphology of S-GQDs was studied by transmission electron microscopy (TEM). **Figure 3.1** shows a typical TEM image of S-GQDs, showing the size of the as-prepared S-GQDs distributed in the range of 15–55 nm with an average diameter of 28.7 ± 5.4 nm. This size distribution is similar to that of other types of GQDs prepared by different methods reported in the literature. [86,87]
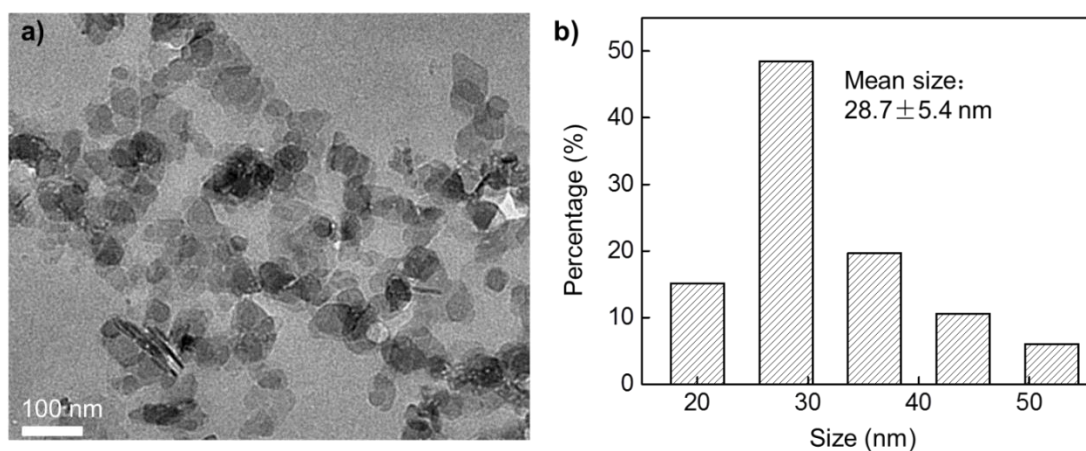
Figure 3.1 (a) TEM images of S-GQDs with scale bar of 100 nm. (b) Size distribution (Statistical Analysis) 28.7±5.4 nm. Reprinted with permission from Zeng *et al.*[3]

Sonication stability of GQDs

In order to explore the potential of S-GQDs as an exfoliation agent and dispersant for graphene, its stability was examined under tip sonication, as sonication is a commonly used method to facilitate liquid-phase exfoliation of graphite into graphene.[35] Tip sonication uses high energy sound waves which are generated by a piezoelectric actuator. To prove that the sonication process will not cause fragmentation

of S-GQDs, we compared the UV–vis spectra of S-GQDs before and after sonication for 1 h. As shown in **Figure 3.2a**, a bright blue luminescence of the S-GQDs aqueous solution (0.2 mg·mL^{-1}) under the illumination of a UV (365 nm) light is shown without any visible change before/after sonication. Moreover, as shown in **Figure 3.2b**, there is no discernable difference in absorption peak positions, indicating that GQDs are not altered by sonication. These results show that GQDs can tolerate sonication conditions required for exfoliating graphite into graphene.
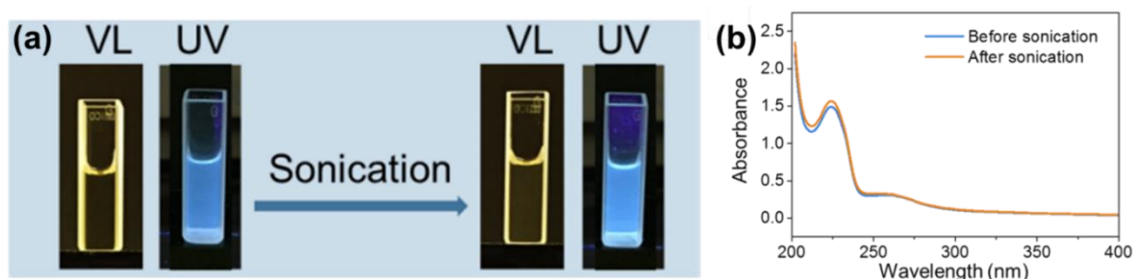
Figure 3.2 (a) Photographs of the S-GQDs in water under visible light (VL) and ultraviolet (UV, 365 nm) light before and after sonication. (b) UV–vis absorption spectra of S-GQDs before and after sonication. Reprinted with permission from Zeng *et al.*[3]

Direct Exfoliation of Graphite into Graphene

We then evaluated the capability of S-GQDs to stabilize pristine graphene exfoliated from graphite in aqueous solution. Tip sonication was used to achieve lab-scale liquid exfoliation of graphite to graphene, as shown in **Figure 3.3a**. For this study, we sonicated a slurry of S-GQDs and graphite dispersed in deionized (DI) water. As a result, graphite is exfoliated into a mixture of single- to few-layered graphene sheets (referred to as graphene nanosheets here onward) and multilayered (layers > 5) graphitic flakes.[88] The resulting slurry was centrifuged at 500–3000 rpm, causing the heavy

graphitic fractions to sediment, and the supernatant was extracted. In the extracted supernatant, the graphene nanosheet concentration was calculated to be 0.16 mg·mL^{-1} using UV–vis spectroscopy. This graphene concentration of 0.16 mg·mL^{-1} is comparable to that reported for graphene sheets prepared by direct exfoliation with surfactants, polymers, and polyaromatic hydrocarbons at the similar concentrations of stabilizers.[35,78,89] Such dispersions showed colloidal stability without any noticeable sedimentation and aggregation over a period of 30 days. The zeta potential (ζ) of this graphene dispersion was measured to be about −64.3 mV, indicating excellent colloidal stability.
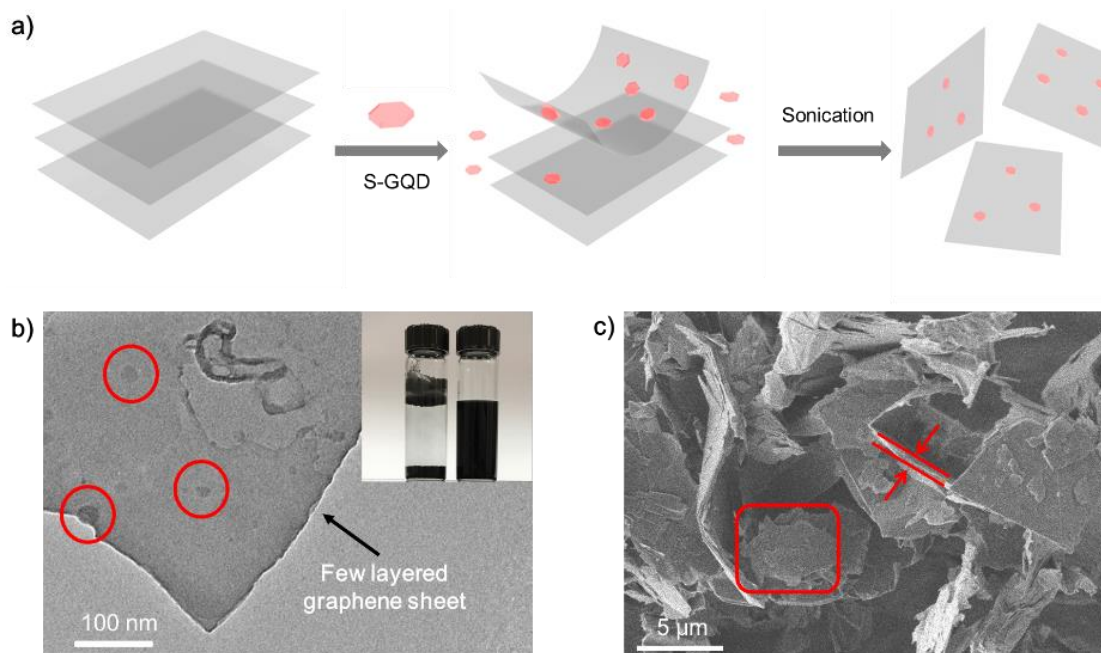
Figure 3.3 Exfoliation of graphite with S-GQDs. (a) Schematic illustration of the formation of S-GQDs-stabilized graphene. (b) TEM image of a few-layered graphene nanosheet stabilized by S-GQDs (red circles indicate S-GQDs); the inset shows colloidal stability comparison between aqueous graphite suspension (left) and aqueous graphene dispersion (right). (c) SEM image of expanded graphite (parent material). Reprinted with permission from Zeng *et al.*[3]

TEM was used to verify the presence of single- to few-layered graphene nanosheets in aqueous dispersions. As shown in **Figure 3.3b**, the S-GQDs-stabilized graphene nanosheets were estimated to be 2- to 5-layers thick by counting the layers at the graphene edges in TEM, which is common for sonicated graphene samples.[35] Atomic force microscopy (AFM) was performed on these S-GQDs-stabilized graphene nanosheets (**Figure 3.4a,b**). AFM height profiles were consistent with graphene nanosheets of 2–3 layers; these profiles also indicate the presence of the S-GQD dispersant. However, for starting material graphite, the SEM image shows a large lateral size around 5–20 μm with a thickness of 0.5–1 μm (**Figure 3.3c**), indicating that the exfoliated graphene sheets have much smaller lateral size with reduced thickness.
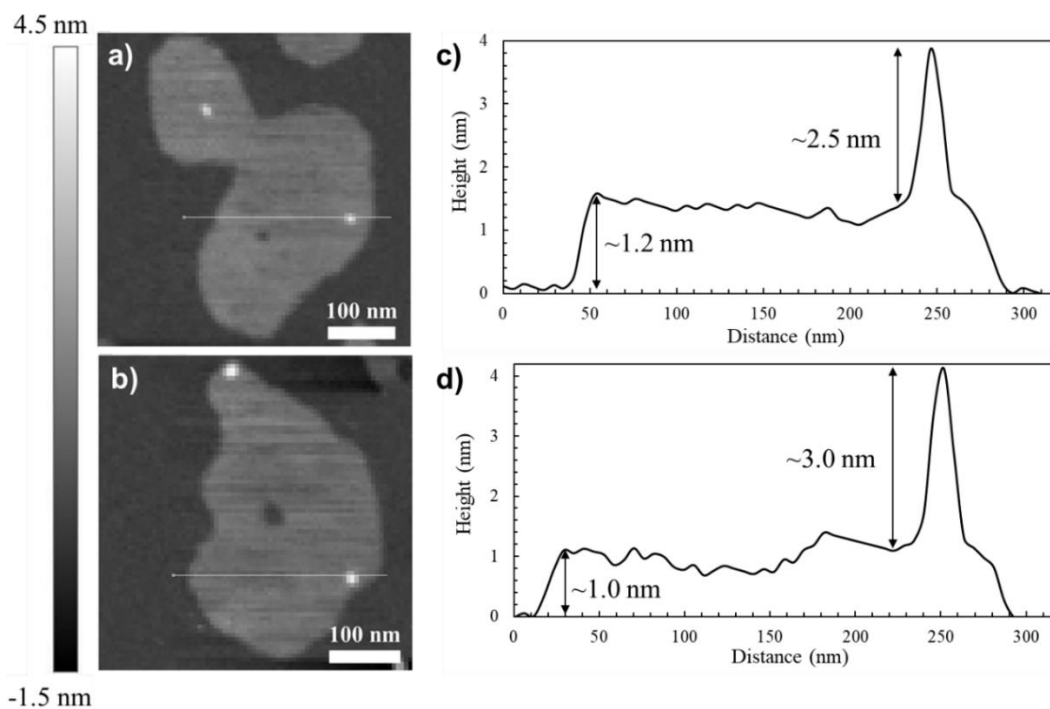
Figure 3.4 (a, b) AFM images of two graphene nanosheets with their color scale on left and (c, d) their respective height profiles on right indicating the presence of few-layered graphene nanosheets and S-GQDs. Reprinted with permission from Zeng *et al.*[3]

As seen in **Figures 3.4c,d**, the graphene nanosheets have a step height of ~1-1.2 nm which corresponds to 2-3 graphene layers.[90] The lateral size of S-GQDs are ~25 nm as expected. The step height of S-GQDs is ~2.5-3.0 nm, which may indicate local stacked aggregates (3-4 layers) of graphene quantum dots.[91]

Our prior work has shown that functional groups can influence the exfoliation efficiency of pyrene derivatives.[35] It was shown that the pyrene molecules functionalized by sulfonyl groups (1-pyrenesulfonic acid sodium salt) yielded much higher graphene concentration (~0.8 mg/mL) in comparison with carboxylic functionalized pyrene (1-pyrenecarboxylic acid) and amine functionalized pyrene (1-pyrenemethylamine hydrochloride), which yield graphene dispersions of about 0.4 and 0.1 mg/mL, respectively. This difference in dispersant performance among pyrene derivatives was shown to originate from the variation in their tendency for accepting π (pi) electrons from the sp^2 carbon of graphene. It was found that, as the electronegativity of the functional groups increases, π electron density in the aromatic rings of pyrene derivative decreases. This in turn will increase pyrene derivative's tendency of accepting π electrons from the sp^2 carbon of graphene.

In the current paper, we analyzed whether a similar functionalization-performance mechanism could also be applied for GQDs as a dispersant. Graphene quantum dots with amine functional groups (N-GQDs) and carboxylic acid groups (C-GQDs) were synthesized and studied. As shown in **Figure 3.5a**, N-GQDs were first examined at a graphite concentration of 0.5 mg/mL under sonication (45 W). It was

43

found that N-GQDs were able to disperse only a small amount (0.003 mg/mL) of graphene nanosheets after 240 min centrifugation. The stabilized graphene concentration is considerably lower than that of reported CQD with amine functional groups, likely due to the higher sonication power (800 W) and lower centrifugation time (30 min).[83] Moreover, when C-GQDs were used to prepare a graphene dispersion, the concentration was observed to be negligible. We believe that the reason behind their poor performance as dispersants in contrast to S-GQDs is due to the lower electronegativity of the carboxyl groups in C-GQDs and the amine groups in N-GQDs in comparison to the sulfonyl groups in S-GQDs. We also studied the effect of dispersant and initial graphite concentration on the final graphene yield. Upon increasing the initial graphite concentration, no significant change in final graphene concentration was observed when using C-GQDs and N-GQDs as dispersants. However, graphene concentration showed a clear upward trend with increasing graphite concentration. These results indicate that the S-GQDs are able to produce a more stable graphene dispersion in comparison with C-GQDs and N-GQDs.
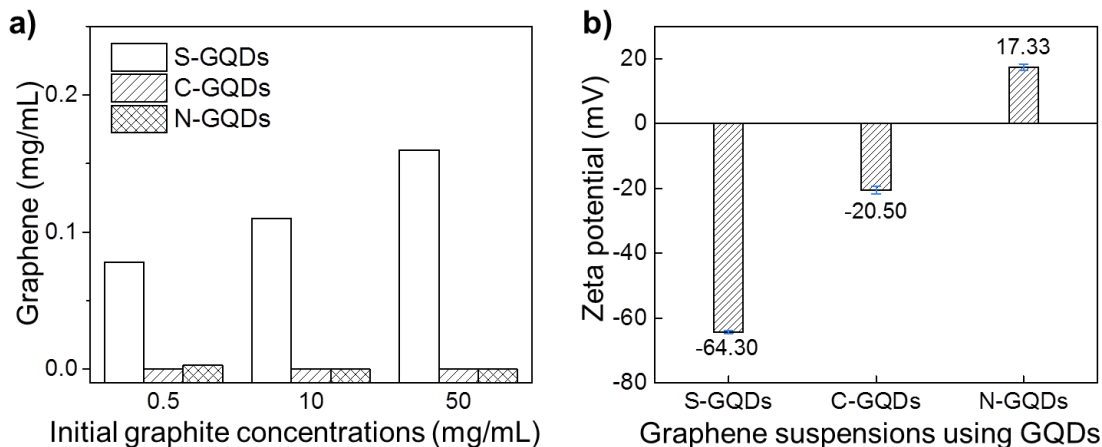
Figure 3.5 Exfoliation efficiencies with various GQDs. (a) Graphene concentrations prepared by N-GQDs, C-GQDs, and S-GQDs. (b) ζ potential values of exfoliation products by the aforementioned three types of GQDs. Reprinted with permission from Zeng *et al.*[3]

To understand the mechanism behind the different exfoliation efficiencies, we studied the colloidal stability of exfoliation products by measuring ζ potential values of exfoliation products. Generally, a suspension of nanoparticles exhibiting a higher absolute value of ζ potential would be more colloidally stable than suspensions with low ζ potential absolute values.[92] As shown in **Figure 3.5b**, it is obvious that the ζ potential absolute values of exfoliation products by C-GQDs and N-GQDs are relatively low (<30 mV), whereas a large surface potential ζ is observed for S-GQDs-stabilized graphene (>60 mV). The relatively low ζ potential values explain poor stability of graphene produced by C-GQDs and N-GQDs, resulting in extremely low concentrations of graphene after centrifugation. This trend is consistent with prior studies, where pyrenes functionalized with either an amino group or a carboxylic group produce graphene

dispersions with lower ζ potential values than those with a sulfonyl group.[35,51] It is worth noting that N-GQDs-stabilized graphene shows a positive potential value, likely originating from the amino functional groups of N-GQDs. These results suggest that S-GQDs-stabilized graphene nanosheets show excellent colloidal stability, making them suitable for the application of enhancing photonic devices' performance.

3.4 Conclusion

In summary, we showed that π–π stacking interactions with graphene are not limited to pyrene derivatives and perylenediimide,[37] but are also applicable to larger polyaromatic structures such as graphene quantum dots. The exfoliation efficiencies of GQDs with different functional groups were evaluated, demonstrating that only strong electron-withdrawing groups allow for effective stabilization of graphene dispersions. The mechanism could be explained by the polarization of the aromatic core of graphene quantum dots that facilitates π-electron sharing between graphene and GQDs.

CHAPTER 4

SYNTHESIS, AQUEOUS PROCESSING AND CRUMPLING OF MXENE

NANOSHEETS[**]

4.1 Introduction

MXenes are layered, two-dimensional structures with general formula of $M_{n+1}X_nT_x$ where M is an early transition metal, X is carbon and/or nitrogen, T is terminal group (-F, -OH, -O, etc.), x is number of terminal groups and n=1-3. Their metallic structure makes them highly electrically conductive, but they are also hydrophilic due to terminal groups on their surface layers. The latter, makes them easily dispersible in water, unlike many other nanosheet types.[93] Since the first MXenes were discovered in 2011, they have showed great promise for a wide range of applications including energy storage devices, batteries and supercapacitors, transparent electronics,[94-100] catalyst support,[101,102] lead absorption,[103] electromagnetic interference shielding[104,105] and water desalination[106] due to their unique dielectric, transport and chemical properties.[107,108]

There has been a significant interest in producing MXene-based 3D structures and 3D particles. Macroscale 3D structures have been formed by drop casting MXene nanosheet dispersions on a nickel template.[109] However, little is known about the possibility of directly altering MXene morphology to produce bent, scrolled, or

---

crumpled structures at the microscale, although there have been isolated reports of MXene nanoscrolls.[93,108,110]

One means to create such structures is to use capillary forces to locally bend nanosheets through spray drying.[44,111]; this has been recently demonstrated for graphene, boron nitride, and transition metal dichalcogenides. Dispersions of nanosheets are aerosolized, and the nanosheets are entrapped and compressed by capillary forces at the interface of the evaporating droplets.[44,111] Our prior work has shown that the mechanism of the nanosheet crumpling process is heavily influenced by the bending modulus of the nanosheets. This crumpled morphology prevents restacking and increases the porosity and accessible surface area of the resulting powder consisting of crumpled nanosheets. This, in turn, can highly improve electrochemical energy storage properties of 2D materials.[112-115]

In this work, we utilized a spray drying method to successfully demonstrate scrolling and crumpling of $Ti_3C_2T_x$ MXene nanosheets. We further demonstrate that the crumpling mechanism is strongly affected by (1) high bending stiffness of MXenes and (2) concentration of dispersed MXenes.

4.2 Materials and Methods

Synthesis of Ti₃AlC₂ MAX phase

Commercial Ti (44 μm average particle size, 99.5% purity), Al (44 μm average particle size, 99.5% purity) and TiC powders (2 – 3 μm average particle size, 99.5% purity), (all from Alfa Aesar, MA, USA), were used as starting raw materials to synthesize Ti_3AlC_2 MAX phase. To prepare homogeneous powder mixtures, Ti, Al, and

48

TiC powders were first weighed to achieve Ti:Al:C=3.0:1.2:1.8 ratio and mixed together using ball-milling with zirconia beads in a glass jar at the speed of 300 rpm for 24 hours. Then, the bulk high-purity Ti_3AlC_2 samples were sintered at temperature of 1510 ^{o}C for 15 mins with a loading of 50 MPa using Pulsed Electric Current System (PECS). This method is commonly, but inaccurately referred to as spark plasma sintering (SPS). To fabricate high-purity Ti_3AlC_2 powder, the PECSed sample was first drill-milled and sieved to obtain powder with particle sizes below 44 μm.

Synthesis of $Ti_3C_2T_x$ MXene clay

$Ti_3C_2T_x$ MXene clay was synthesized by etching aluminum from the MAX phase using technique described by Ghidiu et.al.[116] Concentrated hydrochloric acid (HCl, ACS reagent, 37% w/w Sigma-Aldrich) was diluted with DI water to obtain 30 mL of 6 M HCl solution. This solution was transferred to a polypropylene (PP) beaker and 1.98 gm of lithium fluoride (LiF, 98+% purity, Alfa Aesar) was added to it. This dispersion was stirred for 5 minutes using a Teflon (PTFE) magnetic stirrer at room temperature. Ti_3AlC_2 MAX phase powder was slowly added to the HCl+LiF solution to prevent overheating as the reaction is exothermic. The PP beaker was capped to prevent evaporation of water and a hole was made in the cap to avoid buildup of hydrogen gas. The reaction mixture was stirred at 40 ºC for about 45 hours. The slurry product was filtered and washed with deionized (DI) water in a polyvinyl-difluoride (PVDF) filtration unit with pore size of 0.22 μm (Millipore® SCGVU10RE Stericup™ GV) to remove the unreacted HF and water-soluble salts. This washing process was repeated

until pH of the filtrate reached a value of about 6. Reaction product collected over the PVDF filter is extracted as $Ti_3C_2T_x$ MXene clay.

Intercalation and delamination of $Ti_3C_2T_x$ MXene clay

$Ti_3C_2T_x$ MXene clay was intercalated with dimethyl sulfoxide (DMSO) and eventually bath sonicated to obtain an aqueous dispersion of delaminated $Ti_3C_2T_x$ MXenes following procedure described in more detail by Mashtalir et.al.[117] DMSO (ReagentPlus, >99.5%, Sigma-Aldrich) was added to $Ti_3C_2T_x$ MXene clay (dried in vacuum oven for about 24 hours at 40 ˚C) to form a 60 mg/ml suspension followed by about 18 hours of stirring at room temperature. After intercalation, excess DMSO was removed by several cycles of washing with DI water and centrifugation at 5000 rpm for 4 hours. The intercalated $Ti_3C_2T_x$ MXene clay suspension in DI water was bath sonicated for 1 hour at room temperature followed by centrifugation at 3500 rpm for 1 hour to separate the heavier components.

Crumpling of $Ti_3C_2T_x$ MXene nanosheet dispersion

Crumpling of $Ti_3C_2T_x$ MXene nanosheets was achieved by spray drying delaminated MXene dispersion.[111] Aqueous dispersion of delaminated $Ti_3C_2T_x$ MXene was diluted to a concentration of 1 mg/ml, and processed in Buchi B-290 mini spray dryer, **Figure 4.1**. The spray drying procedure involved conveying the dispersion using a peristaltic pump to an atomizer where it was mixed with in house air to form micrometer sized droplets. For our experiments, we used a pump flow rate of 10 % (of maximum possible flow rate) and atomizer air pressure of 60 psi. The droplets formed by the atomizer were carried and dried by co-currently flowing hot air in the drying chamber.

This airflow was created by an aspirator pump by induced draft mechanism and heating occurred via a heating coil. For our experiments, the highest drying air flow rate was used by operating aspirator at 100% power, and inlet air temperature was maintained at 220 ˚C. Carrier gas loses its heat to droplets causing water to evaporate and the dispersion to dry. The dried particles are eventually collected in a cyclone separator and are stored for further analysis. Above mentioned procedure was also carried out at a starting concentration of 0.1 mg/ml to analyze the effect of concentration on morphology of dried MXenes.
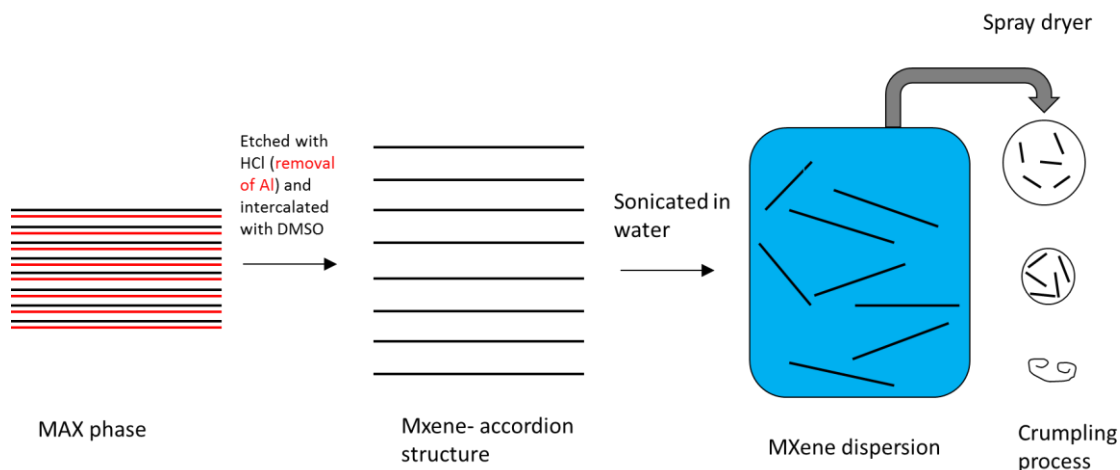
Figure 4.1 Schematic showing synthesis of $Ti_3C_2T_x$ nanosheets from parent MAX phase to nanosheet crumpling via spray drying. Layered MAX phase (Ti_3AlC_2) is etched using HCl + LiF to obtain $Ti_3C_2T_x$ clay. This clay is intercalated with DMSO and sonicated to obtain delaminated $Ti_3C_2T_x$ nanosheet dispersion. This dispersion is spray dried to obtain crumpled $Ti_3C_2T_x$ nanosheets. The crumpling process on the far right of the figure shows possible crumping mechanism for $Ti_3C_2T_x$ nanosheets. Reproduced with permission from Shah *et al.*[4]

Freeze Drying

Delaminated $Ti_3C_2T_x$ MXene dispersion was frozen in a freezer overnight and freeze dried for roughly 48 hours in Labconco FreeZone benchtop freeze dryer to obtain dry MXene nanosheet powder.

Transmission Electron Microscopy (TEM)

TEM images were obtained using FEI Tecnai G2 F20 field emission transmission electron microscope (FE-TEM). All samples were deposited on 200 mesh holey carbon-coated copper grids of 100 µm (HC200-CU-100, Electron Microscopy Sciences) for imaging. Powdered crumpled $Ti_3C_2T_x$ MXene samples from spray dryer were directly placed on the grid for imaging. Water rehydrated crumpled MXenes were drop casted on the grid followed by air drying for about 5 minutes.

Scanning Electron Microscopy (SEM)

SEM images were obtained using FEI Quanta 600 field emission scanning electron microscope (FE-SEM). For imaging, delaminated native $Ti_3C_2T_x$ MXene samples were prepared by drop casting their dispersion on a silicon wafer. Crumpled MXene samples were prepared by directly placing spray dried powder on carbon tape.

X-Ray Photoelectron Spectroscopy (XPS)

XPS measurements were performed using an Omicron XPS system with Mg x-ray source. Sample preparation for XPS was done by drop casting moistened crumpled $Ti_3C_2T_x$ MXene powder on hydrophilic (oxygen plasma treated) silicon wafer followed by drying in a vacuum oven overnight at 40 °C. Deconvolution was performed using CasaXPS software version 2.3.16.

X-Ray Diffraction (XRD)

Bruker D8 powder X-Ray diffractometer fitted with LynxEye detector, in a Bragg Brentano geometry with CuKα (λ: 1.5418 Å) radiation was used to obtain XRD patterns of powder samples. Freeze dried $Ti_3C_2T_x$ MXene powder was placed on a zero-background holder to obtain its XRD pattern. Similarly, crumpled MXene powder was also placed on the same holder to measure its XRD pattern. The X-ray scan was performed with a step size of 0.02º and a scan rate of 1 s per step.

UV-Visible Spectroscopy

Absorbance spectra of $Ti_3C_2T_x$ MXene dispersions were measured using Shimazdu UV-vis spectrophotometer 2550 (Wavelength range: 200 - 800 nm). Samples were placed in a quartz cell with path length of 1 cm, and DI water was used as a blank. Concentrations of MXene dispersions were determined using Beer-Lambert law. The extinction coefficient of MXene dispersions was calculated to be 1167.2 ml.(mg.m)$^{-1}$ at 580 nm. See **Figure 4.2** for more details.
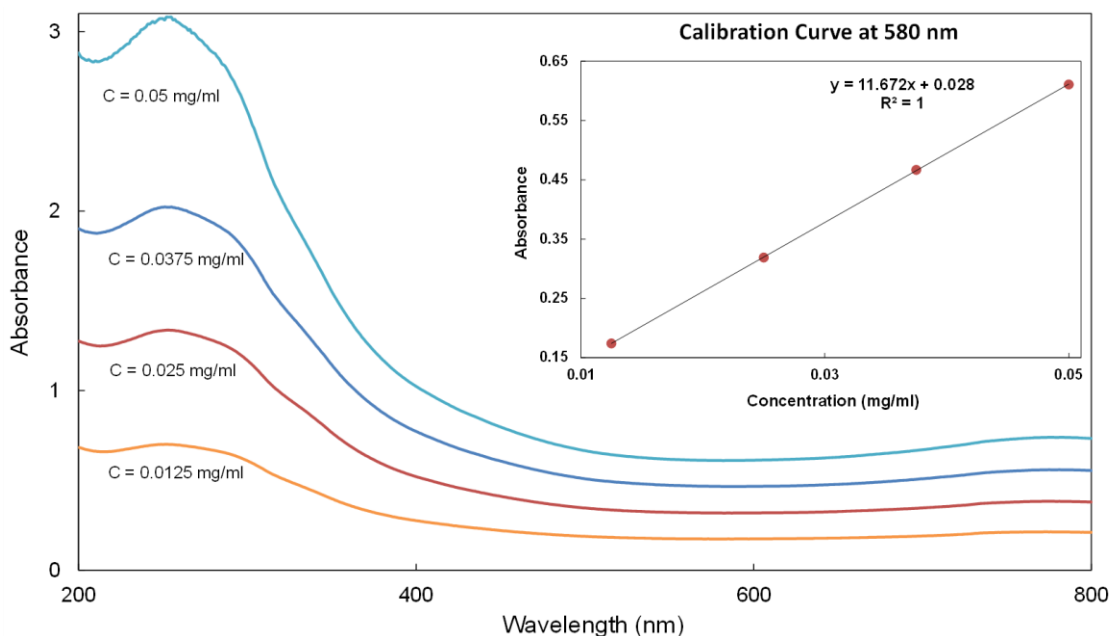
Figure 4.2 UV-Vis absorbance spectra are shown for $Ti_3C_2T_x$ dispersions at different concentrations (measured using vacuum filtration). Calibration curve (inset) was made using the absorbance values at 580 nm to measure concentration of subsequent $Ti_3C_2T_x$ dispersions. Reproduced with permission from Shah *et al.*[4]

Zeta Potential

Malvern Zetasizer ZS90 and the appropriate capillary cell (DTS1070) was used to measure the zeta potential of the stable $Ti_3C_2T_x$ MXene dispersions.

4.3 Results and discussion

Synthesis and processing of $Ti_3C_2T_X$ MXenes nanosheets

MXenes are derived from MAX phases by etching (using acid) out the "A" layer (a group 13 or 14 elements) from the layered MAX phases. Many MXenes have been reported experimentally and many more are expected to be stable but are yet to be synthesized.[118] For this study, the $Ti_3C_2T_x$ (MXene phase) was derived from Ti_3AlC_2 (parent MAX phase[119]) by etching Ti_3AlC_2 to remove Al. This is typically done using

54

concentrated HF aqueous solution; however, mixtures of LiF and HCl aqueous solution were recently shown to be effective as well.[116] We utilize this latter method in this study. After etching the A layer away, the $Ti_3C_2T_x$ structures possess a multi-layer accordion-like morphology.[93]

We then intercalate this structure with dimethylsulfoxide (DMSO) to aid in delamination. The DMSO was then solvent-exchanged to water and bath sonicated; the resulting dispersion was then centrifuged to eliminate unexfoliated material. The supernatant was collected as a colloidally stable few-layered $Ti_3C_2T_x$ nanosheet dispersion, with typical concentrations of ~1.5 mg/mL as measured by UV-vis absorbance. These colloids are stabilized electrostatically by the terminating groups, with typical ζ (zeta) potential values of approximately -32 mV (**Figure 4.3**).
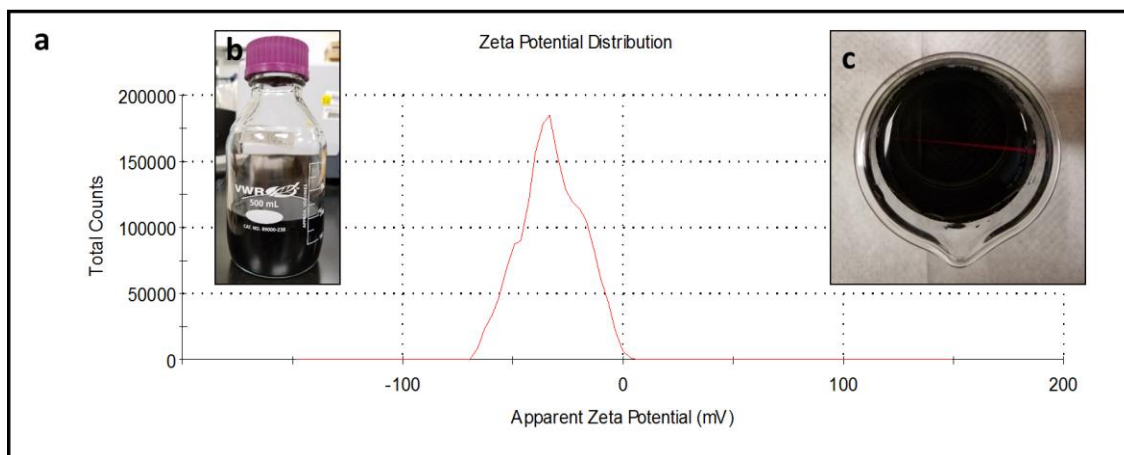
Figure 4.3 (a) Zeta potential of (b) aqueous $Ti_3C_2T_x$ nanosheet dispersion being stored in glass container shows its colloidal stability. (c) Colloidal nature of the dispersion can be verified by Tyndall effect (laser being scattered by dispersed MXene nanosheets). Reproduced with permission from Shah *et al.*[4]

The stable $Ti_3C_2T_x$ dispersion was diluted to a concentration of 0.1 mg/ml and fed to the spray dryer. The dispersion is aerosolized at an aspirator pressure of 60 psi and dried using in-house air as a carrier gas at 220 °C. The resulting dry powder is collected using a cyclone separator.

Crumpling of the nanosheets

As described above, the capillary forces on the evaporating droplets crumple the nanosheets during droplet evaporation. Scanning electron microscopy (SEM) images show clear distinctions in morphology between the native, flat MXene nanosheets (**Figure 4.4a**) and the crumpled nanosheet powder (**Figure 4.4b**).
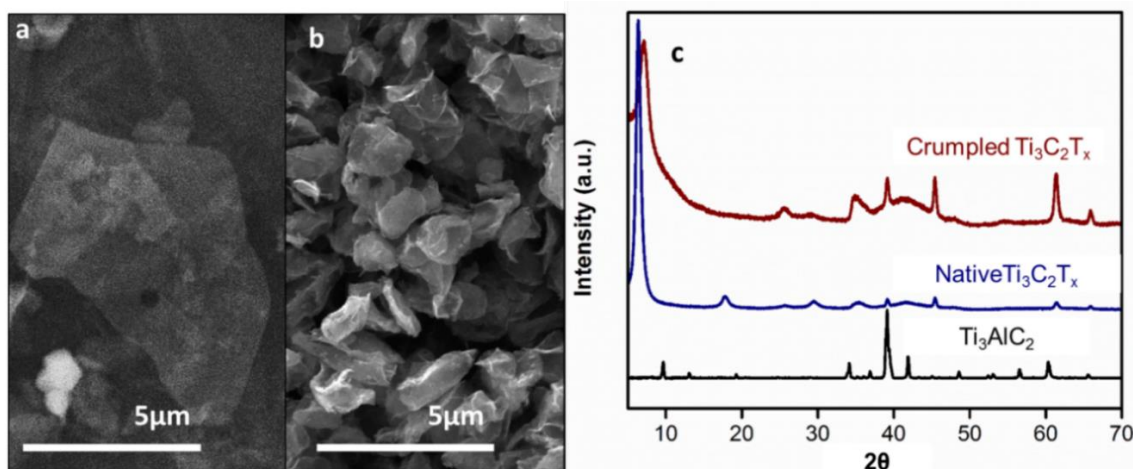
Figure 4.4 SEM images of $Ti_3C_2T_x$ MXene nanosheets in their (a) native and (b) crumpled morphology (spray dried at a concentration of 1 mg/ml), and (c) XRD spectra of Ti_3AlC_2 MAX phase powder, flat native $Ti_3C_2T_x$ MXene nanosheet powder, and crumpled $Ti_3C_2T_x$ MXene nanosheet powder. Reproduced with permission from Shah *et al.*[4]

XRD pattern of crumpled nanosheets

X-ray diffraction (XRD) patterns of these crumpled $Ti_3C_2T_x$ MXenes (spray dried) are compared to those of the flat, native $Ti_3C_2T_x$ MXenes (freeze dried) and the parent Ti_3AlC_2 MAX phase in **Figure 4.4c**. The initial etching process alters Ti_3AlC_2 to $Ti_3C_2T_x$, and the XRD spectrum for $Ti_3C_2T_x$ is consistent with prior studies, showing pronounced diffraction peak at around $2\theta = 6.3°$ - $7.1°$.[116,120] Comparison of position of XRD peaks for native and crumpled MXenes in **Figure 4.4c**, suggests that crumpling process does not appreciably affect the crystal structure of the nanosheets. However, the first peak (7.1°) for the crumpled MXene is broadened, most likely due to stresses induced by the crumpling process.

XPS analysis of the crumpled nanosheets

The composition of crumpled MXene powder was probed using X-ray photoelectron spectroscopy (XPS) analysis. Survey spectra (**Figure 4.5**) shows presence of titanium, carbon, oxygen and fluorine and the percentage atomic compositions are reported in **Table 4.1**. Peaks corresponding to sulfur, lithium or chlorine were not detected in the XPS spectrum, indicating that these species were removed in the final product. As shown in **Figure 4.6**, region corresponding to each element was deconvoluted and the results are listed in **Table 4.1**.
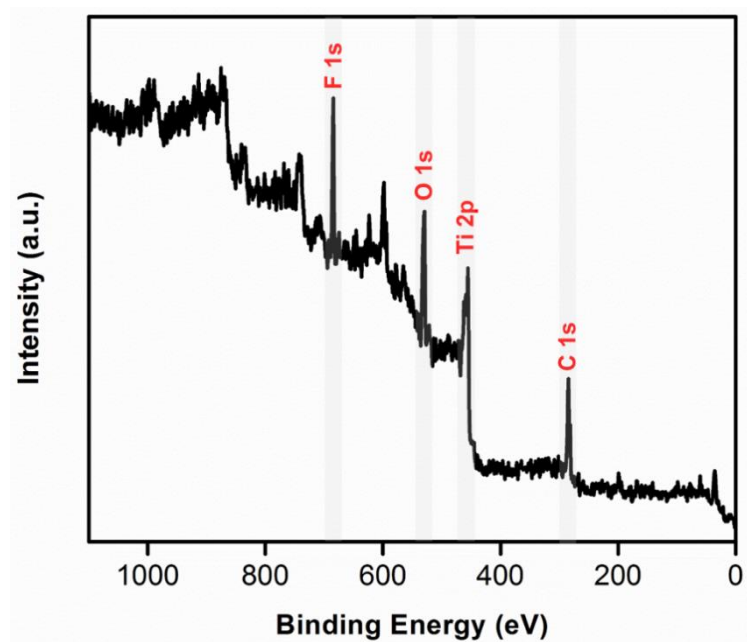
Figure 4.5 XPS spectrum of crumpled Ti₃C₂Tₓ MXenes labelled with characteristic peaks of Ti, C, O and F. Reproduced with permission from Shah *et al.*[4]
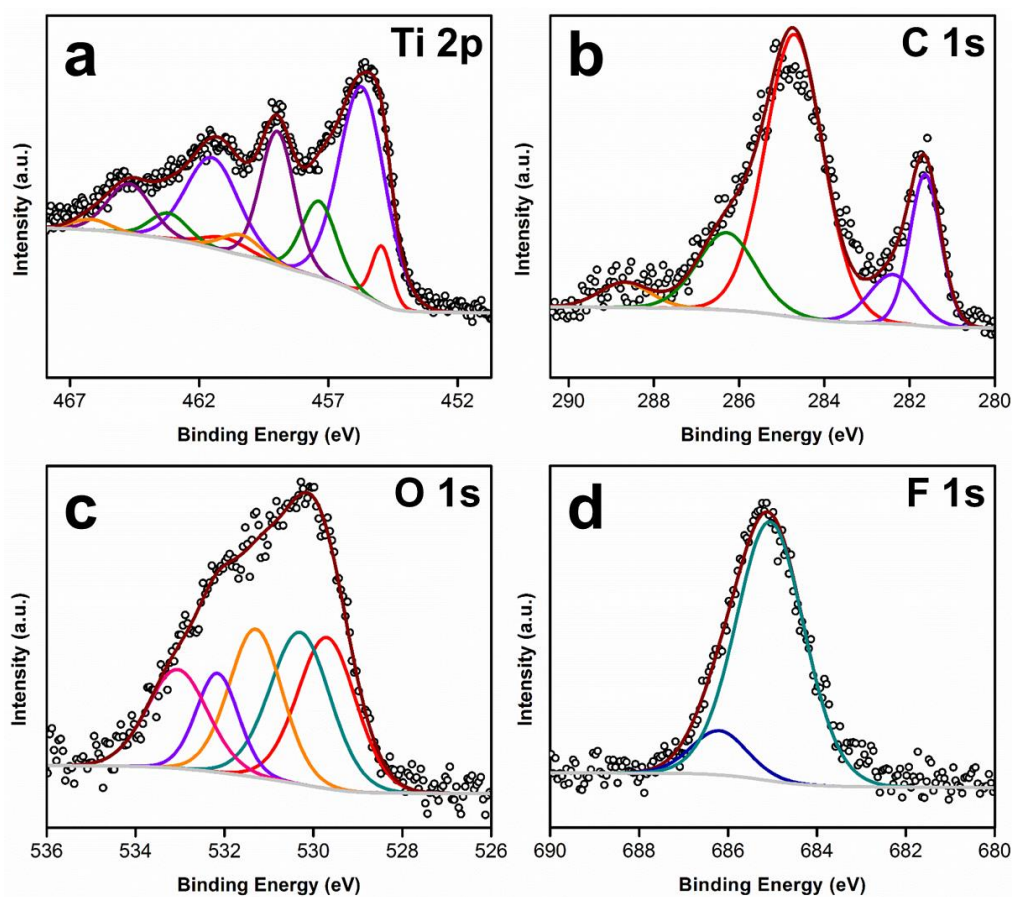
Figure 4.6 XPS spectra of crumpled $Ti_3C_2T_x$ MXenes. (a) Ti 2p (b) C 1s (c) O 1s (d) F 1s. Binding energy values of each bond associated with deconvoluted peaks are listed in Table 1. Reproduced with permission from Shah *et al.*[4]

Binding energy values of components were found to be in accordance with previous XPS studies on $Ti_3C_2T_x$ MXenes.[105,121-123] Our results indicated the presence of three type of surface functional groups on crumpled $Ti_3C_2T_x$ MXenes: oxide (-O-), hydroxyl (-OH) and fluoride (-F). 56% of carbon was composed of graphitic C-C which may have formed due to Ti etching during the MXene synthesis process.[124] About 25% of titanium was estimated to be oxidized to TiO_2.

59

Table 4.1 XPS peak fitting results for crumpled Ti$_3$C$_2$T$_x$ MXenes. Reproduced with permission from Shah et al.[4]

Element	Overall Atomic %	Component Name	Component Atomic %	BE (eV)	FWHM (eV)
Ti 2p$_{3/2}$ (2p$_{1/2}$)	18.21	Ti-C	6.30	454.9 (461)	0.9 (2)
		Ti^{2+}	51.94	455.7 (461.5)	2.1 (2.4)
		Ti^{3+}	13.04	457.4 (463.2)	1.6 (1.7)
		TiO$_2$	24.49	459 (464.7)	1.6 (2)
		C-Ti-F$_x$	4.23	460.4 (466.2)	1.8 (1.7)
C 1s	43.88	(†) C-Ti-T$_x$	23.97	281.6	0.8
		(†) C-Ti-T$_x$		282.4	1.3
		C-C	56.23	284.7	1.6
		CH$_x$/CO	15.37	286.3	1.6
		COO	4.43	288.7	1.4
O 1s	25.33	TiO$_2$	24.45	529.7	1.5
		C-Ti-O$_x$	25.46	530.3	1.6
		C-Ti-(OH)$_x$	21.89	531.3	1.4
		Al$_2$O$_3$	11.62	532.2	1.1
		(*)H$_2$O	16.58	533.1	1.6
F 1s	12.58	AlF$_x$	12.29	686.2	1.5
		C-Ti-F$_x$	87.71	685.1	1.8

† T$_x$ represents MXene terminal groups. The peak corresponding to this bond is asymmetric and is here it is represented by two symmetric peaks.

* Water molecules associated with –OH terminal groups.

Effect of MXene dispersion concentration on degree of crumpling

At higher MXene concentration in the feed dispersion, the degree of crumpling in the as-obtained powder is significantly decreased, as seen in **Figure 4.7a, b.** This trend may be explained as follows: with increased concentration, the number of nanosheets per

droplet increases, such that multi-nanosheet shells may form during evaporation. These thicker nanosheet shells would have a higher effective bending modulus and crumple less than shells with fewer nanosheets, resulting in a less compact structure. Inspection of the crumpled nanosheet edges reveal far fewer nanosheets in **Figure 4.7a** (0.1 mg/mL) than in **Figure 4.7b** (1 mg/mL). Similarly, at the edges of the structure, there is a significant degree of scrolling rather than crumpling in **Figure 4.7b**. This presents a possible route to control the morphology of dry MXene nanosheets. We also compared the effect of out-of-plane bending modulus of $Ti_3C_2T_x$ MXenes with other nanosheets such graphene oxide (GO) (**Figure 4.8**). The increased number of atomic layers (5) would result in a higher stiffness of MXenes when compared to the single-layer GO. More TEM images of crumpled MXenes from dispersion spray dried at concentration of 0.1 mg/ml and 1 mg/ml are shown in **Figure 4.9** and **Figure 4.10** respectively.
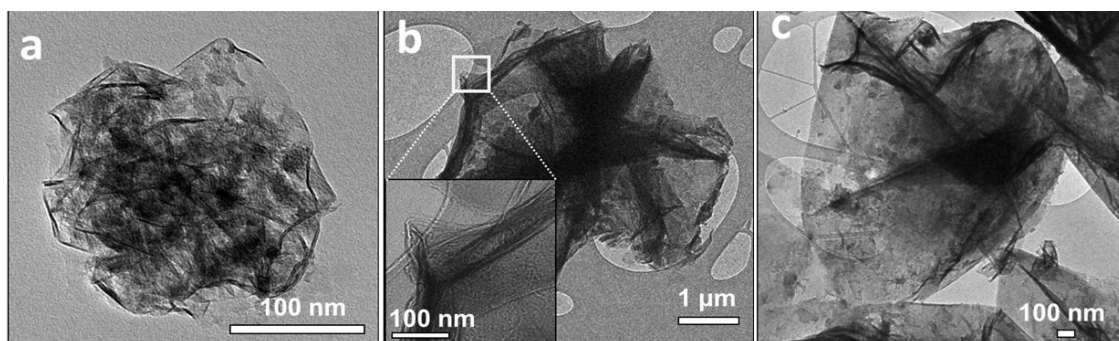
Figure 4.7 TEM images of crumpled $Ti_3C_2T_x$ MXene spray dried at a concentration of (a) 0.1 mg/ml, (b) 1 mg/ml [zoomed in inset shows few layers and scrolling] and (c) "rehydrated" crumpled MXene from dispersion spray dried at 1 mg/ml. Reproduced with permission from Shah *et al.*[4]

61
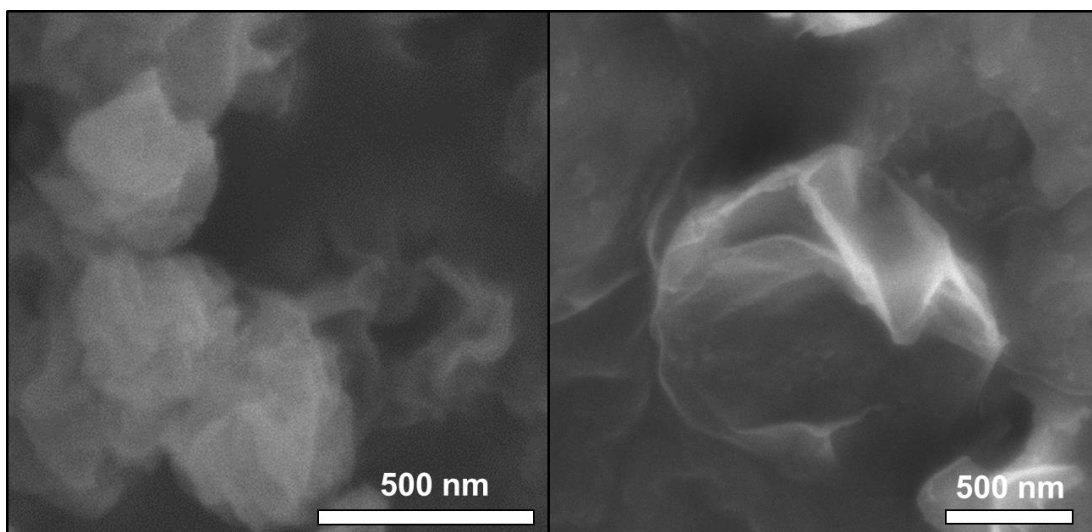
Figure 4.8 SEM/TEM images of (a) crumpled GO and (b) crumpled Ti$_3$C$_2$T$_x$. Crumpled GO shows significant number of ridges whereas crumpled Ti$_3$C$_2$T$_x$ shows folds with relatively larger local radius of curvature. Reproduced with permission from Shah *et al.*[4]
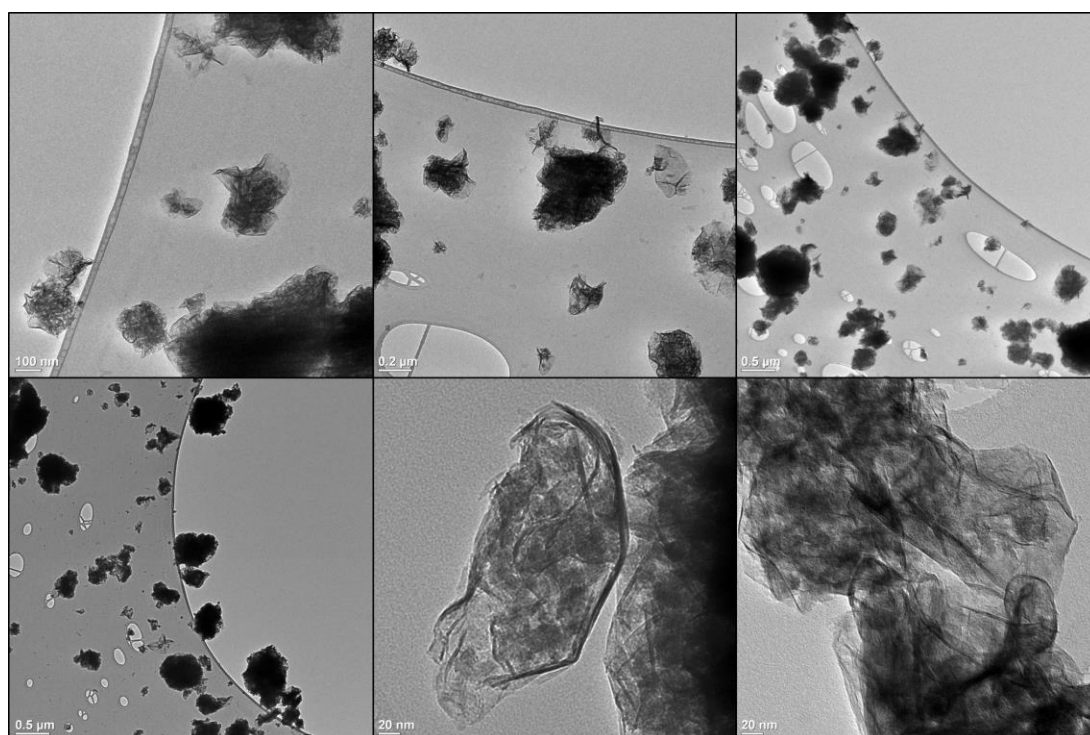
Figure 4.9 TEM images of crumpled Ti$_3$C$_2$T$_x$ spray dried at a concentration of 0.1 mg/ml. Reproduced with permission from Shah *et al.*[4]
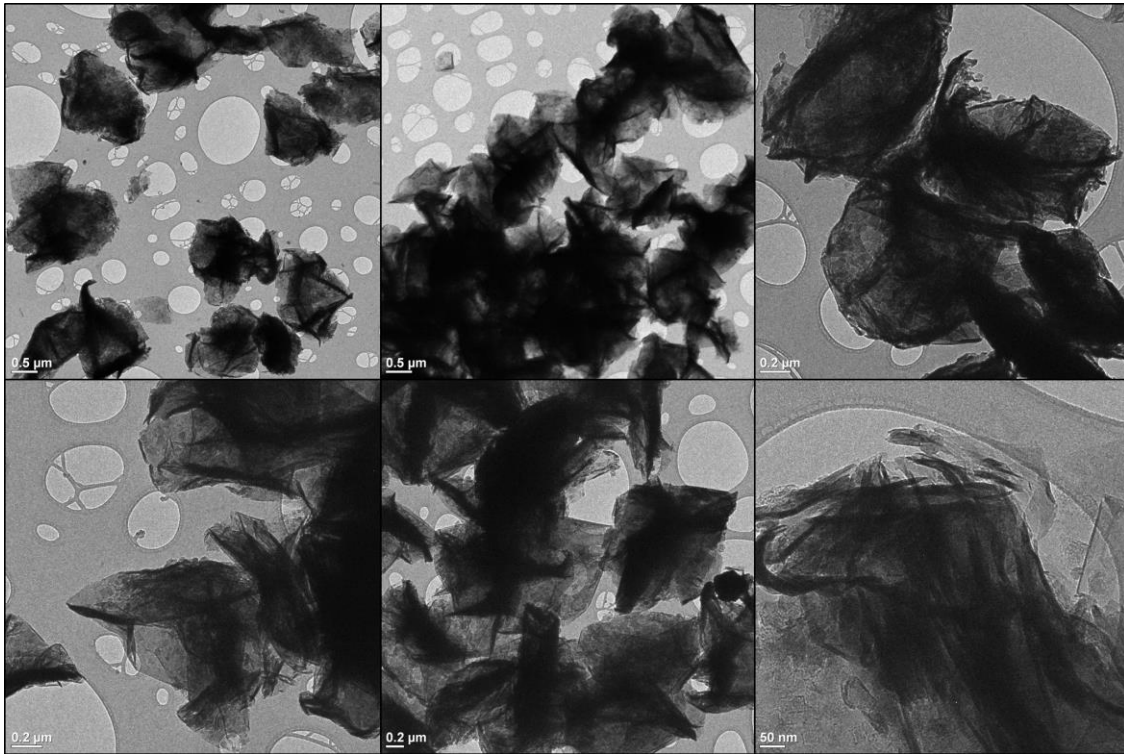
Figure 4.10 TEM images of crumpled Ti₃C₂Tₓ spray dried at a concentration of 1 mg/ml. Reproduced with permission from Shah *et al.*[4]

Uncrumpling of the nanosheets on rehydration

To determine whether this crumpled morphology is reversible, crumpled Ti₃C₂Tₓ was rehydrated in water using a vortex mixer and allowed to settle for two hours. The supernatant was drop cast on a TEM grid and analyzed. From **Figure 4.7c**, the lack of folding, bending, and scrolling sites indicates that this structure has "uncrumpled" to a state closer to the pristine MXenes. This indicates (i) that the capillary forces induce few permanent defects or covalent bonds in the MXene structure and (ii) that the MXene structure remains hydrophilic due to terminal groups on the nanosheet surface, even after crumpling. The latter point is confirmed by the XPS data showing presence of C-Ti-OH

63

terminal groups and C-Ti-O$_x$ sites after rehydration of crumpled MXenes. More TEM images of rehydrated crumpled MXenes spray dried at a concentration of 1 mg/ml are shown in **Figure 4.11**.
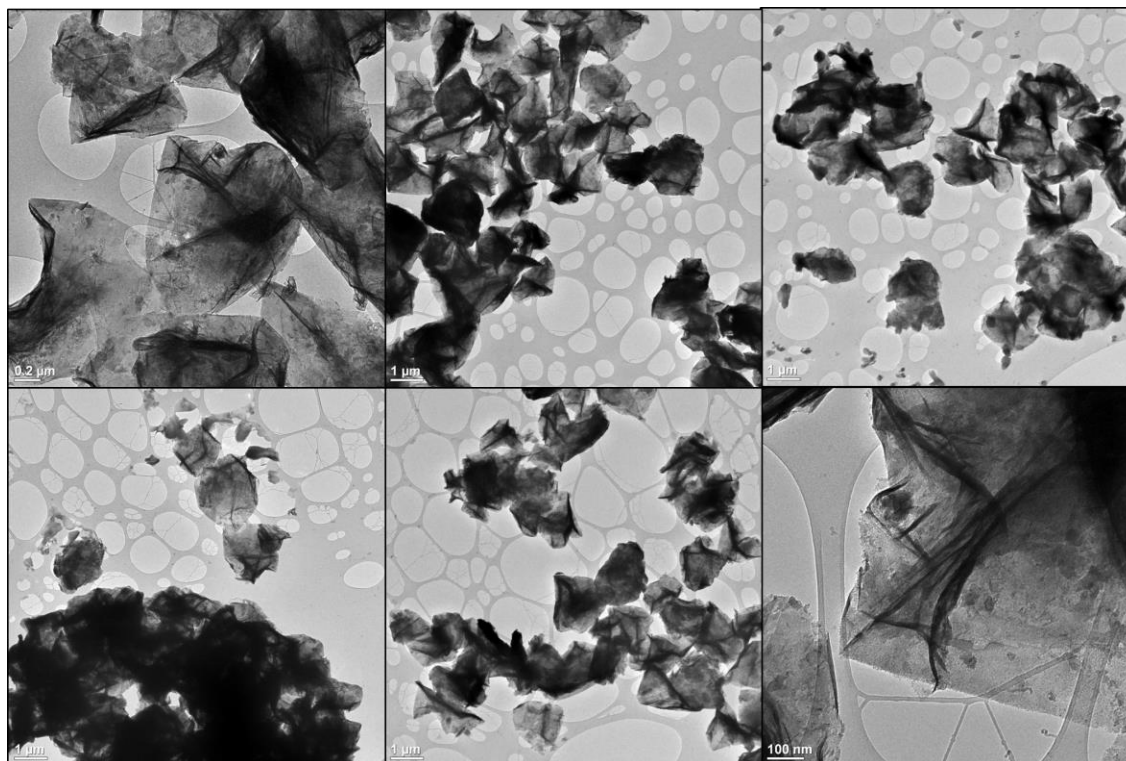
Figure 4.11 TEM images of "rehydrated" Ti$_3$C$_2$T$_x$ MXene nanosheets from spray dried 1 mg/ml crumpled Ti$_3$C$_2$T$_x$ dispersion. Reproduced with permission from Shah *et al.*[4]

To compare the aggregation resistant property of the crumpled MXene powder, the specific surface area of crumpled MXene was compared with freeze dried MXene powder. N$_2$ adsorption and desorption analysis (**Figure 4.12**) was used to measure the surface area of MXene powders using Brunauer–Emmett–Teller (BET) method. The specific surface area (SSA) for crumpled Ti$_3$C$_2$ powder was calculated to be 105.52 m^2/g which is marginally smaller than the 147.40 m^2/g SSA of freeze dried MXenes.
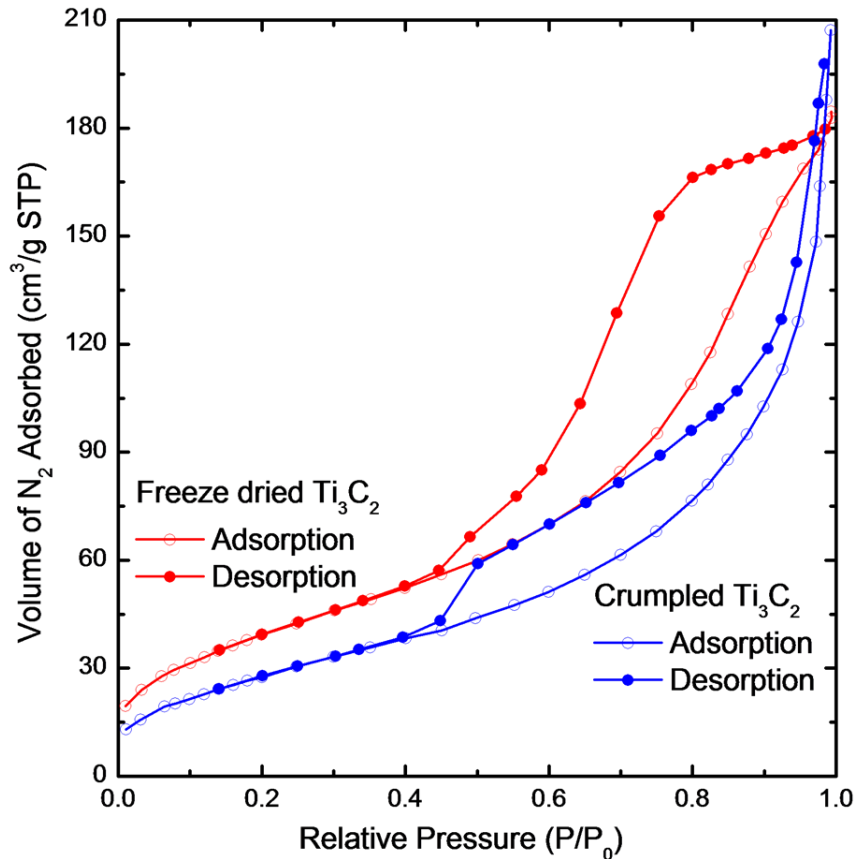
Figure 4.12 N_2 sorption and desorption measurements conducted using ASAP 2010 (Micrometrics) at 77.35 K. The samples were degassed at 373.15 K for 12 hours prior to the measurements. Reproduced with permission from Shah *et al.*[4]

4.4 Conclusion

In this study, we have successfully converted $Ti_3C_2T_x$ from 2D flat nanosheet to 3D crumpled structure via spray drying method, without the assistance of any templates. The extent of crumpling can be controlled by changing the feed concentration; higher concentration leads to decreased crumpling. The results also showed that crumpled nanosheet can be "uncrumpled" if rehydrated, indicating the change in structure is a reversible process.

CHAPTER 5

ARAMID NANOFIBER-REINFORCED 3D GRAPHENE HYDROGELS FOR

SUPERCAPACITOR ELECTRODES

5.1 Introduction

Graphene nanosheets can be assembled into a range of functional architectures.[125] These architectures are broadly divided into three categories: compact layered structures, semi-porous powder-based structures, and self-assembled 3D porous structures.[126] For example, buckypapers with a compact, layered architecture are made by vacuum filtration of aqueous graphene oxide (GO) dispersion. GO buckypapers have high tensile modulus, high tensile strength, and low strain-to-failure due to the large degree of π-π stacking and hydrogen bonding between adjacent graphene nanosheets which are aligned in-plane. Powder-based graphene film architectures can be obtained by directly pressing GO/reduced graphene oxide (rGO) powder or by solution casting them on a substrate. However, these architectures require binders to improve their mechanical integrity.[127] GO nanosheets may also be self-assembled into 3D porous architectures composed of randomly oriented nanosheets. These structures have higher surface area, porosity and strain-to-failure as compared to buckypapers and powder-based electrodes. However, 3D architectures tend to have poor mechanical integrity and electrical conductivity compared to rGO buckypapers.

GO hydrogels are one of the most widely studied types of 3D architectures. GO hydrogels are typically synthesized by self-assembly of aqueous GO dispersions using hydrothermal with or without further chemical reduction. During the self-assembly

process, GO nanosheets become hydrophobic and bind with surrounding nanosheets via π-π stacking to form a monolithic GO hydrogel. Several studies have catalogued how properties of GO hydrogels can be influenced by gelation parameters, such as pH of the pre-gelation dispersion, concentration and/or lateral size of GO nanosheets, reaction time and temperature, and concentration of ammonia, which acts as a chemical crosslinker.[128] In our prior paper, we examined how to tailor the morphology, density, and surface area of GO hydrogels by altering the concentration of ammonia and by crumpling the GO nanosheet morphology.[5] Other reports have also shown that gelation parameters can be used to modify the electrical conductivity, pore-size distribution, surface chemistry and mechanical properties of the GO gels.[128-130]

In general, GO hydrogels have high surface area, high porosity, an interconnected pore-network, and good electrical conductivity. Because of this combination of properties, GO hydrogels have been extensively used as binder-free electrodes for supercapacitor applications.[131,132] Reports have also shown that GO hydrogels can be compressed into thin and flexible supercapacitor devices to achieve high areal energy and power densities.[133,134] However, graphene gels have poor mechanical modulus (~100 kPa) in comparison to paper-like GO architectures (~4.8 GPa).[135] Several studies have reported the use of polymers and/or chemical crosslinking additives such as ethylene diamine,[136] polyvinyl alcohol,[137] polyacrylic acid,[138] or polypyrrole[139,140] to improve shear modulus, compressive modulus, and/or compression recovery.[141] These properties are important for designing deformation-tolerant and/or load-bearing supercapacitor devices.

One potential additive, not yet examined for rGO hydrogels, is aramid nanofibers (ANFs). ANFs are synthesized from Kevlar® threads, which are composed of aligned poly(paraphenylene terephtalamide) (PPTA) chains. Kevlar® threads are commercially widespread as high tensile strength and stiffness threads due to hydrogen bonding between aligned linear PPTA polymer chains. ANFs are synthesized from Kevlar® threads in a polar aprotic solvent (e.g. DMSO) in the presence of a strong base (e.g. KOH). The strong base deprotonates the amide groups on PPTA chains and reduces the interaction between PPTA chains. As a result, Kevlar® threads dissociate into a colloidal dispersion of nanofibers, which is stabilized by electrostatic repulsions between negatively charged amide groups on ANF surfaces.[142]

Several reports have used ANFs as filler in polymer matrices to enhance mechanical strength and stiffness.[143,144] Buckypapers made from ANF-graphene or ANF-CNTs have exhibited excellent tensile properties.[145,146] A branched variant of ANFs (BANFs) was shown to produce a high modulus hydrogel through hydrogen bonding between BANFs.[147] Recently, Kwon *et al.* reported synthesis of vacuum-filtered rGO-ANF buckypaper electrodes with excellent mechanical and electrochemical properties for supercapacitor applications.[148] This enhancement of properties was attributed to π-π stacking and hydrogen bonding interactions between layered rGO sheets and ANFs. However, ANFs have never been used in GO hydrogel-based supercapacitor electrodes.

We evaluated ANFs as a structural additive to improve the shear modulus of graphene hydrogels. Our results show that addition of only 2 wt.% of ANFs can improve the shear

modulus of the GO-ANF composite hydrogel by ~80%. This enhancement in shear modulus may make GO gels more suitable for use in applications involving load-bearing hydrogel electrodes. To this end, we evaluate the electrochemical properties of the proposed rGO-ANF composite as supercapacitor electrodes and discuss the trade-off in mechanical and electrochemical properties.

5.2 Materials and Methods

Materials

Graphite powder (SP-1) was obtained from Bay Carbon. Sulfuric acid (95-98%), $KMnO_4$, H_2O_2, HCl, DMSO, ammonium hydroxide and KOH were obtained from Sigma Aldrich. Kevlar® thread (grade K69) was purchased from The Thread Exchange.

Graphene oxide synthesis (modified Hummers method)

Graphene oxide was synthesized using modified Hummers method. 5 gm graphite powder and 230 mL of concentrated H_2SO_4 were mixed in a 1L Erlenmeyer flask in an ice bath at ~5 ℃. 15 g of $KMnO_4$ was slowly added to the acid solution, keeping the temperature between 5 and 10 ℃. The mixture was stirred for 2 h at room temperature. The reaction flask was returned to the ice bath and the reaction was quenched by slowly adding 450 mL deionized (DI) water, keeping the mixture around 45 ℃. The reaction mixture was stirred for 2 h at room temperature, transferred to a 2L Erlenmeyer flask, and then filled with DI water to ~1600 mL. 23 mL of 33% H_2O_2 was slowly added to the mixture to cause manganates to re-enter solution, followed by allowing the mixture to stir for 72 h. The stirring was stopped, and GO product was

allowed to settle. 1L of the acid solution was decanted and replaced with 1L of 10% HCl and allowed to stir for 24 h and settle again. This step was repeated three times. The resulting reaction mixture was washed with DI water until the pH reached ~4.5 to obtain aqueous graphite oxide suspension.

Graphene oxide processing for gelation

Washed graphite oxide suspension was exfoliated to GO sheets by bath sonicating at 55 °C overnight. The sonicated aqueous GO dispersion was centrifuged at 2000 rpm for 20 min to remove the heavy unexfoliated fraction. The stable GO supernatant was collected for further processing. A GO dispersion in DMSO was obtained using solvent exchange. 200 mL of DMSO was added to 200 mL of aqueous GO dispersion (10 mg/ml), followed by 30 minutes of bath sonication at room temperature. The mixture was subjected to rotary evaporation to selectively remove water and obtain GO-DMSO dispersion of 10 mg/ml in concentration.

Aramid nanofiber (ANF) synthesis

To prepare ANFs, bulk Kevlar® (K69) thread and KOH pellets were added in DMSO at concentrations of 2 mg/ml and 3 mg/ml, respectively. The mixture was stirred for about 10 d until the solution appeared dark red. The residual KOH pellets were allowed to settle and the colloidal 2 mg/ml ANF dispersion was decanted for further use.

Combining ANFs and GO sheets

To obtain a homogeneous GO and ANF dispersion in DMSO, a desired concentration of ANF/DMSO dispersion (0.2 mg/ml) was added into GO/DMSO dispersion (10 mg/ml) during bath sonication, followed by vortex mixing. To induce

hydrogen bonding between GO nanosheets and ANFs, DI water was added to the GO-ANF/DMSO mixture, followed by ~2 h of magnetic stirring at room temperature.

Synthesis of GO-ANF hydrogels

The GO-ANF mixture in DMSO/water was solvent exchanged to water using dialysis. As-obtained aqueous GO-ANF mixture was concentrated in a rotary evaporator to yield a GO-ANF slurry with a GO loading of 10 mg/ml. For sol-gel reaction, the aqueous GO-ANF slurry was mixed with ammonium hydroxide (NH_4OH), with a NH_4OH/GO ratio (v/w) of 0.024 mL/mg. GO(ANF_X) hydrogels with desired ANF concentration (X wt. % dry solid basis) were obtained by heating the aqueous GO-ANF-NH_4OH mixture at 90 ℃ in a sealed hydrothermal chamber for 3 d. Excess ammonia and reaction byproducts were removed by washing with DI water. rGO(ANF_X) hydrogels were obtained by treating GO(ANF_X) hydrogels in 40 mg/ml aqueous L-sodium ascorbate solution at 90 ℃ for 5 h. The residual L-sodium ascorbate and reaction byproducts were removed by washing with DI water.

Scanning electron microscopy

The cross-sectional morphologies of aerogels were investigated using scanning electron microscopy (SEM). The GO(ANF_X) hydrogels were flash-frozen in liquid nitrogen and then fractured to expose their interior cross section. The fractured hydrogels were freeze-dried for 3 d in a Labconco FreeZone dryer to obtain aerogels. SEM analysis was performed using a JEOL JSM-7500F instrument at an acceleration voltage of 2 kV.

Rheology

For oscillatory strain and frequency sweeps, GO hydrogel monoliths were sliced to disks of thickness of 2 mm. An Anton Parr Physica MCR301 rheometer was used with a parallel plate fixture at room temperature for the analysis. The plate gap was determined using a normal force control of 1 N. Oscillatory amplitude sweeps were conducted at a nominal frequency of 1 Hz to find the linear viscoelastic region. Oscillatory frequency sweeps were performed at an amplitude of 0.5 – 1.0 %. For compression analysis, 2 mm hydrogel disks were compressed using a hydraulic press to predetermined heights using shims.

Methylene blue (MB) dye adsorption tests

MB dye tests were performed to measure the specific surface area of $rGO(ANF_X)$ hydrogels. Hydrogels were immersed in a known concentration of aqueous MB solution for two days. The concentration of MB dye was measured using UV-Vis absorption spectroscopy. Surface area of graphene hydrogel was calculated from mass adsorbed MB dye using the literature correlation of 2.54 mg MB associating with 1 m^2 of graphene surface.[149-151]

Atomic Force Microscopy (AFM)

GO and ANF dispersions were separately drop-cast on freshly cleaved Mica substrate at a concentration of 0.02 mg/ml/. Height profiles were obtained in tapping mode (Bruker dimension icon AFM).

Electrochemical characterization

rGO(ANF$_X$) hydrogels were sliced into ~2 mm thick disks using a blade, followed by hydraulic pressing to obtain thin hydrogel electrodes. A pressure of 500 psi was applied for 1 min using a cold press with a 670 µm shim thickness between non-stick aluminum foils. Two electrodes of 3/8" diameter were punched from the pressed film, followed by assembly in a symmetric cell for supercapacitor testing. 6M KOH was the aqueous electrolyte, and the separator was hydrophilic polypropylene (Celgard 3501). Platinum foils were used as current collectors and electrical contact were made of stainless steel. Gamry reference 3000 Potentiostat was used to conduct all electrochemical tests at room temperature.

Cyclic voltammograms (CV) were collected in the voltage window of 0-1 V at various scan rates. The specific capacitance was calculated from CV curves by using the formula $C = 2 \int_{V_{min}}^{V_{max}} IdV/(v \times \Delta V \times m)$, where C is the specific capacitance in F/g, V_{min} and V_{max} are the low and high voltage cutoffs (Volts) respectively, I represents the current, ΔV is the potential window, v indicates the scan rate, and m represents the total mass of both electrodes. Electrochemical impedance spectroscopy was performed using an AC voltage of 10 mV, and a frequency range from 100 kHz to 1 mHz.

5.3 Results, discussion and proposed future work

GO-ANF dispersion processing and hydrogel assembly

Synthesis of graphene oxide (GO) hydrogels using hydrothermal gelation involves an aqueous GO colloid with dissolved ammonia. However, ANFs require a polar aprotic solvent to form a stable dispersion and are typically prepared in a solution

73

of DMSO and KOH. When an ANF/DMSO/KOH dispersion is added directly to an aqueous GO dispersion, the ANFs will be reprotonated by water and coagulate with each other instead of becoming well-mixed with the GO nanosheets. In order to avoid this problem of coagulation of ANFs, aqueous GO dispersion is first solvent-exchanged to DMSO using rotary evaporation. An ANF/DMSO/KOH dispersion can then be slowly added to the GO/DMSO while mixing to prevent ANF coagulation during the transition. Water is then reintroduced to the combined dispersion to induce hydrogen bonding between reprotonated ANFs and GO nanosheets. DMSO is slowly removed using dialysis to yield an aqueous dispersion. The schematic of this procedure is shown in **Figure 5.1a**. ANF loadings of 0, 1, 2, 5, 10, and 15 wt.% (on a dry weight basis) were incorporated into the precursor GO dispersion.

Figure 5.1 (a) ANF dispersion in DMSO is added to GO dispersion in DMSO. GO-ANF dispersion in DMSO is dialyzed with water to obtain an aqueous GO-ANF dispersion. (b) AFM height profile of aqueous GO-ANF 2 wt.% loading (dry weight basis) dispersion (drop-cast on mica substrate) (c) Sol-gel gelation results in formation of a GO(ANF$_x$) hydrogel.
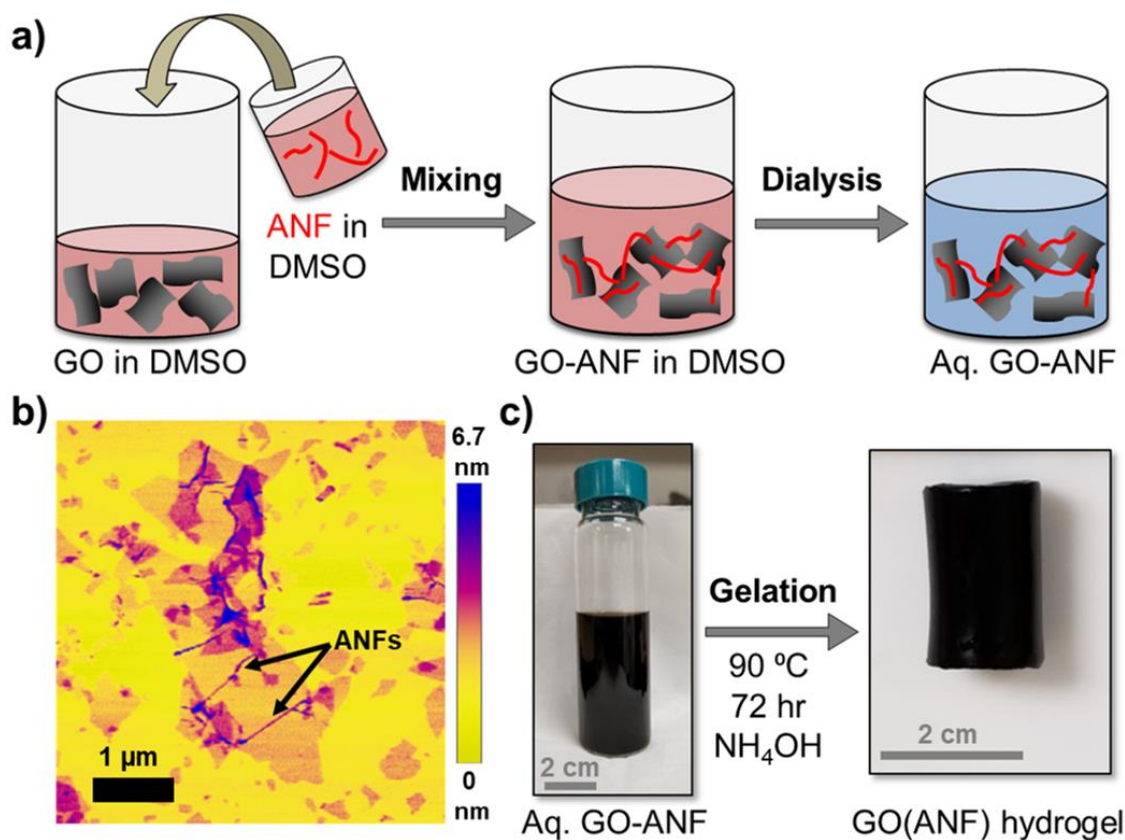
Atomic force microscopy (AFM) was performed on the pre-gelation dispersion to observe the morphology and interactions of GO and ANFs. In the AFM height profile in **Figure 5.1b**, few-layered GO nanosheets are distributed across a mica substrate with many appearing to have ANFs adhered to their surface. In several areas, ANFs even appear to extend between nanosheets to form links which would be desirable in the intended gel structures. Furthermore, based on comparison with AFM of an ANF/DMSO/KOH dispersion (**Figure 5.2**), no significant aggregation of ANFs is

75

visible. **Figure 5.1b** serves to demonstrate the compatible interaction of GO and ANFs and their successful nanoscale incorporation through the procedure previously described.
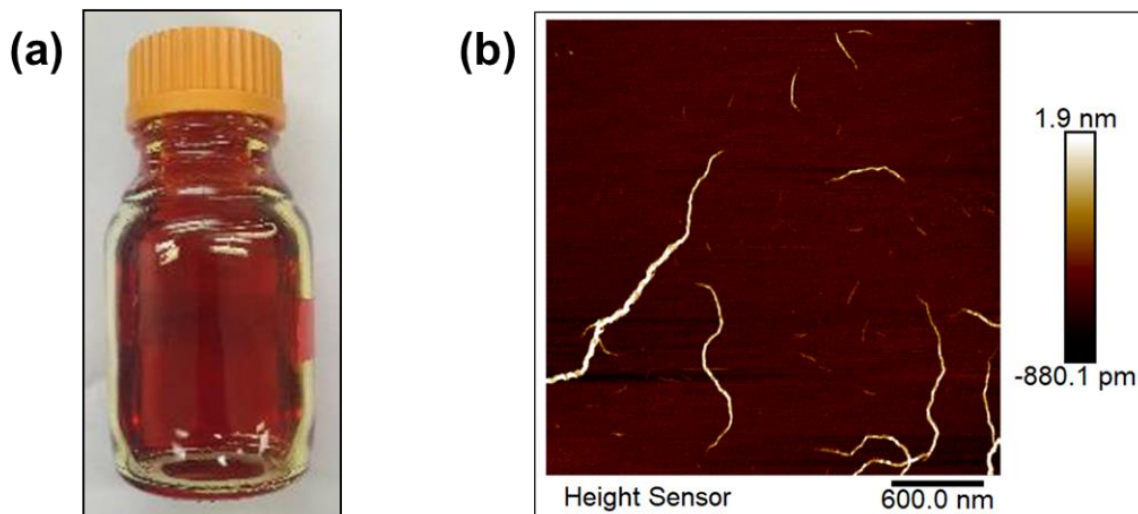
Figure 5.2 (a) Aramid nanofiber dispersion in DMSO and KOH (2 mg/ml). (b) Atomic force microscopy image of ANF dispersion drop-cast on mica substrate.

The aqueous GO-ANF dispersion undergoes self-assembly upon being heated at 90 °C for 3 days in the presence of ammonium hydroxide to obtain GO-ANF hydrogels (**Figure 5.1c**). The resulting gels are referred to as $GO(ANF_X)$, where X represents the ANF loading on a dry weight basis. These GO-ANF gels were analyzed to study the effect of ANFs on the hydrogel's mechanical properties and electrochemical performance.

Scanning Electron Microscopy of $GO(ANF_X)$ aerogels

The morphology and pore-structure of $GO(ANF_X)$ hydrogels were analyzed using scanning electron microscopy (SEM). As-prepared hydrogels were flash frozen, freeze-fractured, and then freeze-dried for SEM analysis (**Figure 5.3**). A common observation in all samples is that a porous 3D morphology is retained in all $GO(ANF_X)$

compositions with pore sizes ranging from sub-microns to several microns. This shows that the gelation of GO nanosheets in presence of ANFs was successful. ANFs themselves are difficult to observe using SEM due to their small size.
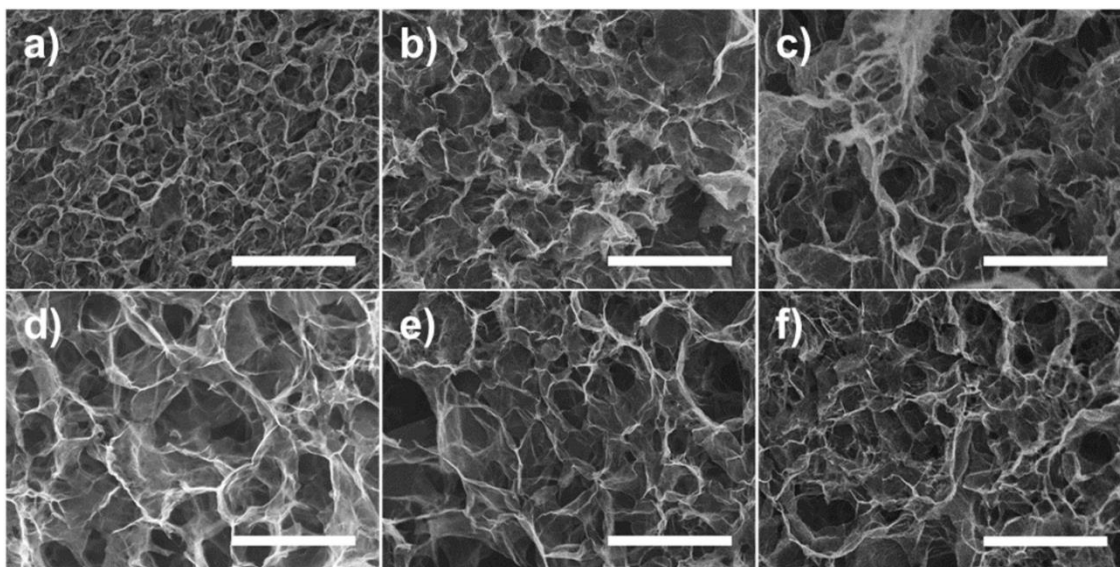
Figure 5.3 Scanning electron microscopy (SEM) images of graphene oxide and aramid nanofiber (ANF) composites at (a) 0 dry wt.% ANF, (b) 1 dry wt.% ANF, (c) 2 dry wt.% ANF, (d) 5 dry wt.% ANF, (e) 10 dry wt.% ANF, and (f) 15 dry wt.% ANF. The scale bars in all SEM images are 2 μm.

Rheology of GO(ANF$_X$) hydrogels

The mechanical performance of GO-ANF composite hydrogels was investigated by comparing shear rheological properties as a function of ANF content (**Figure 5.4**). **Figure 5.4a** illustrates that storage (G') and loss modulus (G") of GO(ANF$_2$) hydrogels are independent of shear rate, with G' about an order of magnitude higher than G" over the entire frequency range (1 – 200 rad/s). This result indicates that self-assembled hydrogels have permanent crosslinks and are predominantly elastic in nature.[152] Shear storage-modulus (G') was measured as a function of oscillatory strain as shown for the

neat GO hydrogel in **Figure 5.4b**. These oscillatory shear-strain sweeps were performed on hydrogel slices to determine the linear viscoelastic strain regime. A comparison of G' for all ANF loadings, measured at 0.02% strain and 1 rad/s frequency, (**Figure 5.4c**), revealed that G' was highest for the GO(ANF$_2$) sample and was about 80 % higher than G' for the neat GO sample. However, G' begins to deteriorate when ANF loading increases to 5 wt.% and higher. This decline in G' may be caused by ANFs disrupting or decreasing the number of effective crosslinks during the gelation of GO nanosheets. Several studies have utilized shear rheology on graphene hydrogels, and their G' values are comparable to our hydrogels at similar solids content.[153,154]
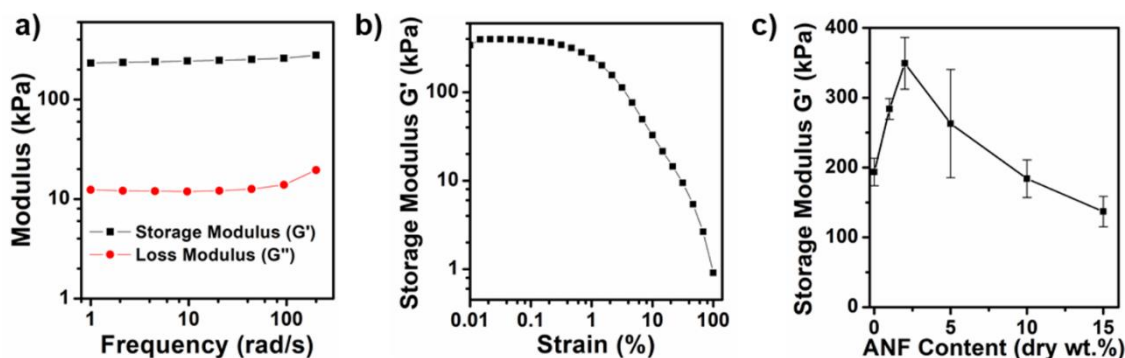
Figure 5.4 (a) Oscillatory frequency sweep of neat GO hydrogel at an amplitude of 0.5 %. Storage (G') and loss modulus (G") are nearly constant with frequency, indicating a crosslinked elastic hydrogel (b) G' variation of GO(ANF$_2$) hydrogel with strain rate (c) Variation of G' (measured at 0.02 % strain and 1 rad/s) with ANF loading. GO(ANF$_2$) hydrogel shows 80% increase in storage modulus as compared to neat GO hydrogel.

The effect of uniaxial-compression on the shear storage modulus of the neat rGO and rGO(ANF$_2$) composite hydrogels was investigated. Compression can influence the microstructure and crosslinks of the rGO architecture. Cross sections of compressed neat rGO and rGO(ANF$_2$) hydrogels show partial alignment of nanosheets in the direction

perpendicular to the compression axis (**Figure 5.5**). Chemically reduced hydrogel slices were tested using shear oscillatory frequency sweeps at various degrees of compression. The values of storage modulus (G') were measured at a frequency of 10 rad/s over an amplitude range of 0.1 - 0.5% and compared (**Figure 5.6**).
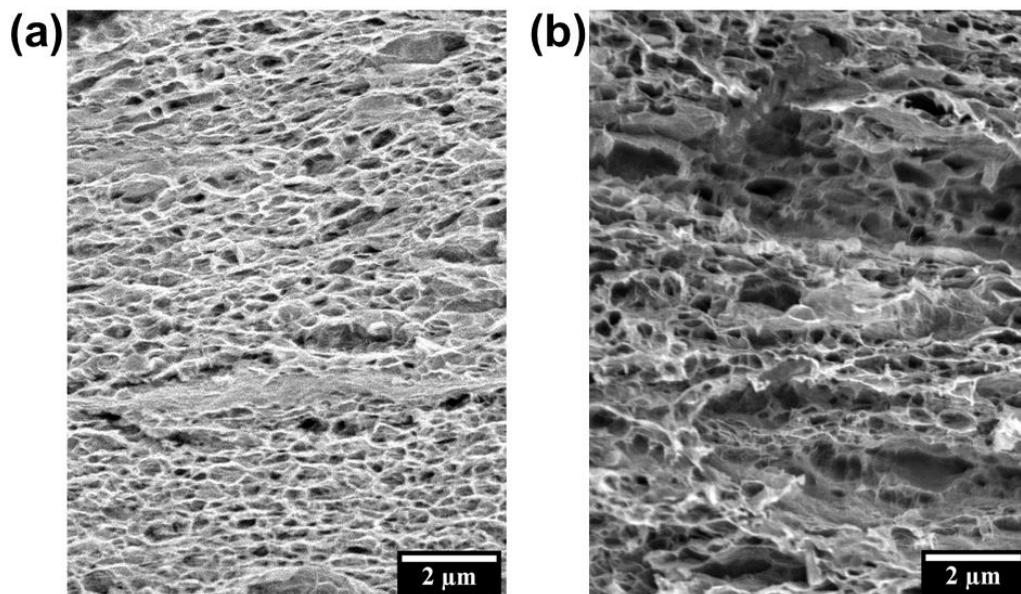
Figure 5.5 Cross sectional SEM images of compressed (a) rGO and (b) rGO(ANF$_2$) composites. As-prepared hydrogels were compressed to 30% of their original thickness (2 mm) prior to analysis.

For the neat rGO hydrogel, we observe an increase in shear modulus with compressive strain of ~46%, followed by a reduction in shear storage modulus at ~75%, indicating damage to the internal crosslinks beyond a certain strain. However, the rGO(ANF$_2$) hydrogel shows a consistent increase in G' (up to ~256%) for compressive strain as high as ~87%. The damage to internal crosslinks in GO(ANF$_2$) hydrogel may be prevented at high strains due to the presence of additional adhesive strength imparted

by the ANFs. The data provide important insight into the dependence of storage modulus on addition of ANFs, nanosheet alignment, and densification of hydrogel microstructure.
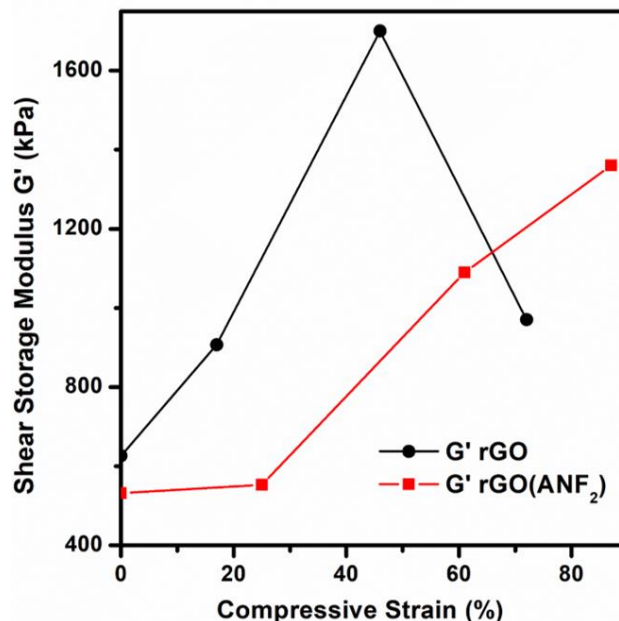
Figure 5.6 Storage modulus (G') of rGO and rGO(ANF₂) hydrogels with increasing axial-compression strain.

Electrochemical characterization of rGO(ANF_X) hydrogels

The supercapacitor performance of the hydrogel composite was measured in a symmetric cell with 6 M aqueous KOH as an electrolyte. Hydrogel electrodes were prepared by slicing and pressing the as-prepared GO(ANF_X) hydrogels into films. These hydrogel films were further chemically reduced using L-sodium ascorbate to improve their electrical conductivity prior to their assembly in test cells.[155,156] Cyclic voltammograms (CVs) for rGO(ANF_X) samples at the scan rates of 20 mV/s (**Figure 5.7a**) show nearly rectangular CVs, indicating an electrical double-layer mechanism of

energy storage and low electrolyte ion transport resistance through the hydrogel electrodes.
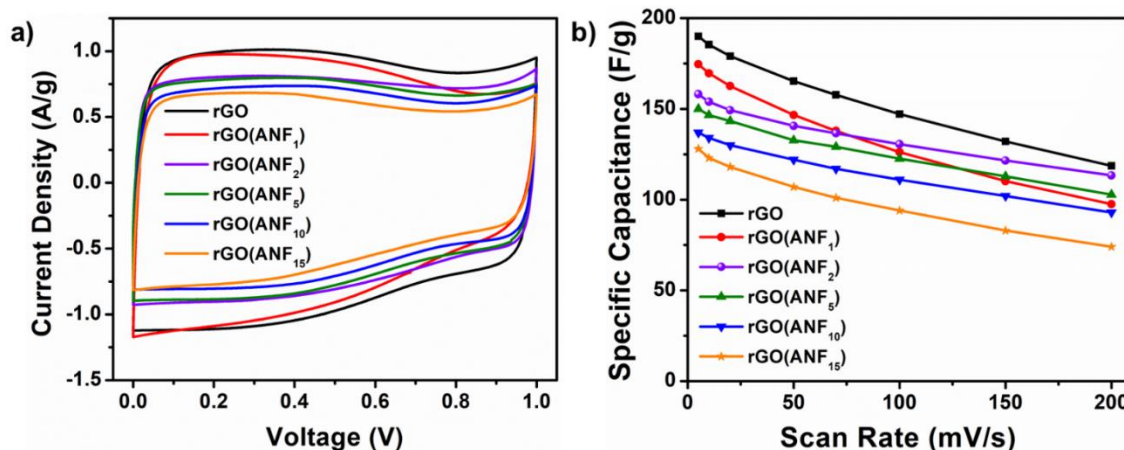
Figure 5.7 Electrochemical performance of rGO(ANF) hydrogels. (a) Cyclic voltammetry scans for rGO(ANF) samples at a scan rate of 20 mV/s. (b) Specific capacitance's dependence on scan rate (5 – 200 mV/s) for rGO(ANF) hydrogels with varying ANF content. Total electrode mass (rGO and ANFs) was included in calculating the current density and specific capacitance.

The specific capacitance values of rGO(ANF$_X$) hydrogels are compared in **Figure 5.7b**. Neat rGO electrodes with a thickness of ~600 µm showed excellent specific capacitance of 190 F/g at scan rate of 5 mV/s. Typical supercapacitor electrodes are limited to a thickness ~10-20 µm to minimize ion-diffusion resistance and achieve high specific capacitance. However, rGO(ANF$_X$) hydrogel electrodes' interconnected pore structure allows to have very low ion-diffusion resistance even at large thickness. A general trend of decrease in specific capacitance of composite hydrogels is observed with increasing ANF content at a given scan rate. This was expected because ANFs are electrochemically inactive, and as ANF composition increases, the fraction of active sites decreases. Furthermore, ANFs may reduce the π-π interactions between rGO sheets

as well as reduce accessible surface area on rGO nanosheets (**Figure 5.1b**). The specific

surface area of neat rGO hydrogel was measured to be 199.3 m^2/g based on an MB dye

adsorption test. The rate performance of hydrogel composites was evaluated by

measuring the effect of increase in scan rate on specific capacitance. The specific

capacitance is expected to decrease at higher scan rates due to ion-diffusion limitations.

As a result, it is expected that architectures with more porous microstructure and better

ion-diffusion properties will show lower extent of capacitance reduction. The specific

capacitance of neat rGO hydrogel was 119 F/g at scan rate of 200 mV/s, which is 63% of

its specific capacitance of 190 F/g at 5 mV/s. For rGO(ANF$_2$) hydrogel, 72% of the

specific capacitance was retained at 200 mV/s compared to that at 5 mV/s, indicating

improved rate capability compared to neat rGO electrodes. Electrochemical impedance

spectroscopy (**Figure 5.8**) shows very small electrical and ion diffusion resistance for all

rGO(ANF$_X$) composites.
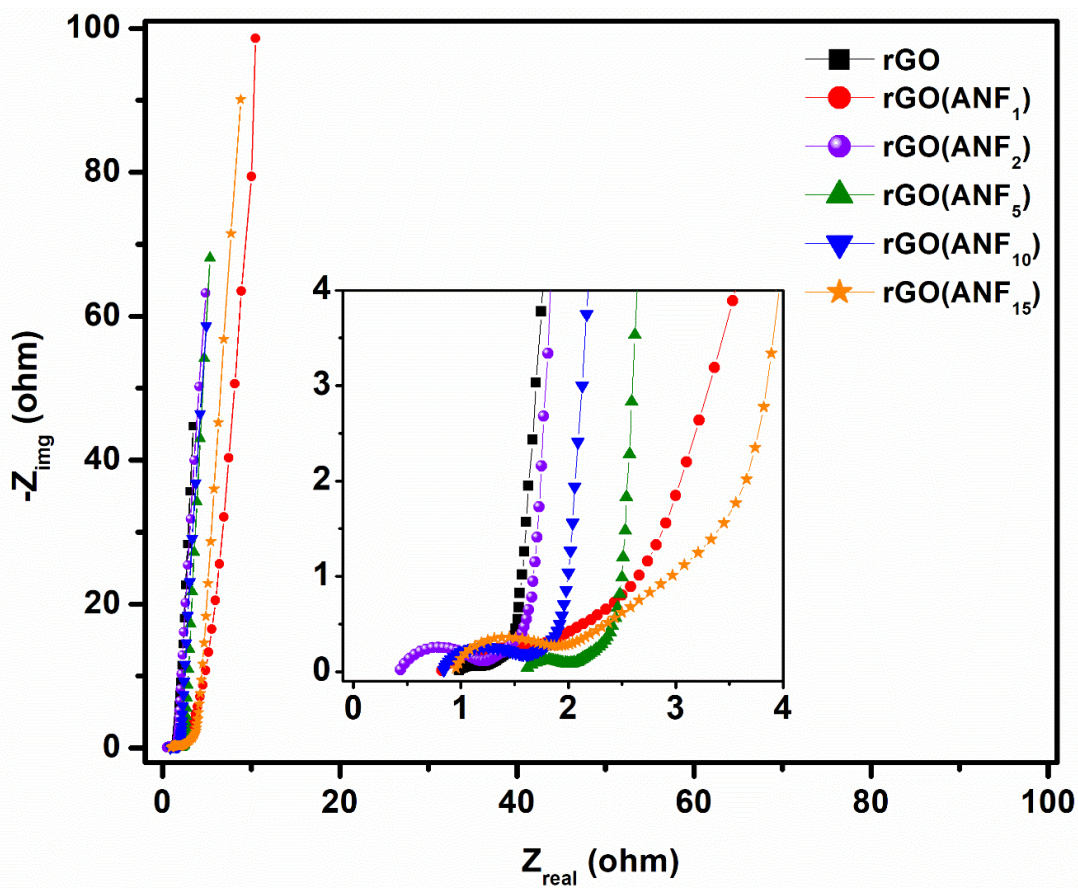
Figure 5.8 Electrochemical impedance spectra of rGO(ANFx) hydrogels with ANF composition (X) varying from 0 – 15 wt.% (dry basis)

5.4 Conclusion

In this study, we fabricated high shear-modulus ANF reinforced GO hydrogel electrodes by harnessing strong hydrogen bonding and π-π stacking interactions between GO nanosheets and ANFs. Synergistic interactions between GO and ANFs manifested as 80% improvement in shear modulus of GO-ANF 2 wt.% composite (349 kPa) over neat-GO hydrogel (193 kPa). We also demonstrated that compression of hydrogels results in an increase of the shear storage modulus by 46% due to partial alignment of the constitutive nanosheets. The specific capacitance of neat-rGO hydrogel was 185 F/g at

83

scan rate of 10 mV/s. This study paves the way for further research to design rGO hydrogel electrodes reinforced with structural fillers to develop load-bearing multifunctional energy storage devices.

CHAPTER 6

CONCLUSIONS AND FUTURE WORK

6.1 Conclusions and summary

In Chapter 2 of this dissertation, we devised an approach to improve the yield of graphene exfoliation by modifying the centrifugation process.[157] The separation of exfoliated graphene from graphitic precursor is a challenge that complicates the scalability of various production routes and increases the associated time and energy cost. We found that ~50% of well exfoliated pristine graphene nanosheets are trapped in the sediments during the centrifugation process. A method was developed to extract these inaccessible graphene nanosheets by repeatedly adding solvent to the sediment, followed by mixing and re-centrifugation. We obtained higher graphene yield with larger quantities of solvent, but this higher graphene yield comes at the price of extra solvent processing and overhead costs on an industrial scale. The marginal increase in graphene yield reduces with increasing wash volume. An optimization algorithm was also created to determine the optimum volume of solvent for graphene recovery, given the costs of solvent processing, precursor material, and graphene product.

Moving forward, we want to extend this approach to other types of nanosheets/dispersant systems including electrochemically exfoliated graphene dispersed in water/ethanol cosolvent system, and aqueous pristine graphene dispersions with graphene quantum dots as dispersants. Another important aspect to consider is to evaluate the effect of dispersant type on the fractional yield of trapped nanosheets that can be extracted with each wash cycle.

In chapter 3, we concluded that the sulfonyl (-SO$_3$H) functionalized graphene quantum dots can disperse significantly higher concentration of pristine graphene in water compared to those functionalized with carboxylic (-COOH), and amine (-NH$_3$) groups. Moreover, the aqueous graphene dispersion with sulfonyl functionalized graphene quantum dots resulted in highest zeta potential of -64 mV, indicating excellent colloidal stability. Similar trends were observed in prior studies for pyrene derivative based dispersants, indicating that sulfonyl (strong electron withdrawing) group's role is universal over range of polyaromatic hydrocarbon sizes in creating efficient graphene dispersants.

In addition, the as-prepared aqueous graphene dispersions were utilized to improve the contrast of polystyrene photonic crystals as graphene nanosheets can suppress the incoherent diffused scattering.[3] In the future, we are interested in understanding the influence of GQD's size on exfoliating and dispersing graphene nanosheets.

As discussed in Chapter 4, a spray drying approach was successfully employed to crumple and scroll Ti$_3$C$_2$T$_X$ MXene nanosheets. The capillary forces in a spray dryer's drying water droplets were utilized to induce crumpling in 2D nanosheets to obtain 3D crumpled structures. BET surface area analysis showed that the crumpled particles had a high specific surface area of 105 m^2/g, indicating the aggregation resistant property of the powders, unlike the parent 2D nanosheets.

In the future, our goal is to utilize the crumpled MXene powder in batteries and supercapacitors to achieve high active surface area and better ion diffusivity. A trade off

for the spray drying method is partial oxidation of MXene nanosheets due to high processing temperature of 220 ℃. Moving ahead, we want to devise new approaches to prevent oxidation during the spray drying process by introducing a reducing agent in the nanosheet dispersion.

In chapter 5, we fabricated 3D porous rGO hydrogels using colloidal self-assembly for application in supercapacitors. Addition of ANFs as a structural filler results in significant improvement of the hydrogel's shear modulus. However, we found that higher than 2 wt.% (dry weight basis) concentration of ANFs result in decrease in shear modulus properties as they likely start interfering with the crosslinking between the GO nanosheets during the gelation process.

This study shows that high-strength nanofibers can provide reinforcement to nanosheet hydrogels provided that the nanofibers do not interfere with the crosslinking process. Moreover, the solvent-exchange approach utilized for mixing GO and ANF can also be extended to other nanosheet dispersions, such as MXenes, to create homogeneous ANF nanomaterial dispersions. However, water incompatibility of ANF/DMSO/KOH dispersions still remains to be addressed in the ANF composite community.

6.2 Future work

Electrically conductive and flexible ANF-MXene buckypapers

Introduction

Ti$_3$C$_2$T$_X$ MXene nanosheets have the unique combination of high electrical conductivity and hydrophilicity due to their extensive surface terminal groups (-O, -OH, -F). We utilize these properties to create strong and durable composites of MXene and ANFs. MXene nanosheets will provide electrical conductivity as well as improvement in ultimate strain due to the extensive hydrogen bonding between the surface terminal groups on MXene with the carbonyl and amine groups on the ANF surface. These high strain conductive films can be used in applications such as structural electronics, wearable electronics, and electromagnetic interference (EMI) shielding.

Materials and methods

Ti$_3$C$_2$T$_X$ MXene nanosheets were synthesized using the LiF+HCl method described in Chapter 4. ANF dispersion was made from commercial K69 thread using method described in Chapter 5. MXene nanosheet dispersion were combined with aqueous sodium ascorbate (NaAsc) solution to impede oxidation during processing which involved a strong base KOH which can expedite the oxidation of MXenes. The aqueous MXene-NaAsc solution was solvent exchanged to DMSO using rotary evaporator to obtain a MXene/NaAsc/DMSO dispersion. The as-prepared ANF dispersion was diluted to 0.2 mg/ml and added drop wise to MXene/ NaAsc/DMSO dispersion while stirring. 1 ml of water was added to the MXene/ NaAsc/ANF/DMSO

mixture per mg of ANF to induce protonation and crosslinking of ANFs. This solution is vacuum filtered on a 200 nm pore size nylon membrane to obtain layered MXene-ANF films. After allowing the buckypaper to dry in a vacuum oven overnight at room temperature, the buckypaper was peeled from the Nylon membrane to obtain a free-standing film for further characterization.

A TA instruments DMA was used to measure the tensile properties of MXene-only and MXene-ANF (10% ANF loading). For the DMA tensile testing the buckypaper was cut in to rectangular strips of 2-3 mm in width and about 15-20 mm in length. The buckypaper was gripped in tensile testing apparatus with about 10 mm gap between the clamps. A constant strain rate of 0.1% was applied and the stress was measured. SEM was performed on the fracture cross-section.

Preliminary results:

The as-prepared MXene-ANF (10 wt.%) buckypaper and MXene-only buckypapers cut in to rectangular strips are shown in **Figure 6.1**.
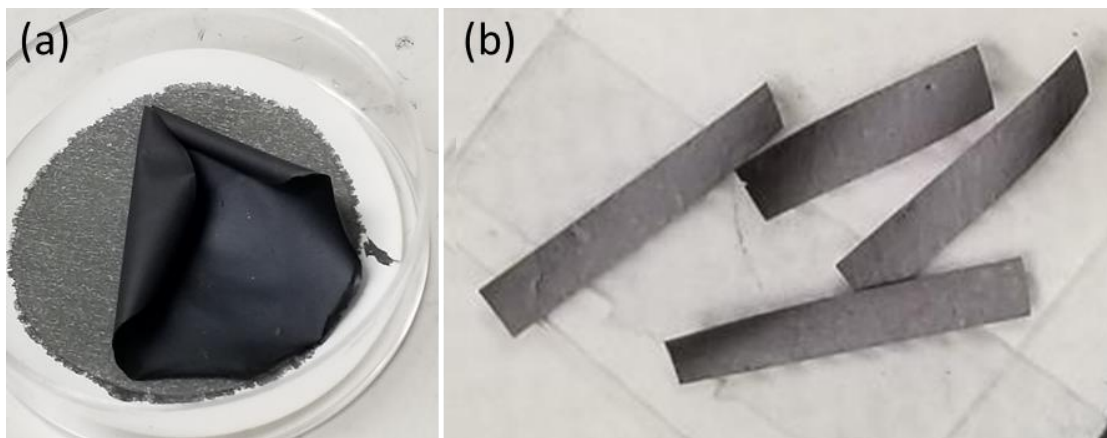
Figure 6.1 (a) Formation of a flexible and free standing MXene-ANF (10 wt.%) film after vacuum filtration on a nylon membrane. (b) MXene-only buckypaper cut in to rectangular strips before tensile testing

The SEM images of MXene-only buckypaper cross-section are shown in **Figure 6.2** indicating a compact layered structure with some degree of waviness. The cross-section of MXene-ANF (10 wt.%) buckypaper in **Figure 6.3** indicates presence of waviness as well as small spheres which are typical of partially oxidized MXenes. The future work will involve increasing the amount of sodium ascorbate to prevent oxidation during processing.
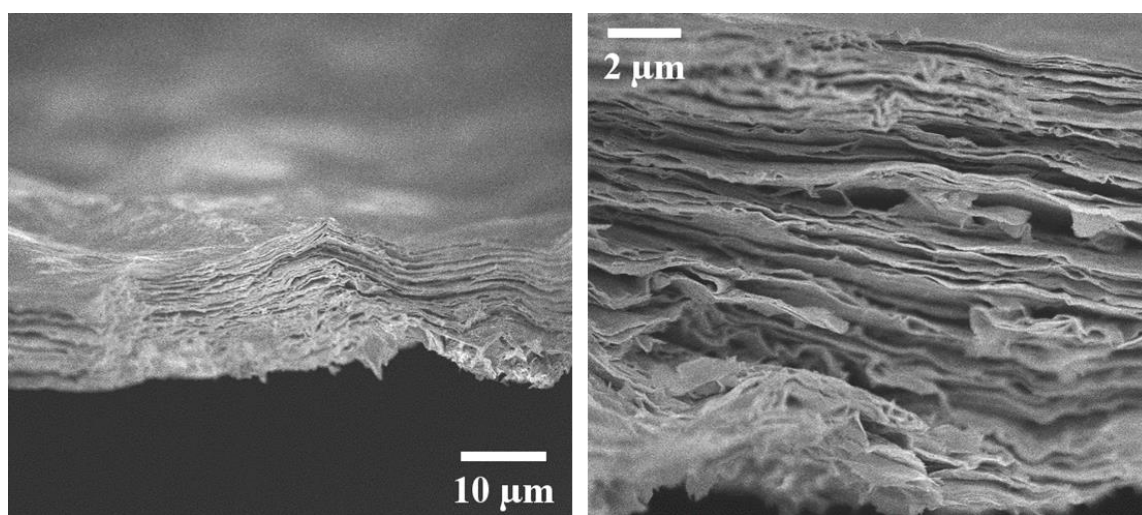
Figure 6.2 Low (left) and high (right) magnification SEM images of MXene-only buckypaper cross-section
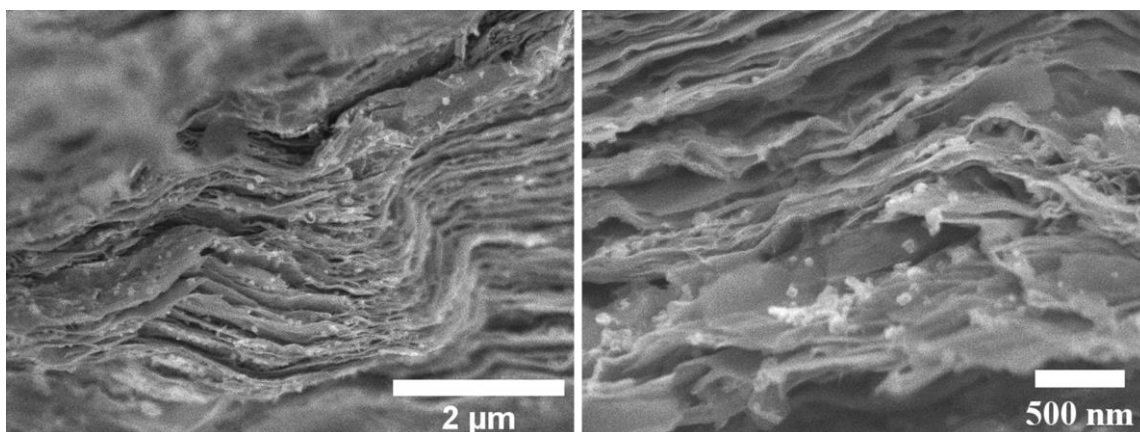
Figure 6.3 Low (left) and high (right) magnification SEM images of MXene-ANF (10 wt.%) buckypaper cross-section

The stress-strain curves are analyzed to measure the ultimate strain, toughness, Young modulus, and ultimate strength. These properties are compared against the mechanical properties reported in the literature. The MXene-ANF properties are compared with rGO-ANF (0.1% strain rate),[135] MXene-PVA (polyvinyl alcohol),[97] and ANF-only (1% strain rate)[148] samples with similar loading of fillers and active materials. The results are compiled in the **Figures 6.4, 6.5, 6.6, and 6.7**.

The data shows that MXene-ANF composites have significant improvement in ultimate strain property (**Figure 6.4**) compared to other nanocomposites. This can be attributed to large number of surface functional groups on MXene surface which can hydrogen bond with amide and carboxylic groups on ANFs. Such high improvement in yield strain also translates to significant enhancement in the toughness of nanocomposites (**Figure 6.5**). However, the improvement in Young modulus and ultimate strain is not as significant in case of rGO-ANF composites (**Figures 6.6, 6.7**).

This may be attributed to the π- π stacking interactions between rGO and ANF which is absent in case of MXenes-ANF.
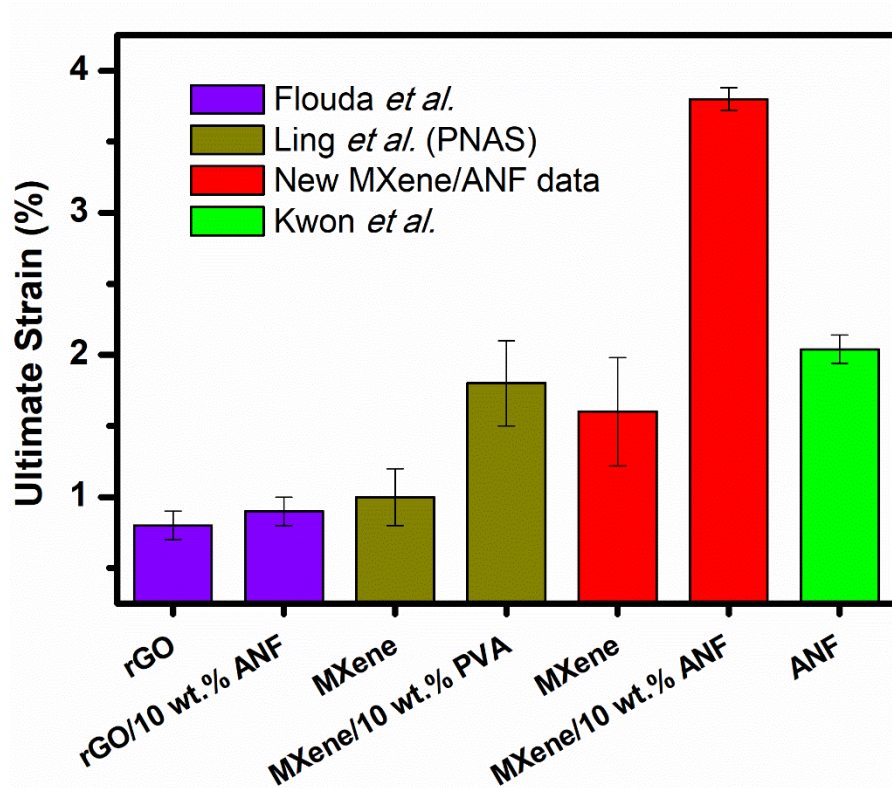
Figure 6.4 Comparison of MXene-ANF composite ultimate strain (%) property with nanocomposite literature
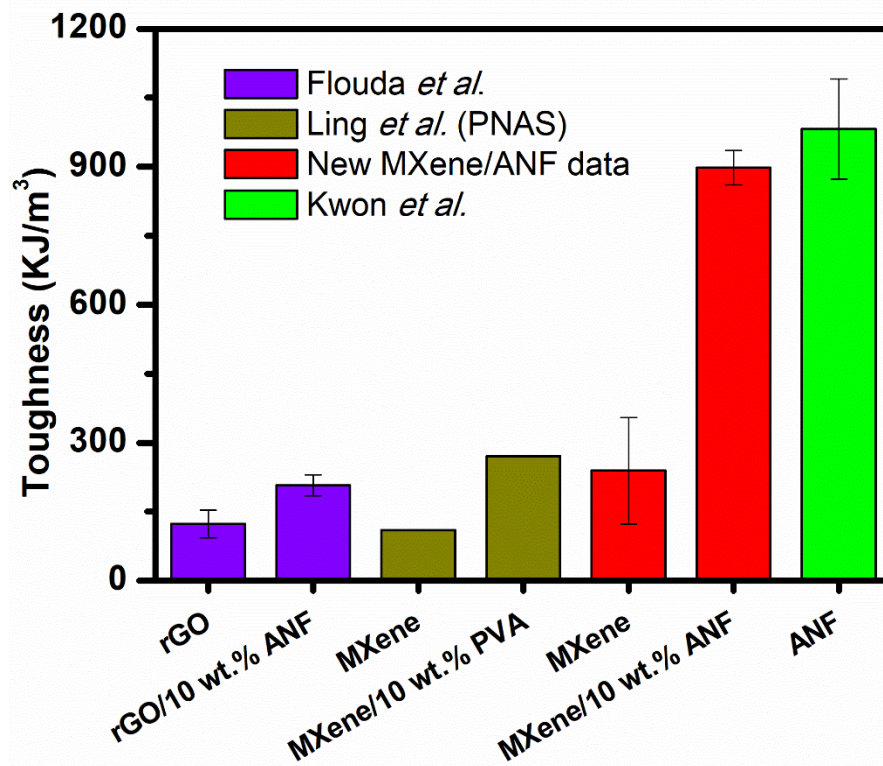
Figure 6.5 Comparison of MXene-ANF composite toughness (kJ/m^3) property with nanocomposite literature
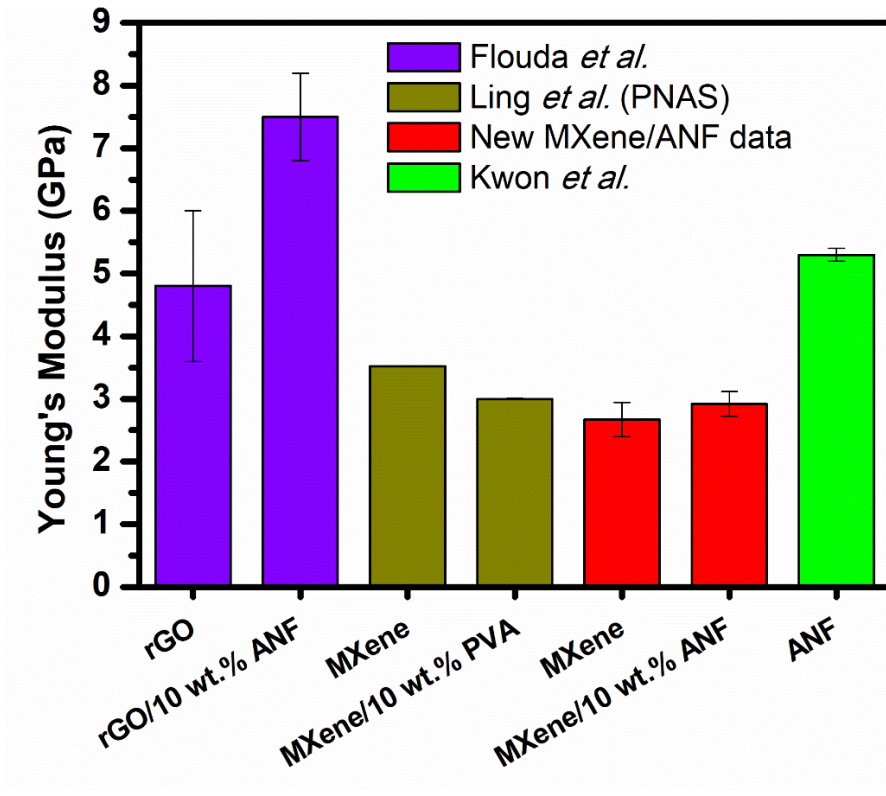
Figure 6.6 Comparison of MXene-ANF composite Young's modulus (GPa) property with nanocomposite literature
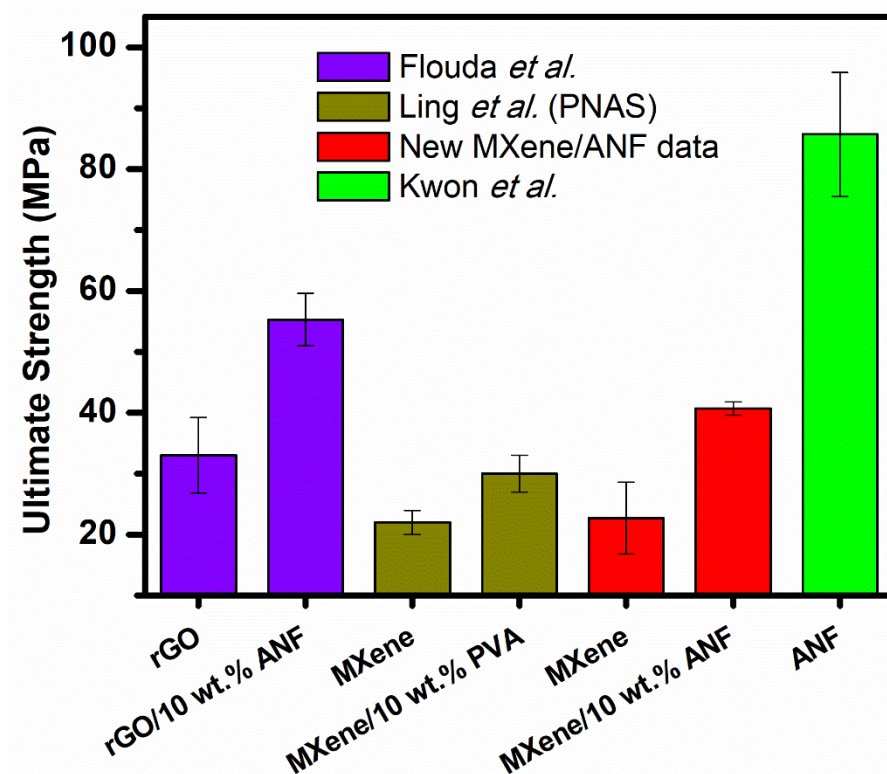
Figure 6.7 Comparison of MXene-ANF composite ultimate strength (MPa) property with nanocomposite literature

Proposed future work

In the future, we want to characterize and the relative fraction of functional groups between rGO and MXenes using XPS. XPS will also help in determining the he extent of hydrogen bonding interactions between the constituents of the nanocomposites. Further ahead, we want to fabricate nanocomposites with low concentrations of MXenes in ANF mats and estimate the composition of MXenes required for achieving electrical percolation threshold in ANFs.

REFERENCES

(1)   Parviz, D.; Irin, F.; Shah, S. A.; Das, S.; Sweeney, C. B.; Green, M. J. Challenges in Liquid-Phase Exfoliation, Processing, and Assembly of Pristine Graphene. *Advanced Materials* **2016**, *28*, 8796-8818.

(2)   Rountree, K. S.; Shah, S. A.; Sweeney, C. B.; Irin, F.; Green, M. J. Graphene reflux: improving the yield of liquid-exfoliated nanosheets through repeated separation techniques. *Nanotechnology* **2016**, *27*, 505601.

(3)   Zeng, M.; Shah, S. A.; Huang, D.; Parviz, D.; Yu, Y.-H.; Wang, X.; Green, M. J.; Cheng, Z. Aqueous Exfoliation of Graphite into Graphene Assisted by Sulfonyl Graphene Quantum Dots for Photonic Crystal Applications. *ACS Applied Materials & Interfaces* **2017**, *9*, 30797-30804.

(4)   Shah, S. A.; Habib, T.; Gao, H.; Gao, P.; Sun, W.; Green, M. J.; Radovic, M. Template-free 3D titanium carbide (Ti3C2Tx) MXene particles crumpled by capillary forces. *Chemical Communications* **2017**, *53*, 400-403.

(5)   Parviz, D.; Shah, S. A.; Odom, M. G. B.; Sun, W.; Lutkenhaus, J. L.; Green, M. J. Tailored Network Formation in Graphene Oxide Gels. *Langmuir* **2018**, *34*, 8550-8559.

(6)   Ferrari, A. C.; Meyer, J. C.; Scardaci, V.; Casiraghi, C.; Lazzeri, M.;
Mauri, F.; Piscanec, S.; Jiang, D.; Novoselov, K. S.; Roth, S.; Geim, A. K. Raman
Spectrum of Graphene and Graphene Layers. *Physical Review Letters* **2006**, *97*, 187401.

(7)   Bianco, A.; Cheng, H.-M.; Enoki, T.; Gogotsi, Y.; Hurt, R. H.; Koratkar,
N.; Kyotani, T.; Monthioux, M.; Park, C. R.; Tascon, J. M. D.; Zhang, J. All in the
graphene family – A recommended nomenclature for two-dimensional carbon materials.
Carbon **2013**, *65*, 1-6.

(8)   Park, S.; Ruoff, R. S. Chemical methods for the production of graphenes.
Nature Nanotechnology **2009**, *4*, 217-224.

(9)   Liu, N.; Fu, L.; Dai, B.; Yan, K.; Liu, X.; Zhao, R.; Zhang, Y.; Liu, Z.
Universal Segregation Growth Approach to Wafer-Size Graphene from Non-Noble
Metals. *Nano Letters* **2011**, *11*, 297-303.

(10)   Production of a 100-m-long high-quality graphene transparent conductive
film by roll-to-roll chemical vapor deposition and transfer process. *Appl. Phys. Lett.*
2013, *102*, 023112.

(11)   Sutter, P. How silicon leaves the scene. *Nature Materials* **2009**, *8*, 171.

(12)   Novoselov, K. S.; Geim, A. K.; Morozov, S. V.; Jiang, D.; Zhang, Y.;
Dubonos, S. V.; Grigorieva, I. V.; Firsov, A. A. Electric Field Effect in Atomically Thin
Carbon Films. *Science* **2004**, *306*, 666-669.

(13)   Wei, Y.; Sun, Z. Liquid-phase exfoliation of graphite for mass production of pristine few-layer graphene. *Current Opinion in Colloid & Interface Science* **2015**, *20*, 311-321.

(14)   Fu, W.; Kiggans, J.; Overbury, S. H.; Schwartz, V.; Liang, C. Low-temperature exfoliation of multilayer-graphene material from FeCl3 and CH3NO2 co-intercalated graphite compound. *Chemical Communications* **2011**, *47*, 5265-5267.

(15)   Dresselhaus, M. S.; Dresselhaus, G. Intercalation compounds of graphite. *Advances in Physics* **1981**, *30*, 139-326.

(16)   Hooley, J. G. Physical chemistry and mechanism of intercalation in graphite. *Materials Science and Engineering* **1977**, *31*, 17-24.

(17)   Vogel, F. L.: Intercalation Compounds of Graphite. In *Molecular Metals*; Hatfield, W. E., Ed.; Springer US: Boston, MA, 1979; pp 261-279.

(18)   Asghar, H. M. A.; Hussain, S. N.; Sattar, H.; Brown, N. W.; Roberts, E. P. L. Environmentally friendly preparation of exfoliated graphite. *Journal of Industrial and Engineering Chemistry* **2014**, *20*, 1936-1941.

(19)   Kovtyukhova, N. I.; Wang, Y.; Berkdemir, A.; Cruz-Silva, R.; Terrones, M.; Crespi, V. H.; Mallouk, T. E. Non-oxidative intercalation and exfoliation of graphite by Brønsted acids. *Nature Chemistry* **2014**, *6*, 957.

(20)   Pu, N.-W.; Wang, C.-A.; Sung, Y.; Liu, Y.-M.; Ger, M.-D. Production of few-layer graphene by supercritical CO2 exfoliation of graphite. *Materials Letters* **2009**, *63*, 1987-1989.

(21)   Morales, G. M.; Schifani, P.; Ellis, G.; Ballesteros, C.; Martínez, G.; Barbero, C.; Salavagione, H. J. High-quality few layer graphene produced by electrochemical intercalation and microwave-assisted expansion of graphite. *Carbon* **2011**, *49*, 2809-2816.

(22)   Viculis, L. M.; Mack, J. J.; Mayer, O. M.; Hahn, H. T.; Kaner, R. B. Intercalation and exfoliation routes to graphite nanoplatelets. *Journal of Materials Chemistry* **2005**, *15*, 974-978.

(23)   Yi, M.; Shen, Z. A review on mechanical exfoliation for the scalable production of graphene. *Journal of Materials Chemistry A* **2015**, *3*, 11700-11715.

(24)   Giancarlo, C.; Pedro, C. Sonication-Assisted Fabrication and Post-Synthetic Modifications of Graphene-Like Materials. *Chemistry – A European Journal* **2010**, *16*, 5246-5259.

(25)   Paton, K. R.; Varrla, E.; Backes, C.; Smith, R. J.; Khan, U.; O'Neill, A.; Boland, C.; Lotya, M.; Istrate, O. M.; King, P.; Higgins, T.; Barwich, S.; May, P.; Puczkarski, P.; Ahmed, I.; Moebius, M.; Pettersson, H.; Long, E.; Coelho, J.; O'Brien, S. E.; McGuire, E. K.; Sanchez, B. M.; Duesberg, G. S.; McEvoy, N.; Pennycook, T. J.; Downing, C.; Crossley, A.; Nicolosi, V.; Coleman, J. N. Scalable production of large

quantities of defect-free few-layer graphene by shear exfoliation in liquids. *Nature Materials* **2014**, *13*, 624.

(26)   Nacken, T. J.; Damm, C.; Walter, J.; Rüger, A.; Peukert, W. Delamination of graphite in a high pressure homogenizer. *RSC Advances* **2015**, *5*, 57328-57338.

(27)   Yi, M.; Shen, Z. Kitchen blender for producing high-quality few-layer graphene. *Carbon* **2014**, *78*, 622-626.

(28)   Lotya, M.; Hernandez, Y.; King, P. J.; Smith, R. J.; Nicolosi, V.; Karlsson, L. S.; Blighe, F. M.; De, S.; Wang, Z.; McGovern, I. T.; Duesberg, G. S.; Coleman, J. N. Liquid Phase Production of Graphene by Exfoliation of Graphite in Surfactant/Water Solutions. *Journal of the American Chemical Society* **2009**, *131*, 3611-3620.

(29)   Vadukumpully, S.; Paul, J.; Mahanta, N.; Valiyaveettil, S. Flexible conductive graphene/poly(vinyl chloride) composite thin films with high mechanical strength and thermal stability. *Carbon* **2011**, *49*, 198-205.

(30)   Sukanta, D.; J., K. P.; Mustafa, L.; Arlene, O. N.; M., D. E.; Yenny, H.; S., D. G.; N., C. J. Flexible, Transparent, Conducting Films of Randomly Stacked Graphene from Surfactant-Stabilized, Oxide-Free Graphene Dispersions. *Small* **2010**, *6*, 458-464.

(31)   Lotya, M.; King, P. J.; Khan, U.; De, S.; Coleman, J. N. High-Concentration, Surfactant-Stabilized Graphene Dispersions. *ACS Nano* **2010**, *4*, 3155-3162.

(32)   Wajid, A. S.; Das, S.; Irin, F.; Ahmed, H. S. T.; Shelburne, J. L.; Parviz, D.; Fullerton, R. J.; Jankowski, A. F.; Hedden, R. C.; Green, M. J. Polymer-stabilized graphene dispersions at high concentrations in organic solvents for composite production. *Carbon* **2012**, *50*, 526-534.

(33)   Bourlinos, A. B.; Georgakilas, V.; Zboril, R.; Steriotis, T. A.; Stubos, A. K.; Trapalis, C. Aqueous-phase exfoliation of graphite in the presence of polyvinylpyrrolidone for the production of water-soluble graphenes. *Solid State Communications* **2009**, *149*, 2172-2176.

(34)   Das, S.; Irin, F.; Ma, L.; Bhattacharia, S. K.; Hedden, R. C.; Green, M. J. Rheology and Morphology of Pristine Graphene/Polyacrylamide Gels. *ACS Applied Materials & Interfaces* **2013**, *5*, 8633-8640.

(35)   Parviz, D.; Das, S.; Ahmed, H. S. T.; Irin, F.; Bhattacharia, S.; Green, M. J. Dispersions of Non-Covalently Functionalized Graphene with Minimal Stabilizer. *Acs Nano* **2012**, *6*, 8857-8867.

(36)   Das, S.; Irin, F.; Tanvir Ahmed, H. S.; Cortinas, A. B.; Wajid, A. S.; Parviz, D.; Jankowski, A. F.; Kato, M.; Green, M. J. Non-covalent functionalization of

pristine few-layer graphene using triphenylene derivatives for conductive poly (vinyl alcohol) composites. *Polymer* **2012**, *53*, 2485-2494.

(37)   Su, Q.; Pang, S.; Alijani, V.; Li, C.; Feng, X.; Müllen, K. Composites of Graphene with Large Aromatic Molecules. *Advanced Materials* **2009**, *21*, 3191-3195.

(38)   M., E. J.; Jonas, R.; D., S. C.; Ralf, G.; Martin, H.; Frank, H.; Andreas, H. Soluble Graphene: Generation of Aqueous Graphene Solutions Aided by a Perylenebisimide-Based Bolaamphiphile. *Advanced Materials* **2009**, *21*, 4265-4269.

(39)   V., K. N.; M., E. J.; Guang, Y.; Erdmann, S.; D., S. C.; Frank, H.; Andreas, H. Non-Covalent Chemistry of Graphene: Electronic Communication with Dendronized Perylene Bisimides. *Advanced Materials* **2010**, *22*, 5483-5487.

(40)   Green, A. A.; Hersam, M. C. Solution Phase Production of Graphene with Controlled Thickness via Density Differentiation. *Nano Letters* **2009**, *9*, 4031-4036.

(41)   T., H.; F., T.; Z., S.; D., P.; V., N.; G., P.; F., B.; C., F. A. Solution-phase exfoliation of graphite for ultrafast photonics. *physica status solidi (b)* **2010**, *247*, 2953-2957.

(42)   Guardia, L.; Fernández-Merino, M. J.; Paredes, J. I.; Solís-Fernández, P.; Villar-Rodil, S.; Martínez-Alonso, A.; Tascón, J. M. D. High-throughput production of pristine graphene in an aqueous dispersion assisted by non-ionic surfactants. *Carbon* **2011**, *49*, 1653-1662.

(43)   Ronan, J. S.; Mustafa, L.; Jonathan, N. C. The importance of repulsive potential barriers for the dispersion of graphene using surfactants. *New Journal of Physics* **2010**, *12*, 125008.

(44)   Bari, R.; Parviz, D.; Khabaz, F.; Klaassen, C. D.; Metzler, S. D.; Hansen, M. J.; Khare, R.; Green, M. J. Liquid phase exfoliation and crumpling of inorganic nanosheets. *Physical Chemistry Chemical Physics* **2015**, *17*, 9383-9393.

(45)   Konkena, B.; Vasudevan, S. Understanding Aqueous Dispersibility of Graphene Oxide and Reduced Graphene Oxide through pKa Measurements. *The Journal of Physical Chemistry Letters* **2012**, *3*, 867-872.

(46)   Irin, F.; Hansen, M. J.; Bari, R.; Parviz, D.; Metzler, S. D.; Bhattacharia, S. K.; Green, M. J. Adsorption and removal of graphene dispersants. *Journal of Colloid and Interface Science* **2015**, *446*, 282-289.

(47)   Hansen, M. J.; Rountree, K. S.; Irin, F.; Sweeney, C. B.; Klaassen, C. D.; Green, M. J. Photodegradation of dispersants in colloidal suspensions of pristine graphene. *Journal of Colloid and Interface Science* **2016**, *466*, 425-431.

(48)   An, X.; Simmons, T.; Shah, R.; Wolfe, C.; Lewis, K. M.; Washington, M.; Nayak, S. K.; Talapatra, S.; Kar, S. Stable Aqueous Dispersions of Noncovalently Functionalized Graphene from Graphite and their Multifunctional High-Performance Applications. *Nano Letters* **2010**, *10*, 4295-4301.

(49)   Xu, Y.; Bai, H.; Lu, G.; Li, C.; Shi, G. Flexible Graphene Films via the Filtration of Water-Soluble Noncovalent Functionalized Graphene Sheets. *Journal of the American Chemical Society* **2008**, *130*, 5856-5857.

(50)   Ming, Z.; R., P. R.; Daniel, M.; Boya, D.; Phil, L.; William, C.; Roman, B.; Lam, C. P.; Tao, Z.; Zhongfan, L.; Eric, G.; Huixin, H. Production of Graphene Sheets by Direct Dispersion with Aromatic Healing Agents. *Small* **2010**, *6*, 1100-1107.

(51)   Schlierf, A.; Yang, H.; Gebremedhn, E.; Treossi, E.; Ortolani, L.; Chen, L.; Minoia, A.; Morandi, V.; Samorì, P.; Casiraghi, C.; Beljonne, D.; Palermo, V. Nanoscale insight into the exfoliation mechanism of graphene with organic dyes: effect of charge, dipole and molecular structure. *Nanoscale* **2013**, *5*, 4205-4216.

(52)   Paton, K. R.; Varrla, E.; Backes, C.; Smith, R. J.; Khan, U.; O'Neill, A.; Boland, C.; Lotya, M.; Istrate, O. M.; King, P.; Higgins, T.; Barwich, S.; May, P.; Puczkarski, P.; Ahmed, I.; Moebius, M.; Pettersson, H.; Long, E.; Coelho, J.; O'Brien, S. E.; McGuire, E. K.; Sanchez, B. M.; Duesberg, G. S.; McEvoy, N.; Pennycook, T. J.; Downing, C.; Crossley, A.; Nicolosi, V.; Coleman, J. N. Scalable production of large quantities of defect-free few-layer graphene by shear exfoliation in liquids. *Nat Mater* **2014**, *13*, 624-630.

(53)   Halbig, C. E.; Nacken, T. J.; Walter, J.; Damm, C.; Eigler, S.; Peukert, W. Quantitative investigation of the fragmentation process and defect density evolution of

oxo-functionalized graphene due to ultrasonication and milling. *Carbon* **2016**, *96*, 897-903.

(54)   Kokai, F.; Sorin, R.; Chigusa, H.; Hanai, K.; Koshio, A.; Ishihara, M.; Koga, Y.; Hasegawa, M.; Imanishi, N.; Takeda, Y. Ultrasonication fabrication of high quality multilayer graphene flakes and their characterization as anodes for lithium ion batteries. *Diamond and Related Materials* **2012**, *29*, 63-68.

(55)   Umar, K.; Arlene, O. N.; Mustafa, L.; Sukanta, D.; N., C. J. High-Concentration Solvent Exfoliation of Graphene. *Small* **2010**, *6*, 864-871.

(56)   Coleman, J. N.; Lotya, M.; O'Neill, A.; Bergin, S. D.; King, P. J.; Khan, U.; Young, K.; Gaucher, A.; De, S.; Smith, R. J.; Shvets, I. V.; Arora, S. K.; Stanton, G.; Kim, H.-Y.; Lee, K.; Kim, G. T.; Duesberg, G. S.; Hallam, T.; Boland, J. J.; Wang, J. J.; Donegan, J. F.; Grunlan, J. C.; Moriarty, G.; Shmeliov, A.; Nicholls, R. J.; Perkins, J. M.; Grieveson, E. M.; Theuwissen, K.; McComb, D. W.; Nellist, P. D.; Nicolosi, V. Two-Dimensional Nanosheets Produced by Liquid Exfoliation of Layered Materials. *Science* **2011**, *331*, 568-571.

(57)   Huang, X.; Zeng, Z.; Zhang, H. Metal dichalcogenide nanosheets: preparation, properties and applications. *Chemical Society Reviews* **2013**, *42*, 1934-1946.

(58)   Zhu, Y.; Murali, S.; Cai, W.; Li, X.; Suk, J. W.; Potts, J. R.; Ruoff, R. S. Graphene and Graphene Oxide: Synthesis, Properties, and Applications. *Advanced Materials* **2010**, *22*, 3906-3924.

(59)   Wang, Q. H.; Kalantar-Zadeh, K.; Kis, A.; Coleman, J. N.; Strano, M. S. Electronics and optoelectronics of two-dimensional transition metal dichalcogenides. *Nature Nanotechnology* **2012**, *7*, 699-712.

(60)   Kim, H.; Abdala, A. A.; Macosko, C. W. Graphene/Polymer Nanocomposites. *Macromolecules* **2010**, *43*, 6515-6530.

(61)   Lin, Y.; Connell, J. W. Advances in 2D boron nitride nanostructures: nanosheets, nanoribbons, nanomeshes, and hybrids with graphene. *Nanoscale* **2012**, *4*, 6908-6939.

(62)   Huafeng, Y.; Freddie, W.; Elias, G.; Edward, L.; Liam, B.; Alexandre, F.; Vincenzo, P.; Sarah, H.; David, B.; Casiraghi, C. Dielectric nanosheets made by liquid-phase exfoliation in water and their use in graphene-based electronics. *2D Materials* **2014**, *1*, 011012.

(63)   Guardia, L.; Paredes, J. I.; Rozada, R.; Villar-Rodil, S.; Martinez-Alonso, A.; Tascon, J. M. D. Production of aqueous dispersions of inorganic graphene analogues by exfoliation and stabilization with non-ionic surfactants. *Rsc Advances* **2014**, *4*, 14115-14127.

(64)   Nicolosi, V.; Chhowalla, M.; Kanatzidis, M. G.; Strano, M. S.; Coleman, J. N. Liquid Exfoliation of Layered Materials. *Science* **2013**, *340*.

(65)   Park, S.; Ruoff, R. S. Chemical methods for the production of graphenes. *Nat Nano* **2009**, *4*, 217-224.

(66)   Du, W.; Jiang, X.; Zhu, L. From graphite to graphene: direct liquid-phase exfoliation of graphite to produce single- and few-layered pristine graphene. *Journal of Materials Chemistry A* **2013**, *1*, 10592-10606.

(67)   Du, W.; Lu, J.; Sun, P.; Zhu, Y.; Jiang, X. Organic salt-assisted liquid-phase exfoliation of graphite to produce high-quality graphene. *Chemical Physics Letters* **2013**, *568–569*, 198-201.

(68)   Hernandez, Y.; Nicolosi, V.; Lotya, M.; Blighe, F. M.; Sun, Z.; De, S.; McGovern, I. T.; Holland, B.; Byrne, M.; Gun'Ko, Y. K.; Boland, J. J.; Niraj, P.; Duesberg, G.; Krishnamurthy, S.; Goodhue, R.; Hutchison, J.; Scardaci, V.; Ferrari, A. C.; Coleman, J. N. High-yield production of graphene by liquid-phase exfoliation of graphite. *Nat Nano* **2008**, *3*, 563-568.

(69)   Varrla, E.; Backes, C.; Paton, K. R.; Harvey, A.; Gholamvand, Z.; McCauley, J.; Coleman, J. N. Large-Scale Production of Size-Controlled MoS2 Nanosheets by Shear Exfoliation. *Chemistry of Materials* **2015**, *27*, 1129-1139.

(70)   Puangbuppha, B.; Limsuwan, P.; Asanithi, P. Non-Chemically Functionalized Graphene Exfoliated from Graphite in Water using Ultrasonic Treatment. *Procedia Engineering* **2012**, *32*, 1094-1099.

(71)   Nacken, T. J.; Damm, C.; Walter, J.; Ruger, A.; Peukert, W. Delamination of graphite in a high pressure homogenizer. *RSC Advances* **2015**, *5*, 57328-57338.

(72)   Texter, J. Colloidal graphene—Scalable processing for advanced materials. *Current Opinion in Colloid & Interface Science* **2015**, *20*, 305-310.

(73)   Paton, K. R.; Varrla, E.; Backes, C.; Smith, R. J.; Khan, U.; O'Neill, A.; Boland, C.; Lotya, M.; Istrate, O. M.; King, P.; Higgins, T.; Barwich, S.; May, P.; Puczkarski, P.; Ahmed, I.; Moebius, M.; Pettersson, H.; Long, E.; Coelho, J.; O'Brien, S. E.; McGuire, E. K.; Sanchez, B. M.; Duesberg, G. S.; McEvoy, N.; Pennycook, T. J.; Downing, C.; Crossley, A.; Nicolosi, V.; Coleman, J. N. Scalable production of large quantities of defect-free few-layer graphene by shear exfoliation in liquids. *Nature Materials* **2014**, *13*, 624-630.

(74)   Bari, R.; Parviz, D.; Khabaz, F.; Klaassen, C. D.; Metzler, S. D.; Hansen, M. J.; Khare, R.; Green, M. J. Liquid phase exfoliation and crumpling of inorganic nanosheets. *Physical Chemistry Chemical Physics* **2015**.

(75)   Lotya, M.; Rakovich, A.; Donegan, J. F.; Coleman, J. N. Measuring the lateral size of liquid-exfoliated nanosheets with dynamic light scattering. *Nanotechnology* **2013**, *24*, 265703.

(76)   Parviz, D.; Irin, F.; Shah, S. A.; Das, S.; Sweeney, C. B.; Green, M. J. Challenges in liquid phase exfoliation, processing and assembly of pristine graphene. *Advanced Materials* **2016**, *in press*.

(77)   Dong, X.; Shi, Y.; Zhao, Y.; Chen, D.; Ye, J.; Yao, Y.; Gao, F.; Ni, Z.; Yu, T.; Shen, Z.; Huang, Y.; Chen, P.; Li, L.-J. Symmetry Breaking of Graphene Monolayers by Molecular Decoration. *Phys Rev Lett* **2009**, *102*, 135501.

(78)   Zhang, M.; Parajuli, R. R.; Mastrogiovanni, D.; Dai, B.; Lo, P.; Cheung, W.; Brukh, R.; Chiu, P. L.; Zhou, T.; Liu, Z. Production of graphene sheets by direct dispersion with aromatic healing agents. *Small* **2010**, *6*, 1100-1107.

(79)   Ciesielski, A.; Samorì, P. Graphene via sonication assisted liquid-phase exfoliation. *Chem Soc Rev* **2014**, *43*, 381-398.

(80)   Eigler, S.; Hirsch, A. Chemistry with graphene and graphene oxide—challenges for synthetic chemists. *Angewandte Chemie International Edition* **2014**, *53*, 7720-7738.

(81)   Zheng, X. T.; Ananthanarayanan, A.; Luo, K. Q.; Chen, P. Glowing graphene quantum dots and carbon dots: properties, syntheses, and biological applications. *Small* **2014**.

(82)   Kantheti, S.; Gaddam, R. R.; Narayan, R.; Raju, K. V. S. N. Hyperbranched polyol decorated carbon nanotube by click chemistry for functional polyurethane urea hybrid composites. *RSC Advances* **2014**, *4*, 24420-24427.

(83)   Xu, M.; Zhang, W.; Yang, Z.; Yu, F.; Ma, Y.; Hu, N.; He, D.; Liang, Q.; Su, Y.; Zhang, Y. One-pot liquid-phase exfoliation from graphite to graphene with carbon quantum dots. *Nanoscale* **2015**.

(84)   Dong, Y. Q.; Pang, H. C.; Yang, H. B.; Guo, C. X.; Shao, J. W.; Chi, Y. W.; Li, C. M.; Yu, T. Carbon-Based Dots Co-doped with Nitrogen and Sulfur for High Quantum Yield and Excitation-Independent Emission. *Angew Chem Int Edit* **2013**, *52*, 7800-7804.

(85)   Dong, Y. Q.; Shao, J. W.; Chen, C. Q.; Li, H.; Wang, R. X.; Chi, Y. W.; Lin, X. M.; Chen, G. N. Blue luminescent graphene quantum dots and graphene oxide prepared by tuning the carbonization degree of citric acid. *Carbon* **2012**, *50*, 4738-4743.

(86)   Gokhale, R.; Singh, P. Blue Luminescent Graphene Quantum Dots by Photochemical Stitching of Small Aromatic Molecules: Fluorescent Nanoprobes in Cellular Imaging. *Part Part Syst Char* **2014**, *31*, 433-438.

(87)   Yang, H.; Kang, D. J.; Ku, K. H.; Cho, H. H.; Park, C. H.; Lee, J.; Lee, D. C.; Ajayan, P. M.; Kim, B. J. Highly Luminescent Polymer Particles Driven by Thermally Reduced Graphene Quantum Dot Surfactants. *Acs Macro Lett* **2014**, *3*, 985-990.

(88)   Parviz, D.; Irin, F.; Shah, S. A.; Das, S.; Sweeney, C. B.; Green, M. J. Challenges in Liquid-Phase Exfoliation, Processing, and Assembly of Pristine Graphene. *Adv Mater* **2016**, *28*, 8796-8818.

(89)   Wang, H.; Chen, Z.; Xin, L.; Cui, J.; Zhao, S.; Yan, Y. Synthesis of pyrene-capped polystyrene by free radical polymerization and its application in direct

exfoliation of graphite into graphene nanosheets. *Journal of Polymer Science Part A: Polymer Chemistry* **2015**.

(90)   Vallés, C.; Drummond, C.; Saadaoui, H.; Furtado, C. A.; He, M.; Roubeau, O.; Ortolani, L.; Monthioux, M.; Pénicaud, A. Solutions of Negatively Charged Graphene Sheets and Ribbons. *Journal of the American Chemical Society* **2008**, *130*, 15802-15804.

(91)   Zhang, F.; Liu, F.; Wang, C.; Xin, X.; Liu, J.; Guo, S.; Zhang, J. Effect of Lateral Size of Graphene Quantum Dots on Their Properties and Application. *ACS Applied Materials & Interfaces* **2016**, *8*, 2104-2110.

(92)   Hanaor, D.; Michelazzi, M.; Leonelli, C.; Sorrell, C. C. The effects of carboxylic acids on the aqueous dispersion and electrophoretic deposition of ZrO 2. *Journal of the European Ceramic Society* **2012**, *32*, 235-244.

(93)   Naguib, M.; Mochalin, V. N.; Barsoum, M. W.; Gogotsi, Y. 25th Anniversary Article: MXenes: A New Family of Two-Dimensional Materials. *Advanced Materials* **2014**, *26*, 992-1005.

(94)   Hantanasirisakul, K.; Zhao, M.-Q.; Urbankowski, P.; Halim, J.; Anasori, B.; Kota, S.; Ren, C. E.; Barsoum, M. W.; Gogotsi, Y. Fabrication of Ti3C2Tx MXene Transparent Thin Films with Tunable Optoelectronic Properties. *Advanced Electronic Materials* **2016**, *2*, n/a-n/a.

(95)   Dillon, A. D.; Ghidiu, M. J.; Krick, A. L.; Griggs, J.; May, S. J.; Gogotsi, Y.; Barsoum, M. W.; Fafarman, A. T. Highly Conductive Optical Quality Solution-Processed Films of 2D Titanium Carbide. *Advanced Functional Materials* **2016**, *26*, 4162-4168.

(96)   Peng, X.; Peng, L.; Wu, C.; Xie, Y. Two dimensional nanomaterials for flexible supercapacitors. *Chemical Society Reviews* **2014**, *43*, 3303-3323.

(97)   Ling, Z.; Ren, C. E.; Zhao, M.-Q.; Yang, J.; Giammarco, J. M.; Qiu, J.; Barsoum, M. W.; Gogotsi, Y. Flexible and conductive MXene films and nanocomposites with high capacitance. *Proceedings of the National Academy of Sciences* **2014**, *111*, 16676-16681.

(98)   Halim, J.; Lukatskaya, M. R.; Cook, K. M.; Lu, J.; Smith, C. R.; Näslund, L.-Å.; May, S. J.; Hultman, L.; Gogotsi, Y.; Eklund, P. Transparent conductive two-dimensional titanium carbide epitaxial thin films. *Chemistry of Materials* **2014**, *26*, 2374-2381.

(99)   Lukatskaya, M. R.; Mashtalir, O.; Ren, C. E.; Dall'Agnese, Y.; Rozier, P.; Taberna, P. L.; Naguib, M.; Simon, P.; Barsoum, M. W.; Gogotsi, Y. Cation Intercalation and High Volumetric Capacitance of Two-Dimensional Titanium Carbide. *Science* **2013**, *341*, 1502-1505.

112

(100)   Dall'Agnese, Y.; Lukatskaya, M. R.; Cook, K. M.; Taberna, P.-L.; Gogotsi, Y.; Simon, P. High capacitance of surface-modified 2D titanium carbide in acidic electrolyte. *Electrochemistry Communications* **2014**, *48*, 118-122.

(101)   Xie, X.; Chen, S.; Ding, W.; Nie, Y.; Wei, Z. An extraordinarily stable catalyst: Pt NPs supported on two-dimensional Ti3C2X2 (X = OH, F) nanosheets for oxygen reduction reaction. *Chemical Communications* **2013**, *49*, 10112-10114.

(102)   Xie, X.; Xue, Y.; Li, L.; Chen, S.; Nie, Y.; Ding, W.; Wei, Z. Surface Al leached Ti3AlC2 as a substitute for carbon for use as a catalyst support in a harsh corrosive electrochemical system. *Nanoscale* **2014**, *6*, 11035-11040.

(103)   Peng, Q.; Guo, J.; Zhang, Q.; Xiang, J.; Liu, B.; Zhou, A.; Liu, R.; Tian, Y. Unique Lead Adsorption Behavior of Activated Hydroxyl Group in Two-Dimensional Titanium Carbide. *Journal of the American Chemical Society* **2014**, *136*, 4113-4116.

(104)   Shahzad, F.; Alhabeb, M.; Hatter, C. B.; Anasori, B.; Hong, S. M.; Koo, C. M.; Gogotsi, Y. Electromagnetic interference shielding with 2D transition metal carbides (MXenes). *Science* **2016**, *353*, 1137-1140.

(105)   Han, M.; Yin, X.; Wu, H.; Hou, Z.; Song, C.; Li, X.; Zhang, L.; Cheng, L. Ti3C2 MXenes with Modified Surface for High-Performance Electromagnetic Absorption and Shielding in the X-Band. *ACS Applied Materials & Interfaces* **2016**, *8*, 21011-21019.

(106)   Ren, C. E.; Hatzell, K. B.; Alhabeb, M.; Ling, Z.; Mahmoud, K. A.; Gogotsi, Y. Charge- and Size-Selective Ion Sieving Through Ti3C2Tx MXene Membranes. *The Journal of Physical Chemistry Letters* **2015**, *6*, 4026-4031.

(107)   Lei, J.-C.; Zhang, X.; Zhou, Z. Recent advances in MXene: Preparation, properties, and applications. *Frontiers of Physics* **2015**, *10*, 276-286.

(108)   Naguib, M.; Kurtoglu, M.; Presser, V.; Lu, J.; Niu, J.; Heon, M.; Hultman, L.; Gogotsi, Y.; Barsoum, M. W. Two-Dimensional Nanocrystals Produced by Exfoliation of Ti3AlC2. *Advanced Materials* **2011**, *23*, 4248-4253.

(109)   Hu, M.; Li, Z.; Zhang, H.; Hu, T.; Zhang, C.; Wu, Z.; Wang, X. Self-assembled Ti3C2Tx MXene film with high gravimetric capacitance. *Chemical Communications* **2015**, *51*, 13531-13533.

(110)   Enyashin, A. N.; Ivanovskii, A. L. Atomic structure, comparative stability and electronic properties of hydroxylated Ti2C and Ti3C2 nanotubes. *Computational and Theoretical Chemistry* **2012**, *989*, 27-32.

(111)   Parviz, D.; Metzler, S. D.; Das, S.; Irin, F.; Green, M. J. Tailored Crumpling and Unfolding of Spray-Dried Pristine Graphene and Graphene Oxide Sheets. *Small* **2015**, *11*, 2661-2668.

(112)   Luo, J.; Jang, H. D.; Huang, J. Effect of Sheet Morphology on the Scalability of Graphene-Based Ultracapacitors. *ACS Nano* **2013**, *7*, 1464-1471.

(113)   Zou, Y.; Kinloch, I. A.; Dryfe, R. A. W. Nitrogen-doped and crumpled graphene sheets with improved supercapacitance. *Journal of Materials Chemistry A* **2014**, *2*, 19495-19499.

(114)   Li, Y.; Lv, X.; Lu, J.; Li, J. Preparation of SnO2-Nanocrystal/Graphene-Nanosheets Composites and Their Lithium Storage Ability. *The Journal of Physical Chemistry C* **2010**, *114*, 21770-21774.

(115)   Zhou, G.; Wang, D.-W.; Li, F.; Zhang, L.; Li, N.; Wu, Z.-S.; Wen, L.; Lu, G. Q.; Cheng, H.-M. Graphene-Wrapped Fe3O4 Anode Material with Improved Reversible Capacity and Cyclic Stability for Lithium Ion Batteries. *Chemistry of Materials* **2010**, *22*, 5306-5313.

(116)   Ghidiu, M.; Lukatskaya, M. R.; Zhao, M.-Q.; Gogotsi, Y.; Barsoum, M. W. Conductive two-dimensional titanium carbide /ˆclay/' with high volumetric capacitance. *Nature* **2014**, *516*, 78-81.

(117)   Mashtalir, O.; Naguib, M.; Mochalin, V. N.; Dall'Agnese, Y.; Heon, M.; Barsoum, M. W.; Gogotsi, Y. Intercalation and delamination of layered carbides and carbonitrides. *Nat Commun* **2013**, *4*, 1716.

(118)   Naguib, M.; Gogotsi, Y. Synthesis of Two-Dimensional Materials by Selective Extraction. *Accounts of Chemical Research* **2015**, *48*, 128-135.

(119)   Gao, H.; Benitez, R.; Son, W.; Arroyave, R.; Radovic, M. Structural, physical and mechanical properties of Ti3(Al1−xSix)C2 solid solution with x=0–1. *Materials Science and Engineering: A* **2016**, *676*, 197-208.

(120)   Li, Z.; Wang, L.; Sun, D.; Zhang, Y.; Liu, B.; Hu, Q.; Zhou, A. Synthesis and thermal stability of two-dimensional carbide MXene Ti3C2. *Materials Science and Engineering: B* **2015**, *191*, 33-40.

(121)   Halim, J.; Lukatskaya, M. R.; Cook, K. M.; Lu, J.; Smith, C. R.; Näslund, L.-Å.; May, S. J.; Hultman, L.; Gogotsi, Y.; Eklund, P.; Barsoum, M. W. Transparent Conductive Two-Dimensional Titanium Carbide Epitaxial Thin Films. *Chemistry of Materials* **2014**, *26*, 2374-2381.

(122)   Wang, X.; Shen, X.; Gao, Y.; Wang, Z.; Yu, R.; Chen, L. Atomic-Scale Recognition of Surface Structure and Intercalation Mechanism of Ti3C2X. *Journal of the American Chemical Society* **2015**, *137*, 2715-2721.

(123)   Halim, J.; Cook, K. M.; Naguib, M.; Eklund, P.; Gogotsi, Y.; Rosen, J.; Barsoum, M. W. X-ray photoelectron spectroscopy of select multi-layered transition metal carbides (MXenes). *Applied Surface Science* **2016**, *362*, 406-417.

(124)   Lukatskaya, M. R.; Halim, J.; Dyatkin, B.; Naguib, M.; Buranova, Y. S.; Barsoum, M. W.; Gogotsi, Y. Room-Temperature Carbide-Derived Carbon Synthesis by Electrochemical Etching of MAX Phases. *Angewandte Chemie International Edition* **2014**, *53*, 4877-4880.

116

(125)   El-Kady, M. F.; Shao, Y.; Kaner, R. B. Graphene for batteries, supercapacitors and beyond. *Nature Reviews Materials* **2016**, *1*, 16033.

(126)   Huang, L.; Santiago, D.; Loyselle, P.; Dai, L. Graphene-Based Nanomaterials for Flexible and Wearable Supercapacitors. *Small* **2018**, *14*, 1800879.

(127)   Yan, J.; Wei, T.; Shao, B.; Ma, F.; Fan, Z.; Zhang, M.; Zheng, C.; Shang, Y.; Qian, W.; Wei, F. Electrochemical properties of graphene nanosheet/carbon black composites as electrodes for supercapacitors. *Carbon* **2010**, *48*, 1731-1737.

(128)   Lv, W.; Zhang, C.; Li, Z.; Yang, Q.-H. Self-Assembled 3D Graphene Monolith from Solution. *The Journal of Physical Chemistry Letters* **2015**, *6*, 658-668.

(129)   García-Bordejé, E.; Víctor-Román, S.; Sanahuja-Parejo, O.; Benito, A. M.; Maser, W. K. Control of the microstructure and surface chemistry of graphene aerogels via pH and time manipulation by a hydrothermal method. *Nanoscale* **2018**, *10*, 3526-3539.

(130)   Hu, K.; Xie, X.; Szkopek, T.; Cerruti, M. Understanding Hydrothermally Reduced Graphene Oxide Hydrogels: From Reaction Products to Hydrogel Properties. *Chemistry of Materials* **2016**, *28*, 1756-1768.

(131)   Wang, Z.; Gao, H.; Zhang, Q.; Liu, Y.; Chen, J.; Guo, Z. Recent Advances in 3D Graphene Architectures and Their Composites for Energy Storage Applications. *Small* **2019**, *15*, 1803858.

(132)   Shi, Q.; Cha, Y.; Song, Y.; Lee, J.-I.; Zhu, C.; Li, X.; Song, M.-K.; Du, D.; Lin, Y. 3D graphene-based hybrid materials: synthesis and applications in energy storage and conversion. *Nanoscale* **2016**, *8*, 15414-15447.

(133)   Kim, B. C.; Hong, J.-Y.; Wallace, G. G.; Park, H. S. Recent Progress in Flexible Electrochemical Capacitors: Electrode Materials, Device Configuration, and Functions. *Advanced Energy Materials* **2015**, *5*, 1500959.

(134)   Xu, Y.; Lin, Z.; Huang, X.; Liu, Y.; Huang, Y.; Duan, X. Flexible Solid-State Supercapacitors Based on Three-Dimensional Graphene Hydrogel Films. *ACS Nano* **2013**, *7*, 4042-4049.

(135)   Flouda, P.; Feng, X.; Boyd, J. G.; Thomas, E. L.; Lagoudas, D. C.; Lutkenhaus, J. L. Interfacial Engineering of Reduced Graphene Oxide for Aramid Nanofiber-Enabled Structural Supercapacitors. *Batteries & Supercaps*, *0*.

(136)   Hu, H.; Zhao, Z.; Wan, W.; Gogotsi, Y.; Qiu, J. Ultralight and Highly Compressible Graphene Aerogels. *Advanced Materials* **2013**, *25*, 2219-2223.

(137)   Hong, J.-Y.; Bak, B. M.; Wie, J. J.; Kong, J.; Park, H. S. Reversibly Compressible, Highly Elastic, and Durable Graphene Aerogels for Energy Storage Devices under Limiting Conditions. *Advanced Functional Materials* **2015**, *25*, 1053-1062.

(138)   Huang, P.; Chen, W.; Yan, L. An inorganic–organic double network hydrogel of graphene and polymer. *Nanoscale* **2013**, *5*, 6034-6039.

(139)   Sun, R.; Chen, H.; Li, Q.; Song, Q.; Zhang, X. Spontaneous assembly of strong and conductive graphene/polypyrrole hybrid aerogels for energy storage. *Nanoscale* **2014**, *6*, 12912-12920.

(140)   Zhao, Y.; Liu, J.; Hu, Y.; Cheng, H.; Hu, C.; Jiang, C.; Jiang, L.; Cao, A.; Qu, L. Highly Compression-Tolerant Supercapacitor Based on Polypyrrole-mediated Graphene Foam Electrodes. *Advanced Materials* **2013**, *25*, 591-595.

(141)   Wang, M.; Duan, X.; Xu, Y.; Duan, X. Functional Three-Dimensional Graphene/Polymer Composites. *ACS Nano* **2016**, *10*, 7231-7247.

(142)   Yang, M.; Cao, K.; Sui, L.; Qi, Y.; Zhu, J.; Waas, A.; Arruda, E. M.; Kieffer, J.; Thouless, M. D.; Kotov, N. A. Dispersions of Aramid Nanofibers: A New Nanoscale Building Block. *ACS nano* **2011**, *5*, 6945-6954.

(143)   Lin, J.; Bang, S. H.; Malakooti, M. H.; Sodano, H. A. Isolation of Aramid Nanofibers for High Strength and Toughness Polymer Nanocomposites. *ACS Applied Materials & Interfaces* **2017**, *9*, 11167-11175.

(144)   Zhou, G.; Wang, W.; Peng, M. Functionalized aramid nanofibers prepared by polymerization induced self-assembly for simultaneously reinforcing and toughening of epoxy and carbon fiber/epoxy multiscale composite. *Composites Science and Technology* **2018**, *168*, 312-319.

(145)   Fan, J.; Shi, Z.; Tian, M.; Yin, J. Graphene–aramid nanofiber nanocomposite paper with high mechanical and electrical performance. *RSC Advances* **2013**, *3*, 17664-17667.

(146)   Zhu, J.; Cao, W.; Yue, M.; Hou, Y.; Han, J.; Yang, M. Strong and Stiff Aramid Nanofiber/Carbon Nanotube Nanocomposites. *ACS Nano* **2015**, *9*, 2489-2501.

(147)   Zhu, J.; Yang, M.; Emre, A.; Bahng, J. H.; Xu, L.; Yeom, J.; Yeom, B.; Kim, Y.; Johnson, K.; Green, P.; Kotov, N. A. Branched Aramid Nanofibers. *Angewandte Chemie International Edition* **2017**, *56*, 11744-11748.

(148)   Kwon, S. R.; Harris, J.; Zhou, T.; Loufakis, D.; Boyd, J. G.; Lutkenhaus, J. L. Mechanically Strong Graphene/Aramid Nanofiber Composite Electrodes for Structural Energy and Power. *ACS Nano* **2017**, *11*, 6682-6690.

(149)   Xu, Y.; Chen, C.-Y.; Zhao, Z.; Lin, Z.; Lee, C.; Xu, X.; Wang, C.; Huang, Y.; Shakir, M. I.; Duan, X. Solution Processable Holey Graphene Oxide and Its Derived Macrostructures for High-Performance Supercapacitors. *Nano Letters* **2015**, *15*, 4605-4610.

(150)   Xu, Y.; Lin, Z.; Zhong, X.; Huang, X.; Weiss, N. O.; Huang, Y.; Duan, X. Holey graphene frameworks for highly efficient capacitive energy storage. *Nature Communications* **2014**, *5*, 4554.

(151)   McAllister, M. J.; Li, J.-L.; Adamson, D. H.; Schniepp, H. C.; Abdala, A. A.; Liu, J.; Herrera-Alonso, M.; Milius, D. L.; Car, R.; Prud'homme, R. K.; Aksay, I. A.

Single Sheet Functionalized Graphene by Oxidation and Thermal Expansion of Graphite. *Chemistry of Materials* **2007**, *19*, 4396-4404.

(152)   Xu, Y.; Sheng, K.; Li, C.; Shi, G. Self-Assembled Graphene Hydrogel via a One-Step Hydrothermal Process. *ACS Nano* **2010**, *4*, 4324-4330.

(153)   Wasalathilake, K. C.; Galpaya, D. G. D.; Ayoko, G. A.; Yan, C. Understanding the structure-property relationships in hydrothermally reduced graphene oxide hydrogels. *Carbon* **2018**, *137*, 282-290.

(154)   Xie, Y.; Sheng, X.; Xie, D.; Liu, Z.; Zhang, X.; Zhong, L. Fabricating graphene hydrogels with controllable pore structure via one-step chemical reduction process. *Carbon* **2016**, *109*, 673-680.

(155)   Fernández-Merino, M. J.; Guardia, L.; Paredes, J. I.; Villar-Rodil, S.; Solís-Fernández, P.; Martínez-Alonso, A.; Tascón, J. M. D. Vitamin C Is an Ideal Substitute for Hydrazine in the Reduction of Graphene Oxide Suspensions. *The Journal of Physical Chemistry C* **2010**, *114*, 6426-6432.

(156)   Sheng, K.-x.; Xu, Y.-x.; Li, C.; Shi, G.-q. High-performance self-assembled graphene hydrogels prepared by chemical reduction of graphene oxide. *New Carbon Materials* **2011**, *26*, 9-15.

(157)   Kyler, S. R.; Smit, A. S.; Charles, B. S.; Fahmida, I.; Micah, J. G. Graphene reflux: improving the yield of liquid-exfoliated nanosheets through repeated separation techniques. *Nanotechnology* **2016**, *27*, 505601.